Mathew Graham

62 Words

The Two Photon Decay of the χ_0 State of Charmonium

Fermilab experiment E835 is dedicated to the study of the charm-anticharm bound states, charmonium, produced in proton-antiproton annihilations. In this dissertation, the two-photon decay rate of the $\chi_{c,0}(^3P_0)$ state is investaged. The result of the analysis gives a product of branching ratios $BR(\chi_0 \to \overline{p}p) \times BR(\chi_0 \to \gamma\gamma) = (6.52 \pm 1.18(sta) \pm 0.55(sys)) \times 10^{-8}$. Inserting this result into a fit with other measurements at the χ_0 gives a two-photon partial width of $\Gamma_{\gamma\gamma} = 2.81 \pm 0.51$ keV.

UNIVERSITY OF MINNESOTA

This is to certify that I have examined this bound copy of a doctoral thesis by

Mathew Graham

and have found that it is complete and satisfactory in all respects and that any and all revisions required by the final examining committee have been made.

Professor Roger W. Rusack

(Faculty Adviser)

GRADUATE SCHOOL

The Two Photon Decay of the χ_0 State of Charmonium

A THESIS

SUBMITTED TO THE FACULTY OF THE GRADUATE SCHOOL

OF THE UNIVERSITY OF MINNESOTA

BY

Mathew Graham

IN PARTIAL FULFILLMENT OF THE REQUIREMENTS

FOR THE DEGREE OF

DOCTOR OF PHILOSOPHY

December, 2002

© Mathew Graham 2002

ALL RIGHTS RESERVED

The Two Photon Decay of the χ_0 State of Charmonium

by Mathew Graham

Under the supervision of Professor Roger W. Rusack

ABSTRACT

Fermilab experiment E835 is dedicated to the study of the charm-anticharm bound states, charmonium, produced in proton-antiproton annihilations. In this dissertation, the two-photon decay rate of the $\chi_{c,0}(^3P_0)$ state is investaged. The result of the analysis gives a product of branching ratios $BR(\chi_0 \to \overline{p}p) \times BR(\chi_0 \to \gamma\gamma) = (6.52 \pm 1.18(sta) \pm 0.55(sys)) \times 10^{-8}$. Inserting this result into a fit with other measurements at the χ_0 gives a two-photon partial width of $\Gamma_{\gamma\gamma} = 2.81 \pm 0.51$ keV.

Acknowledgements

First of all, I would like to give my heartfelt thanks to my advisor, Roger Rusack, for the giving so many different opportunities to help me develop as a scientist. I've feel very fortunate to have had you as my advisor.

I would would also like to thank the entire the E835 collaborators and in particular Stephen Pordes and Keith Gollwitzer. Your patience, dedication, and sacrifice made the experiment happen.

To Michelle Stancari and Ted Vidnovic, I'd like to thank you for always being there to bounce ideas off (even across the Atlantic) and for all the support you've given me through the past few years.

To my good friends Travis Novak, Andy Cady, and Mindy Simons: thanks for being patient and sticking with me even when I haven't been a such a great friend.

And finally, to Kelly...we've have been through a lot together. Without you I doubt that this thesis would have ever been completed. You make me a better person and whatever happens down the road I know that we will always be the best of friends.

Table of Contents

Abstract **i**

Acknowledgements **ii**

List of Tables **vi**

List of Figures **vii**

1 Introduction **1**

1.1 The Discovery of Charm 2

1.2 The $\overline{c}c$ System 7

1.3 Charmonium Formation 10

1.4 Theoretical Predictions 11

1.5 Theoretical Predictions for $\Gamma_{\gamma\gamma}$ 13

2 Experiment E835 **16**

2.1 The Antiproton Beam 16

2.1.1 The $\overline{p}$ Beam Energy 18

2.2 The Hydrogen Gas Jet Target 21

2.3 The E835 Detector 24

2.4 The Luminosity Monitor 29
2.5 Data Acquisition 32
2.6 Hardware and Software Trigger 34

3 The Central Calorimeter 41

3.1 Geometry and Electronics 41
3.1.1 Laser Monitor System 44
3.2 Clusterization 46
3.2.1 Isolated Clusters 47
3.2.2 Shared Clusters 50
3.2.3 Split Clusters 51
3.3 Calibration 52
3.4 Timing 53

4 The Background Calculation 57

4.1 The $\gamma\gamma$ Feeddown and the CCAL Simulation 58
4.2 The Feeddown Calculation 60
4.2.1 $\pi^0\pi^0$ Cross Section 60
4.2.2 $\pi^0\gamma$ Cross Section 63
4.2.3 $\gamma\gamma$ Feeddown 69
4.2.4 Feeddown Correction 69
4.2.5 Feeddown Systematic Error 75

5 $\gamma\gamma$ Analysis 78

5.1 $\gamma\gamma$ Cuts 78
5.1.1 $\gamma\gamma$ Efficiencies 82

5.2 $\gamma\gamma$ Data and Feeddown 84

5.3 $\gamma\gamma$ **Continuum** 86

6 Results **93**

6.1 Likelihood Fit 93

6.2 Interference and the $\cos\theta^*$ Cut 95

6.3 $\chi_0 \to \gamma\gamma$ **Partial Width** 99

6.4 Perturbative QCD and the Calculation of α_s 102

6.5 Conclusions 104

Appendix A. Random Gates **107**

Appendix B. Trigger Efficiencies **109**

Appendix C. Neutral DSTs **112**

References **115**

List of Tables

1.1 Theoretical predictions for the partial width $\chi_0 \to \gamma\gamma$ in keV. . . . 15

2.1 The design of the three types of FCAL blocks. 27

3.1 The specifications and geometry of each CCAL ring. 43

4.1 The inputs to the feeddown systematic error calculation. 75

4.2 The $\pi^0\pi^0$ cross section for different cuts. The systematic error is estimated to be $< 1\%$. 77

4.3 The $\pi^0\gamma$ cross section for different cuts. I estimate the systematic error is estimated to be 2.5%, mainly from the CL cut. 77

5.1 Energy sorted point-by-point results of $\chi_0 \to \gamma\gamma$ data and feeddown analyses up to $\cos\theta^* = 0.4$. 90

6.1 Results from the likelihood fits with and without interference. . . 96

6.2 A summary of the sources of systematic error in the $\chi_0 \to \gamma\gamma$ branching ratio. 99

6.3 Results of the fit to χ_0 measurements with and without the 2000 E835 results. 101

6.4 Summary of the χ_0 results from the 2000 run of E835. 101

6.5 Previous results for the partial width $\chi_0 \to \gamma\gamma$ in keV. 102

List of Figures

1.1 The fundamental particles of the standard model. 2

1.2 The strong coupling constant plotted versus energy. 3

1.3 Left: the (a) hadronic, (b) e^+e^- , and (c) $\mu^+\mu^-$ cross sections showing the ψ signal at the SLAC experiment (reference [4]). Right: the hadronic cross section revealing the ψ' signal (reference [5]). . . . 4

1.4 The e^+e^- invariant mass revealing the J signal at Brookhaven[6]. 5

1.5 Schematic diagrams of OZI suppressed (left) and allowed (right) decays. 7

1.6 The charmonium spectrum below the open charm threshold. . . . 8

1.7 The inclusive photon spectrum from Crystal Ball[12]. The cascades from ψ' to the triplet P states are clearly seen as well as their decays to the J/ψ 9

1.8 Left: First order e^+e^- charmonium formation. Right: Proton-antiproton annihilation charmonium formation via three gluons. . 10

2.1 A schematic of the antiproton source at Fermilab. 17

2.2 A scan of the ψ' resonance used to calibrate the absolute energy measurement. 19

2.3 A sample frequency spectrum. 19

2.4 A schematic of the Hydrogen gas jet target. 22
2.5 The gas jet nozzle showing how Hydrogen clusters form. 23
2.6 A schematic of the pumping system. 23
2.7 The pressure-temperature curve for the Hydrogen gas jet target. . 24
2.8 A plot of the beam current, and instantaneous luminosity. The luminosity remains nearly constant because the gas jet density is being continually increased. 25
2.9 The E835 Detector 26
2.10 A schematic of the E835 forward calorimeter. 28
2.11 The E835 Čerenkov detector. There is a disjoint septum separating the two chambers at $\theta \sim 36^o$. 29
2.12 A schematic of the E835 luminosity monitor 31
2.13 A sample spectrum from the luminosity monitor. 31
2.14 A schematic of the E835 DAQ. 33
2.15 The E835 neutral trigger logic. 35
2.16 A schematic of the CCAL summing algorithm creating super-blocks. 36
2.17 Top: The energy of electrons in the CCAL from J/ψ decay as a function of ring number. Bottom: The energy after being weighted as in the level-2 summer. After the weighting, it is feasible to use a single discriminator threshold for each super-ring. 37
2.18 The inputs and outputs of the NMLU. 39
3.1 A θ view of the Central Calorimeter. 42
3.2 A circuit diagram of the shaper boards. There were different configurations for each of the types of PMTs. 45

3.3 The CCAL pulse shape before and after the shaper board. 45

3.4 A schematic of the laser monitor. 46

3.5 Top: The ratio of measured/expected energy of J/ψ electrons in the CCAL as a function of their distance from the gap. Bottom: The same distribution after the energy correction algorithm. The energy lost in the gap is mostly corrected for. 49

3.6 A typical TDC turn-on curve. Ignore the point at 0 ADC counts. 55

3.7 A typical slew curve. The horizontal axis is ADC counts and the vertical axis is leading edge time. The fit is described in the text. 55

4.1 The $\pi^0\pi^0$ akinematics distribution. The small amount of background is subtracted from the signal as described in the text. . . . 61

4.2 The angular distributions of $\pi^0\pi^0$ data events (top), detection efficiency (middle), and cross section for a sample χ_0 stack. . . . 63

4.3 The $\pi^0\pi^0$ cross section for different $\cos\theta^*$ cuts plotted versus energy in the χ_0 region. The resonant $\chi_0 \to \pi^0\pi^0$ can be observed near 3415 MeV. 64

4.4 Top left: the $\pi^0\pi^0$ differential cross section. Top right: the $\pi^0\pi^0 \to \pi^0\gamma$ feeddown probability. Bottom left: the $\pi^0\gamma$ candidate events (error bars) and the calculated number of feeddown events from $\pi^0\pi^0$. Bottom right: feeddown subtracted $\pi^0\gamma$ differential cross section. 66

4.5 The $\pi^0\gamma$ candidate cross section (black circles), $\pi^0\pi^0 \to \pi^0\gamma$ feeddown cross section (open circles), and feeddown subtracted $\pi^0\gamma$ cross section (triangles). 67

4.6 The $\pi^0\gamma$ asymmetry. Negative asymmetry means the measured cross section is higher in the backward region. 68

4.7 The $\gamma\gamma$ feeddown calculation for a sample stack. Top: the $\pi^0\pi^0$ and $\pi^0\gamma$ differential cross sections. Middle: the $\gamma\gamma$ feeddown probabilities. Bottom: the calculated number of feeddown events. 70

4.8 The $\pi^0\pi^0$ (black triangles), $\pi^0\gamma$ (open triangles), and total $\gamma\gamma$ feeddown cross sections for $\cos\theta^* \leq 0.4$. 71

4.9 The cluster mass distribution for split and isolated π^0 clusters. The solid histogram is data; the dashed is from the fast Monte Carlo. . 72

4.10 The fraction of split π^0s in $\pi^0\pi^0$ and $\pi^0\gamma$ events for data (open circles) and fast Monte Carlo (solid circles). 74

5.1 The confidence level for $\gamma\gamma$ candidates after all other cuts are implemented. The arrow shows the cut at 0.1. 80

5.2 The invariant mass between the photon candidates and extra clusters in the event before and after the requirement on two in-time clusters. The arrows denote the π^0mass region. 80

5.3 The cluster mass distributions for shared photon candidates. Clockwise from top left: photon candidates from data, $\gamma\gamma$ Monte Carlo, $\pi^0\gamma \rightarrow\gamma\gamma$ Monte Carlo, $\pi^0\pi^0 \rightarrow\gamma\gamma$ Monte Carlo. The peak at high cluster mass in the $\pi^0\pi^0$ and $\pi^0\gamma$ come from coalesced π^0s which have a random gate nearby. 81

5.4 The angular distribution of $\gamma\gamma$ candidate events. 83

5.5 Top: $\gamma\gamma$ efficiency verses instantaneous luminosity. Bottom: $\gamma\gamma$ efficiency verses energy. 84

5.6 Top of each plot: Data and feeddown (dots) events versus $\cos\theta^*$ for different regions of $\sqrt{s}$. Bottom of each plot: Data−Feeddown. . 85

5.7 $\gamma\gamma$ cross section versus $\sqrt{s}$ for different slices of $\cos\theta^*$ 87

5.8 $\gamma\gamma$ cross section versus $\sqrt{s}$ for different integrals of $\cos\theta^*$ 88

5.9 Top: The $\gamma\gamma \to \overline{p}p$ cross section for $\cos\theta^*$ <0.6. Bottom: The $\gamma\gamma \to \overline{p}p$ cross sections for two different ranges of $\cos\theta^*$ 91

5.10 Top: the data (solid circles) and calculated feeddown (open circles) cross sections for $\cos\theta^*$ <0.6. Bottom: data-feeddown (points) with the fitted continuum cross section from VENUS. 92

6.1 The $\gamma\gamma$ spectrum fit as described in the text for $\cos\theta^*$ <0.4 with the interference terms free (solid) and without interference (dashed). 97

6.2 Two ranges of the $\gamma\gamma$ spectrum fit with (solid) and without (dashed) interference. 98

6.3 A summary of the measured $\Gamma_{\gamma\gamma}$ results along with the predicted values (dashed lines) compiled in table 1.1. The point labelled "New Fit" is the value derived from the semi-global fit described in the text. 103

6.4 The strong coupling constant versus energy scale. The line is the value of α_s ($\pm 1\sigma$) running from the Z_0. The value obtained from our $\gamma\gamma$ result is the solid circle at ~1.5 GeV. 105

A.1 The fraction of events without an in-time random cluster (open circles) and any random cluster (dark circles) as a function of instantaneous luminosity. This plot is made with 5/20 (seed/cluster) thresholds. 108

C.1 The neutral DST efficiency near the χ_0 (top) and for the entire range of data taken in the 2000 E835 run (bottom). 114

Chapter 1

Introduction

Particle physics is the study of the fundamental particles and their interactions. The theory describing our knowledge of particle physics is called the Standard Model. Arising from Gell-Mann's "Eight-Fold Way"[1], the Standard Model provides a basis for describing all phenomena except those where gravity is involved. In the model, there are 12 particles organized into three families of increasing mass. Each family consistes of two *quarks* and two *leptons*. For example, the family of the up and down quarks and the associated electron and electron neutrino. Each particle has an accompanying anti-particle with the same mass but opposite quantum numbers. In the model the particles interact via three forces: electromagnetic, weak, and strong. The electromagnetic force occurs between any two charged particles, mediated by the photon, and affects both quarks and the charged leptons. The weak force occurs between all particles in the Standard Model and it is responsible for nuclear decay. Neutrinos interact only via the weak force. The mediators of the weak force are the $W^{\pm}$ and the Z^0. The strong force occurs between the quarks and is the force that holds the nucleus together.

FERMIONS matter constituents spin = 1/2, 3/2, 5/2, ...

Leptons spin = 1/2			Quarks spin = 1/2		
Flavor	Mass GeV/c^2	Electric charge	Flavor	Approx. Mass GeV/c^2	Electric charge
ν_e electron neutrino	$<1\times10^{-8}$	0	u up	0.003	2/3
e electron	0.000511	−1	d down	0.006	−1/3
ν_μ muon neutrino	<0.0002	0	c charm	1.3	2/3
μ muon	0.106	−1	s strange	0.1	−1/3
ν_τ tau neutrino	<0.02	0	t top	175	2/3
τ tau	1.7771	−1	b bottom	4.3	−1/3

BOSONS force carriers spin = 0, 1, 2, ...

Unified Electroweak spin = 1			Strong (color) spin = 1		
Name	Mass GeV/c^2	Electric charge	Name	Mass GeV/c^2	Electric charge
γ photon	0	0	g gluon	0	0
W^-	80.4	−1			
W^+	80.4	+1			
Z^0	91.187	0			

Figure 1.1: The fundamental particles of the standard model.

The strong force is mediated by gluons. The properties of these particles are summarized in figure 1.1.

The electromagnetic and weak forces are well understood. Indeed, they have been shown to be two manifestations of the same force, called the electro-weak force[2][3]. The strong force, however, is much more complicated. The "constant" that dictates the strength of the strong interaction is not constant at all; it actually increases with distance (and inversely with the energy) between two quarks (figure 1.2). This leads to a phenomenon known as *confinement* and explains why quarks are found only in composite systems such as protons and neutrons and not as free particles. At very high energies (i.e. short distances), the coupling goes to zero leading to *asymptotic freedom*. This dissertation focuses on the charmonium system, a bound system of the charm and anticharm quarks, which is an excellent laboratory to study the nature of the strong force.

1.1 The Discovery of Charm

Late in 1974 a group led by Burton Richter at SLAC noticed an enhancement in the e^+e^- cross section in a very narrow energy region near the center-of-mass

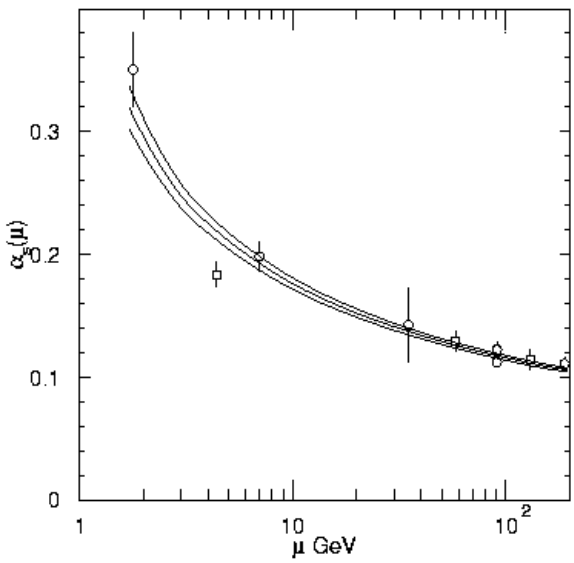

Figure 1.2: The strong coupling constant plotted versus energy.

energy 3.1 GeV[4] and another at 3.86 GeV[5] (figure 1.3). At the same time, Samuel Ting and his group at Brookhaven colliding protons on a beryllium target measured a similar enhancement in the e^+e^- final states with an invariant mass of 3.1 GeV[6] as shown in figure 1.4. In what later would be called the November Revolution, these two groups submitted their findings together in November, 1974 and the particle at 3.1 GeV was dubbed the J/ψ . The width of these resonances (initially believed to be 100 keV) was about 1000 times less than other known resonances in this energy region. Current models of the time were not sufficient to describe the narrowness of these resonances, which corresponded to unusually long lifetimes.

Earlier, in 1970, Glashow, Iliopoulos, and Maiani [8] had proposed an additional quark to go along with the up, down, and strange quarks known at the

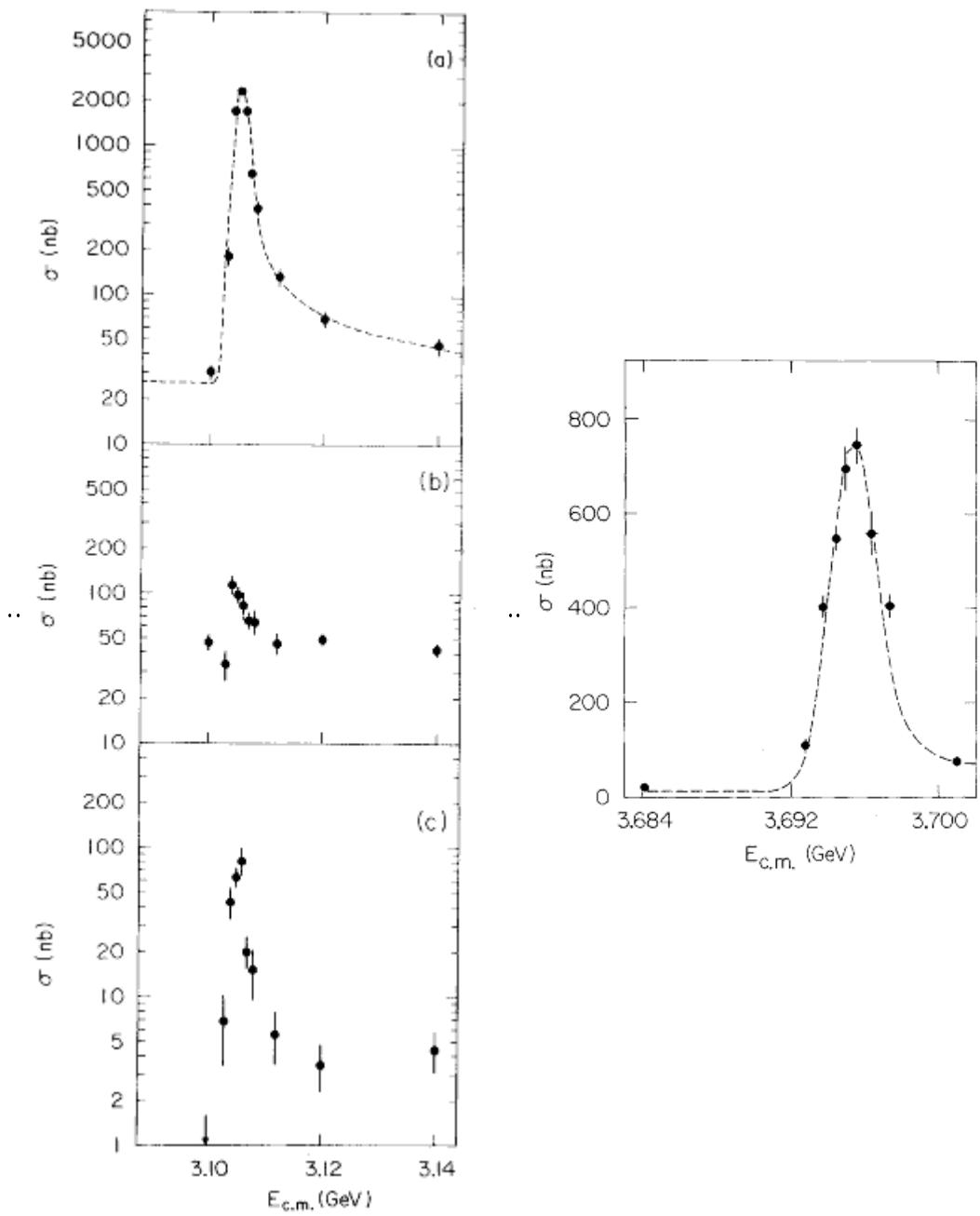

Figure 1.3: Left: the (a) hadronic, (b) e^+e^- , and (c) $\mu^+\mu^-$ cross sections showing the ψ signal at the SLAC experiment (reference [4]). Right: the hadronic cross section revealing the ψ' signal (reference [5]).

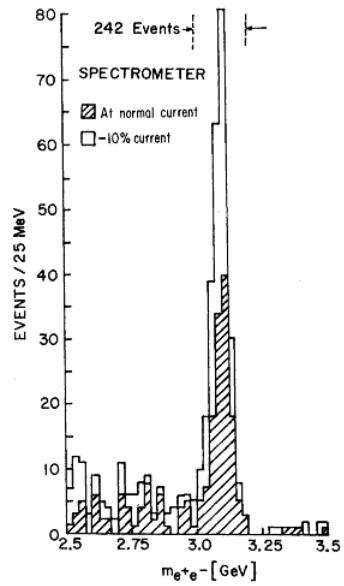

Figure 1.4: The e^+e^- invariant mass revealing the J signal at Brookhaven[6].

time as a way of explaining a strange phenomena in neutral Kaon decays. It had been observed that the decay rate for $K^+ \rightarrow \mu^+\nu_\mu$ (a strangeness changing charged current weak decay) was many orders of magnitude larger than the rate $K^0_L \rightarrow \mu^+\mu^-$ (a strangeness-changing neutral-current weak decay). According to Cabibbo theory, the coupling of the Z^0 to the quarks is:

$$J^0(q) = u\overline{u} - d\overline{d}\ cos^2\theta_c - s\overline{s}\ sin^2\theta_c - (s\overline{d} + \overline{s}d)sin\theta_c cos\theta_c[9],$$

while the charged current coupling is given by:

$$J^+(q) = u\overline{d}cos\theta_c + u\overline{s}sin\theta_c.$$

In both of these expressions the last term is the strangeness-changing term. The magnitudes of the two terms are comparable and a large difference in the charged and neutral current rates would not be expected.

Glashow, Iliopoulos, and Maiani proposed the existance of a fourth, up-like, quark and adding it to this picture changes things. There are now two doublets of quarks, (u,d) and (c,s). As in Cabibo theory, the d and s quark eigenstates for the weak interaction are mixtures of the mass eigenstates.

$$d' = dcos\theta_c + ssin\theta_c$$

$$s' = scos\theta_c - dsin\theta_c$$

Thus, the charged current is unchanged but the neutral current becomes:

$$\begin{aligned} J^0(q) &= u\overline{u} + c\overline{c} - (d\overline{d} + s\overline{s})\ cos^2\theta_c - (s\overline{s} + d\overline{d})\ sin^2\theta_c \\ &\quad -(s\overline{d} + \overline{s}d - s\overline{d} - \overline{s}d)sin\theta_c cos\theta_c \\ &= u\overline{u} + c\overline{c} - d\overline{d} - s\overline{s}. \end{aligned}$$

The introduction of the fourth quark produces an additional term in the neutral current that cancels with the strangeness changing term. This new quark was called "charm" because it "charms away" the neutral current contribution. In reality, the cancellation is not complete because there is a difference between the masses of the up and charm quarks.

While this procedure, known as the GIM mechanism, nicely described why the rate for strangeness changing neutral currents was so low, it came at a high cost: the introduction of an new, undetected particle of an unknown mass. The GIM mechanism remained a rather curious result and the proposed charm quark was not accepted until the discoveries at Brookhaven and SLAC, where it was quickly realized that the narrow resonances could only be explained by identifying the resonances as a bound state of charm and anti-charm quarks[10]. Later, as the $\overline{c}c$ system was better understood, it was dubbed charmonium in analogy to the e^+e^- bound state, positronium which showed a similar spectrum of states.

Figure 1.5: Schematic diagrams of OZI suppressed (left) and allowed (right) decays.

1.2 The $\overline{c}c$ System

The long lifetime of the J/ψ is due to two factors. The strong decay to charmed mesons is kinematically prohibited; the mass of the lightest charmed meson, the D^0, is more than half the mass of the J/ψ . In addition, the annihilation of the charm quarks to two or three hard gluons is suppressed due to the small coupling to high energy gluons. This effect is known as OZI (for Okubo, Zweig, and Iizuka) suppression[11] (figure 1.5). Therefore, since the OZI suppressed decay is the only one allowed, the lifetime is quite long. Above 3.8 GeV, the decay to charmed mesons is allowed so the states are much more short lived.

Like Hydrogen and positronium, charmonium has a spectrum of radial and orbital states. The J/ψ and ψ' are the two lowest lying states with $J^{PC}=1^{--}$. The charmonium states below the open-charm threshold are shown in figure 1.6. All of the states except the 1^1P_1 (h_c) and the 2^1S_0 ($\eta_c\prime$) have been confirmed and well measured.

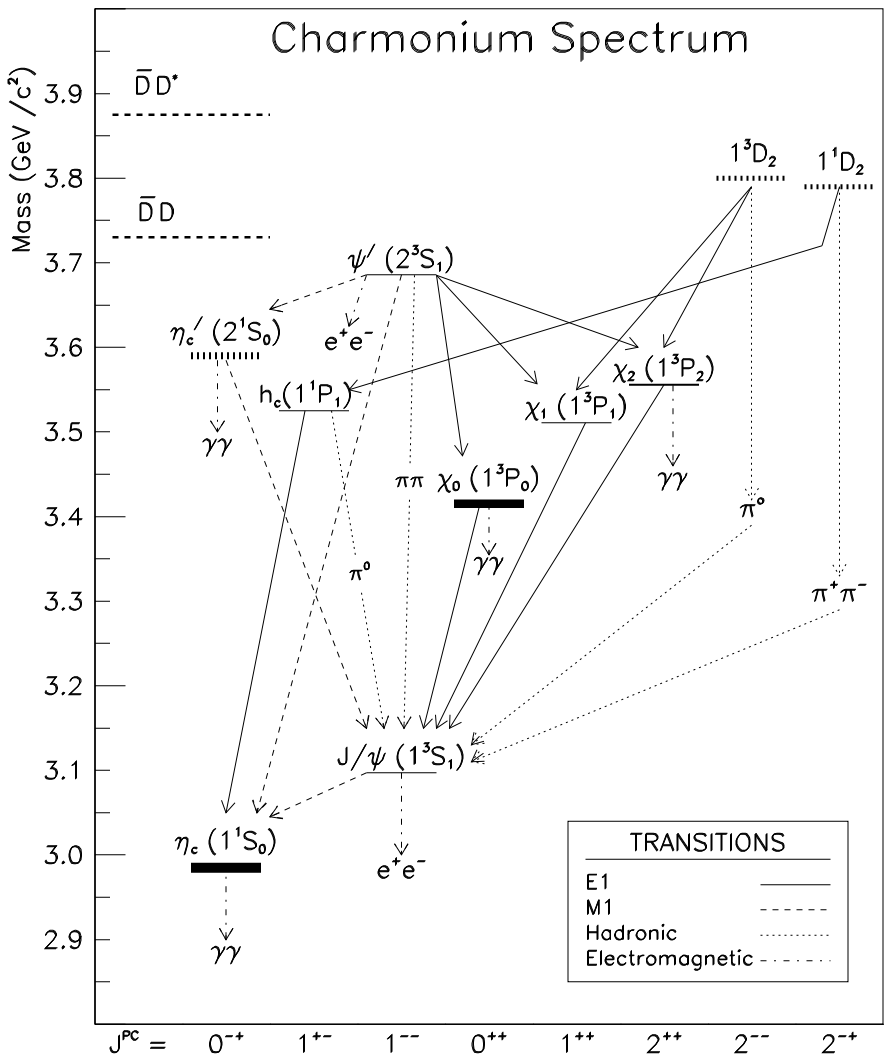

Figure 1.6: The charmonium spectrum below the open charm threshold.

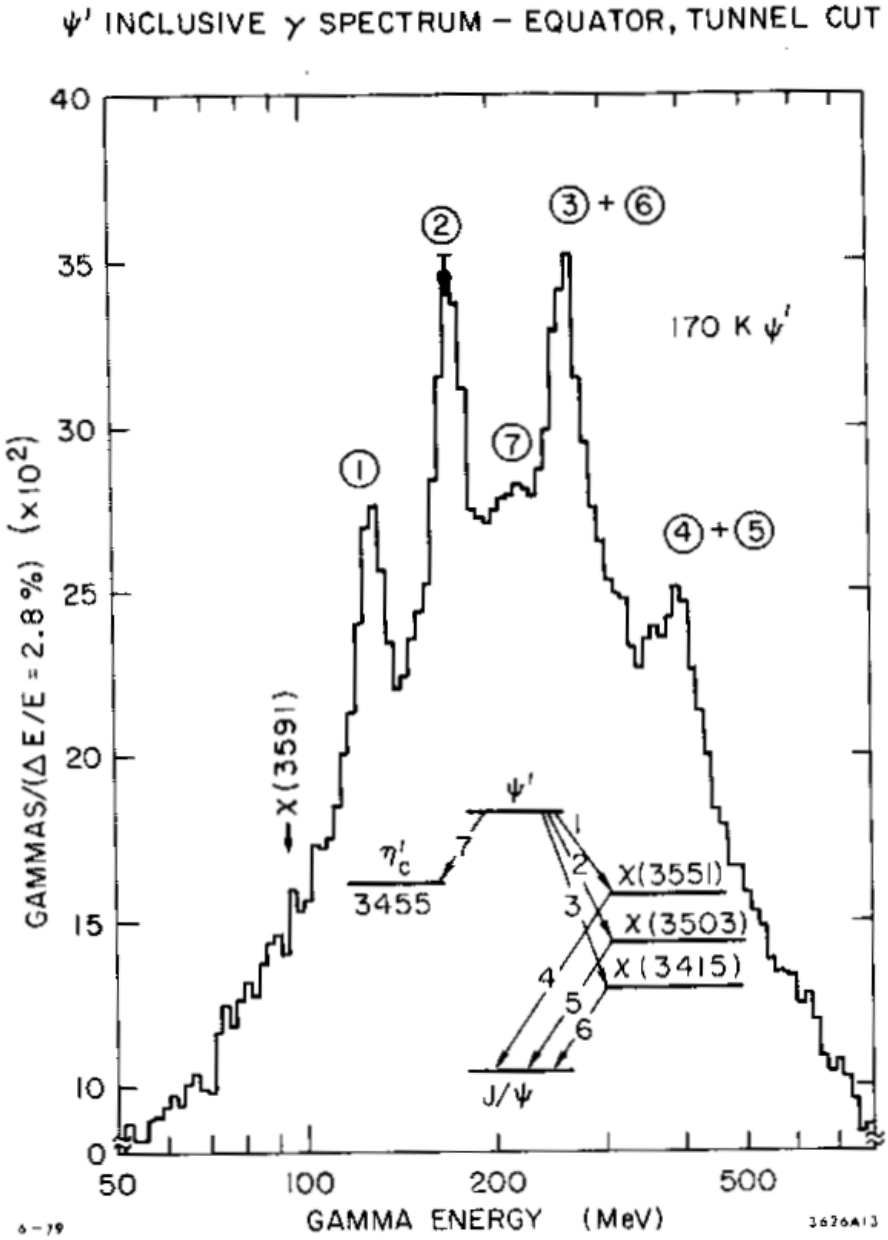

Figure 1.7: The inclusive photon spectrum from Crystal Ball[12]. The cascades from ψ' to the triplet P states are clearly seen as well as their decays to the J/ψ .

Figure 1.8: Left: First order e^+e^- charmonium formation. Right: Proton-antiproton annihilation charmonium formation via three gluons.

1.3 Charmonium Formation

The primary method for creating and studying charmonium states has been in e^+e^- collisions. The Crystal Ball experiment is the classic example of this method. At first order in the electromagnetic coupling constant, α, only those charmonium resonances with J^{PC} equal to that of the photon (i.e. 1^{--}) can be produced in e^+e^- annihilations (figure 1.8), though it is possible to create some of the other charmonium states via higher order interactions. The J=0 states can be produced via a second order diagram.

The primary method for studying charmonium in e^+e^- colliders is to tune the beams to the ψ' and observe the radiative decays to the lower energy states. Figure 1.7 shows photon spectrum from ψ' decays measured by the Crystal Ball experiment. The peaks in the spectrum are associated with transitions between different charmonium resonances. When studying the χ resonances in this way, the measurements of the resonance properties rely on, and are limited by, the resolution of the detector.

An alternative way of producing charmonium is by colliding protons with antiprotons (figure 1.8). The main benefit of using $\overline{p}p$ collisions is that all charmonium states can be directly created through the annihilation to 2 or 3 gluons since all quantum numbers are available in the initial state. Also, some of the

resonance parameters measured via $\overline{p}p$ collisions do not depend on the detector resolution but only on how well the beam energy is known.

The major drawback of using $\overline{p}p$ annihilations to create charmonium is that there is a large $\overline{p}p$ cross section to hadronic final states. The $\overline{p}p$ cross section is $\sim$60 mb at a center-of-mass energy of 3.0 GeV while the typical charmonium resonant cross section is $\sim$60 nb. However, the continuum cross section for $\overline{p}p \rightarrow e^+e^-$ is $\sim$5 pb while the cross section for $\overline{p}p \rightarrow \chi_0 \rightarrow J/\psi\ \gamma \rightarrow e^+e^-\ \gamma$ is $\sim$120 pb. Therefore, these experiments detect electromagnetic final states in order to overcome the large hadronic background.

1.4 Theoretical Predictions

The spectrum of radial and orbital excited states in the charmonium system closely resembles those of the positronium system. The primary difference is that charmonium is bound by the gluon exchange while positronium is bound by photon exchange. The mass splitting between radial excited states, which goes as $\sim$mv/c, implies that v/c$\sim$0.3. Thus, the charmonium system is approximately nonrelativistic. It is therefore natural to try to describe the charmonium spectrum using a non-relativistic potential model. By exploiting the analogy with positronium, first-order calculations of charmonium properties can be made.

There are many different versions of the potential which describe the data well. The most straightforward is the Cornell[13] potential:

$$V(r) = -\frac{4}{3}\frac{\alpha_s}{r} + kr \tag{1.1}$$

in which the first term of the potential is the analog to the electromagnetic potential corresponding to one gluon exchange which dominates at short distances.

The linear term dominates at long distances and describes multi-gluon exchange. This potential exhibits both characteristic properties of the strong interaction: asymptotic freedom at small distances and confinement at large separations.

More refined calculations are made using modified potentials which are typically split into vector and scalar parts. The single gluon exchange is included in the vector part while the confinement potential is at least partially scalar.

The charmonium Hamiltonian was derived by Schnitzer[14] and Pumplin *et al.*[15] to first order in $\left(\frac{v}{c}\right)^2$:

$$H = H_0 + H_1 + ... \tag{1.2}$$

where:

$$H_0 = \frac{p^2}{m} + V_s(r) + V_v(r) \tag{1.3}$$

and V_s and V_v are the vector and scalar terms respectively. H_1 has spin-independent and spin-dependent terms:

$$H_1 = H_{SI} + H_{SO} + H_{SS} + H_T. \tag{1.4}$$

The spin independent term is given by:

$$\begin{aligned} H_{SI} &= -\frac{p^4}{4m^3} + \frac{1}{4m^2}\{\frac{2L(L+1)}{r}V_v' + [p^2, V_v - rV_v'] \\ &\quad +2(V_v - rV_v')p^2 + \frac{1}{2}(\frac{8}{r}V_v' + V_v'' - rV_v'''\}. \end{aligned} \tag{1.5}$$

The spin-dependent terms lead to the fine and hyperfine splitting in the spectrum. The terms are:

$$H_{SO} = \frac{1}{2m^2 r}(3V_v' - V_s')\langle \vec{L} \cdot \vec{S} \rangle \tag{1.6}$$

$$H_{SS} = \frac{2}{3m^2}(\nabla^2 V_v)\langle \vec{S_1} \cdot \vec{S_2} \rangle \tag{1.7}$$

$$H_T = -\frac{1}{3m^2}(3V_v'' - \frac{V_v'}{r})\langle [3(\vec{S_1} \cdot \hat{r})(\vec{S_2} \cdot \hat{r}) - \vec{S_1} \cdot \vec{S_2}] \rangle. \tag{1.8}$$

The expectation values in the above equations are calculable. Thus, by measuring the mass splittings of the charmonium states, information can be obtained about the effective potential which in turn leads to valuable information about QCD.

1.5 Theoretical Predictions for $\Gamma_{\gamma\gamma}$

The topic of this thesis is the measurement of the $\chi_{c,0}$ (from now on refered to simply as the χ_0) decay rate to two photons. The $\gamma\gamma$ rate can give information on the nature of the strong interaction and can also be used to estimate the strong coupling constant at the charm quark mass. Again, as a starting point, we turn to the positronium system. For simplicity the $^1S_0$ decays will be described in detail.

The decay of positronium to two photons is a calculation that can be found in many Quantum Mechanics textbooks[16]. To lowest order, the decay of the ground state ($^1S_0$) is:

$$\Gamma(^1S_0 \to \gamma\gamma) = \frac{4\pi\alpha^2}{m_e^2}|\psi(0)|^2. \tag{1.9}$$

The 1S wave-function for positronium is known; it is the same as that of hydrogen corrected for the reduced mass.

To obtain the lowest order rate for charmonium decays, we simply replace the electron mass with the mass of the charm quark, α with $\frac{2}{3}\alpha$ (the charm quark has a charge of $+\frac{2}{3}$), and the e^+e^- wave-function with the charmonium wave function. We also need to add a factor of three corresponding to the three possible color states, thus:

$$\Gamma(\overline{c}c(^1S_0) \to \gamma\gamma) = \frac{64\pi\alpha^2}{27m_c^2}|\psi_{(\overline{c}c)}(0)|^2. \tag{1.10}$$

The decay to two gluons can be calculated in a similar way. A color factor of 9/8 must be added giving:

$$\Gamma(\overline{c}c(^1S_0) \to gg) = \frac{8\pi\alpha_s^2}{3m_c^2}|\psi_{(\overline{c}c)}(0)|^2. \tag{1.11}$$

Since the wave-function vanishes at the origin for P states, the $\gamma\gamma$ and gluon-gluon decay rates for the state studied in this thesis, the $\chi_0(^3P_0)$, involve the derivative of the radial wave-function at the origin. These rates are to lowest order:

$$\Gamma_0(\overline{c}c(^3P_0) \to \gamma\gamma) = \frac{16\alpha^2}{3m_c^4}|R'_P(0)|^2 \tag{1.12}$$

$$\Gamma_0(\overline{c}c(^3P_0) \to gg) = \frac{6\alpha_s^2}{m_c^4}|R'_P(0)|^2. \tag{1.13}$$

First order corrections within the framework of perturbative QCD have been calculated for the $\gamma\gamma$ and gluon-gluon rates[17]. The corrections are:

$$\Gamma_1(\overline{c}c(^3P_0) \to \gamma\gamma) = \Gamma_{0,\gamma\gamma}\left(1 + \frac{0.2\alpha_s}{\pi}\right) \tag{1.14}$$

$$\Gamma_1(\overline{c}c(^3P_0) \to gg) = \Gamma_{0,gg}\left(1 + \frac{9.5\alpha_s}{\pi}\right). \tag{1.15}$$

The wave function contains the long distance non-perturbative effects which cannot be reliably calculated. We can, however, use the ratio $\Gamma_{\gamma\gamma}/\Gamma_{gg}$ to obtain a measurement of α_s. In the ratio, the wave-function and charm quark mass cancel leaving an expression that only depends on α and α_s. The ratio is given as:

$$\frac{\Gamma_{\gamma\gamma}}{\Gamma_{gg}} = \frac{8\alpha^2}{9\alpha_s^2}\frac{\left[1 + \frac{0.2}{\pi}\alpha_s\right]}{\left[1 + \frac{9.5}{\pi}\alpha_s\right]}. \tag{1.16}$$

The perturbative QCD approach works well for S-wave decays but for P-wave decays to light hadrons it leads to divergences. These divergences suggest that there are non-perturbative effects that cannot be accounted for solely in

the wave-function. More recent calculations of the quarkonia decay rates have been performed using the effective field theory formalism of non-relativistic QCD (NRQCD) as developed by Bodwin, Braatan, and Lepage[18]. While the PQCD approach assumes quarkonium is purely a color singlet $Q\overline{Q}$ pair, NRQCD adds an additional color octet term corresponding to $Q\overline{Q}g$. Thus, there are two non-perturbative parts in the decay to light hadrons:

$$\Gamma(\chi_0 \to LH) = 2Imf_1(^3P_0)H_1 + 2Imf_8(^3S_1)BH_8 + O(v^2) \tag{1.17}$$

and the infrared divergences found in using just the color singlet hypothesis go away. The short distance coefficients, f_1 and f_8, are found using perturbative QCD. The non-perturbative factors, H_1 and H_8, are determined from decays of the χ_1 and the χ_2.

Using this formalism, the $\chi_J \to \gamma\gamma$ decay rates have been calculated. The measurement of the $\gamma\gamma$ rate has been said to be an excellent test of NRQCD. The most fully developed prediction has been made by Chao and Huang [19] who include next-to-leading order QCD corrections.

Explicitly relativistic approaches have also been attempted, most notably by Munz[21]. Table 1.1 summarizes the predictions for the $\chi_0 \to \gamma\gamma$ partial widths. The Bodwin, Braatan, and Lepage prediction uses $\Gamma_{\chi_0} = 9.8 \pm 1.0$ MeV.

	$\Gamma_{\gamma\gamma}$ (keV)
Chao[19] *et al.*	3.72±1.11
Gupta[20] *et al.*	6.38
Munz[21]	1.39±0.16
Bodwin[18] *et al.*	6.67±2.77
Barnes[22]	1.56

Table 1.1: Theoretical predictions for the partial width $\chi_0 \to \gamma\gamma$ in keV.

Chapter 2

Experiment E835

The E835 experiment was designed to study the charmonium states by intersecting a virtually monoenergetic antiproton beam with a molecular hydrogen gas jet. By changing the energy of the beam, the charmonium resonance can be scanned. In order to suppress the huge non-resonant hadronic background, the E835 detector is designed to detect electromagnetic final states. This is accomplished with a pair of lead glass calorimeters and a threshold Čerenkov detector, for electron detection. In addition, there is a series of charged track detectors. In this chapter, we will describe the E835 beam, target, and detector and the system used to collect the data.

2.1 The Antiproton Beam

E835 uses the antiproton beam at the Antiproton Accumulator at Fermilab (figure 2.1). Antiprotons are created by colliding pulses of 120 MeV protons from the Main Injector with a nickel target. The particles produced in the collision are focused using a lithium lens (a cylinder of lithium with longitudinal current

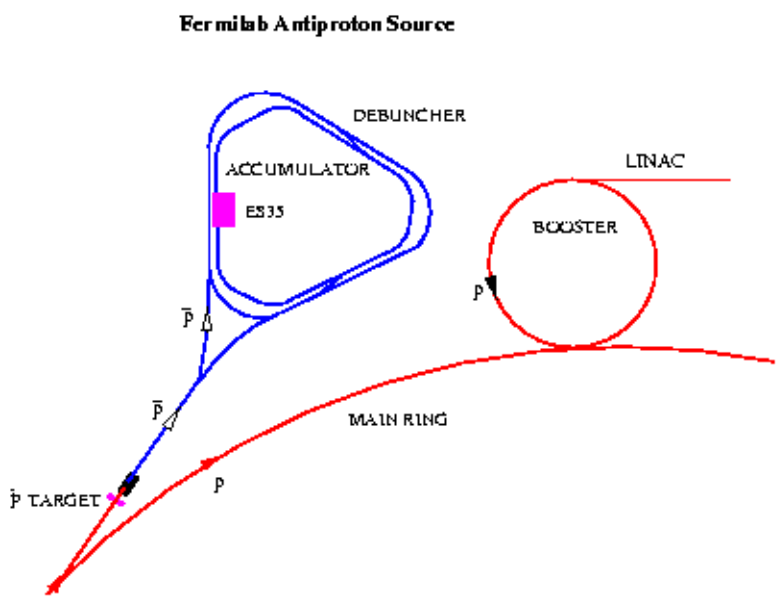

Figure 2.1: A schematic of the antiproton source at Fermilab.

passing through, creating an azimuthal magnetic field). Dipole magnets are used to steer 8.9 GeV antiprotons into the Antiproton Debuncher. Here, the beam is cooled stochastically to reduce the momentum spread, $\frac{\Delta p}{p}$, from 4% to 0.2%. In doing so, the bunch structure of the beam coming out of the main injector is lost giving a continuous beam of antiprotons. The beam is then sent into the accumulator where it is further cooled to $\frac{\Delta p}{p}$ ~0.04%.

The process of creating antiprotons and transferring them into the accumulator is known as *stacking*. The accumulator is capable of holding 8×10^{11} antiprotons which corresponds to a *stack* of 80 mA. E835 typically took data with a stack of 30-50 mA of antiprotons which normally took about 10 hours of stacking to create.

When the stack is the appropriate size, the beam is decelerated from 8.9 GeV/c

to the desired momentum. For instance, for the χ_0 resonance (3.415 GeV), the beam momentum is 5.195 GeV/c. Deceleration is performed by slowly reducing the current in the accumulator's bending magnets. During data taking, stochastic cooling is used to restore the energy lost due to multiple scattering between the beam with the gas jet target and the small amount of excess gas in the beampipe[1].

2.1.1 The $\overline{p}$ Beam Energy

An accurate measurement of the antiproton beam energy is crucial to this method. The energy of the antiproton beam is given by $E=\gamma m_p$ where γ is the relativistic factor. The velocity of the antiprotons is $v=L\times f$ where f is the circulation frequency and L is the orbit length of the beam. The frequency is measured with a series of pick-ups connected to spectrum analyzers. The spectrum analyzers measure the frequency of the beam to an accuracy of 10 parts-per-billion. The exact orbit is measured using a series of beam position monitors (BPMs) placed around the accumulator from which the path width is found. The 48 horizontal BPMs are able to measure the position of the beam to within $\pm$1mm.

The BPMs can only give a relative position measurement. In order to calibrate the length measurement, an energy scan of the ψ' resonance is performed (figure 2.2). The position of the beam given by the BPMs at the peak of the ψ' corresponds to a center-of-mass energy of 3.68596 GeV. All lengths are then measured with respect to this reference orbit. Thus, L is given as $L=L_0+\delta L$, where L_0 is the reference orbit length. The error in the length measurement gives an error in the center-of-mass energy of $\pm$0.15 MeV at the ψ' resonance.

[1]The pressure in the beampipe is $\sim 3\times10^{-10}$ torr

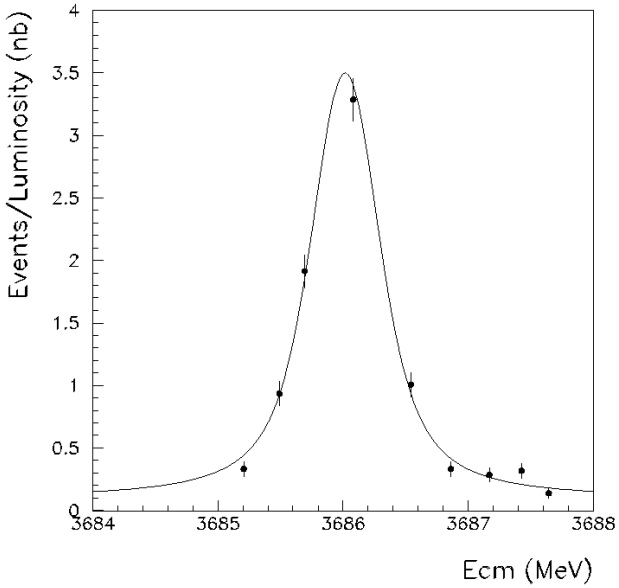

Figure 2.2: A scan of the ψ' resonance used to calibrate the absolute energy measurement.

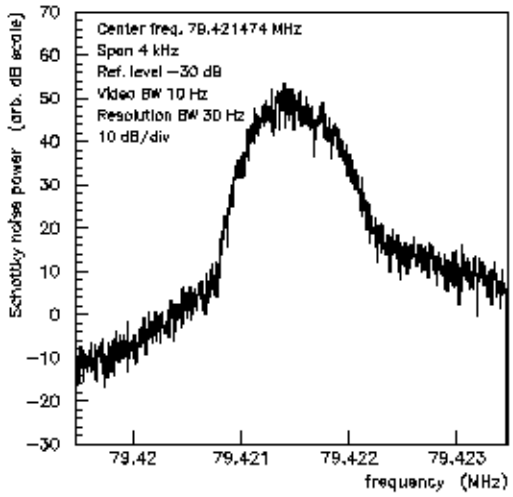

Figure 2.3: A sample frequency spectrum.

For narrow resonances, the energy spread of the beam is important in measuring the resonance parameters. By measuring the frequency spectrum of the circulating beam, the energy spread can be derived. The momentum spread of a circulating beam is:

$$\frac{dp}{p} = -\frac{1}{\eta}\frac{df}{f} \tag{2.1}$$

The slip factor η is a parameter depending on the configuration of the accumulator and is given by:

$$\eta = \frac{1}{\gamma_t^2}\frac{1}{\gamma^2} \tag{2.2}$$

where γ is the relativistic factor, $\gamma = \frac{E_{cm}}{m_p}$. There are a number of different ways to measure γ_t or, equivalently, η[23]. Near $\gamma = \gamma_t$, the beam becomes very unstable and the energy measurement becomes unreliable. This has been a problem in past E835 runs, but for the 2000 run all data was taken at energies well above the transition energy.

A resonance can be scanned using the tunable antiproton beam. By counting the number of observed events per energy point, the resonance parameters can be extracted by fitting:

$$N_i = L_i \times \epsilon_{tot} \times \alpha[\sigma_{bkg}(\sqrt{s_i}) + \sigma(\sqrt{s_i})] \tag{2.3}$$

to a Breit-Wigner resonance using maximum likelihood methods. In the equation, i corresponds to the energy point, L_i is the integrated luminosity for the energy point, ϵ_{tot} is the total detection efficiency, α is the geometric acceptance, and σ_{bkg} is the background cross section. The observed resonance cross section, $\sigma(\sqrt{s_i})$, is a Breit-Wigner convoluted with the beam width and is given by:

$$\sigma(\sqrt{s}) = \int_0^\infty \sigma_{BW}(E')G(E' - \sqrt{s})dE \tag{2.4}$$

$$\sigma_{BW} = \frac{4\pi(2J+1)}{4(s-4M_p^2)}\frac{\Gamma_R^2 B_{in}B_{out}}{(\sqrt{s}-M_R)^2 + \Gamma_R^2/4}. \tag{2.5}$$

Here, G(E-$\sqrt{s}$) is a Gaussian function of energy with the width of the beam as derived from the frequency spectrum measurement. In practice, the convolution of the beam width ($\sim$1 MeV) with the BW resonance is only important for fairly narrow resonances like the ψ' or the χ_2 whose widths are $\sim$0.4 and 2.0 MeV respectively. The effect on the measurement of the parameters of the χ_0, which has a width of 10 MeV, is very small but the convolution is included in the calculation for completeness.

2.2 The Hydrogen Gas Jet Target

Hydrogen gas for charmonium experiments was first used in 1984 by R704[24] at CERN. The target for E835, as well as its predecessor E760, is a collimated jet of pressurized hydrogen gas[25]. Figure 2.4 shows a schematic of the gas jet target. The nozzle of the gas jet is shaped like a trumpet and the large change in pressure between the two sides of the nozzle causes the H_2 gas to form clusters (figure 2.5) of $\sim 10^7$ molecules with a very narrow velocity distribution. The gas jet intersects the anti-proton beam perpendicularly with a width of $\sim$7 mm at the interaction region . An elaborate series of molecular pumps (figure 2.6) are used to minimize the density of stray gas. This is important in order to ensure all of the $\overline{p}p$ interactions occur in the interaction region and also to maximize the beam lifetime.

The density of the gas jet ranges from $1.0 \times 10^{13} - 3.2 \times 10^{14}$ atoms/cm^3 and is adjustable by varying the pressure and temperature. Figure 2.7 shows a diagram of the pressure/temperature dependence of the density. The dark solid line is the gas/liquid phase transition. Going below the line into the liquid phase increases the chance of the nozzle becoming clogged which causes erratic behavior in the

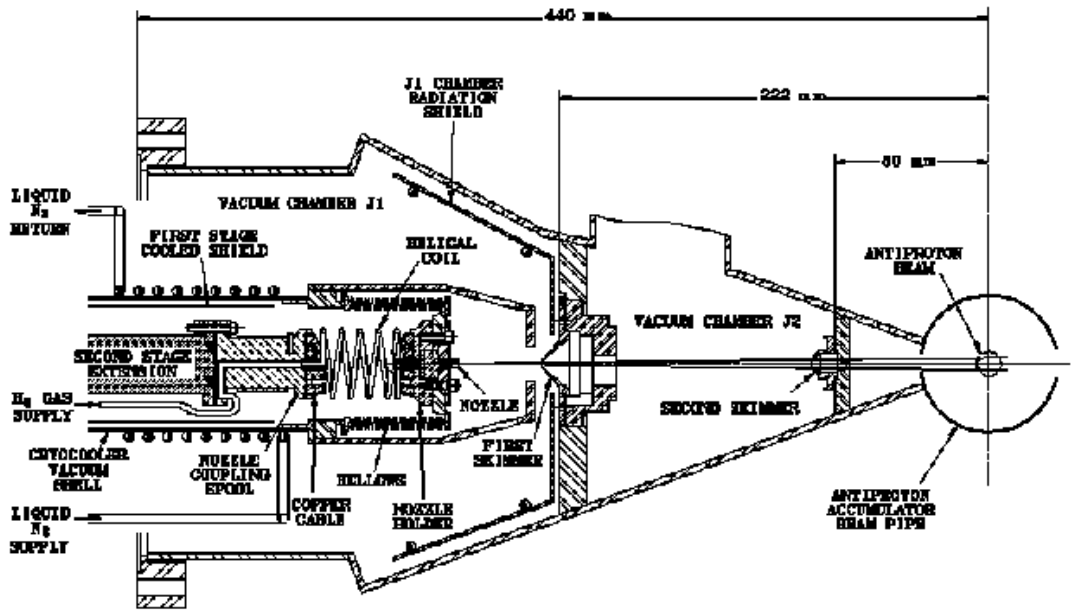

Figure 2.4: A schematic of the Hydrogen gas jet target.

interaction rates. This is characterized by long stretches of low rates interspersed with very high rates as the jet spits out a high density ball of Hydrogen. The detector was not designed for this type of running so the pressure and temperature of the jet was always adjusted to stay away from this region.

To avoid rate dependent systematic effects it is important to maintain a reasonably constant interaction rate over the course of a stack. During data taking, the current in the antiproton ring would continuously decrease due to interactions with the gas jet target. To maintain a constant instantaneous luminosity, the density of the gas jet was increased to offset the beam loss. This was achieved by continuously changing the temperature and pressure of the jet. Figure 2.8 shows the beam current, the jet density, and the nearly constant instantaneous luminosity over an entire stack.

Figure 2.5: The gas jet nozzle showing how Hydrogen clusters form.

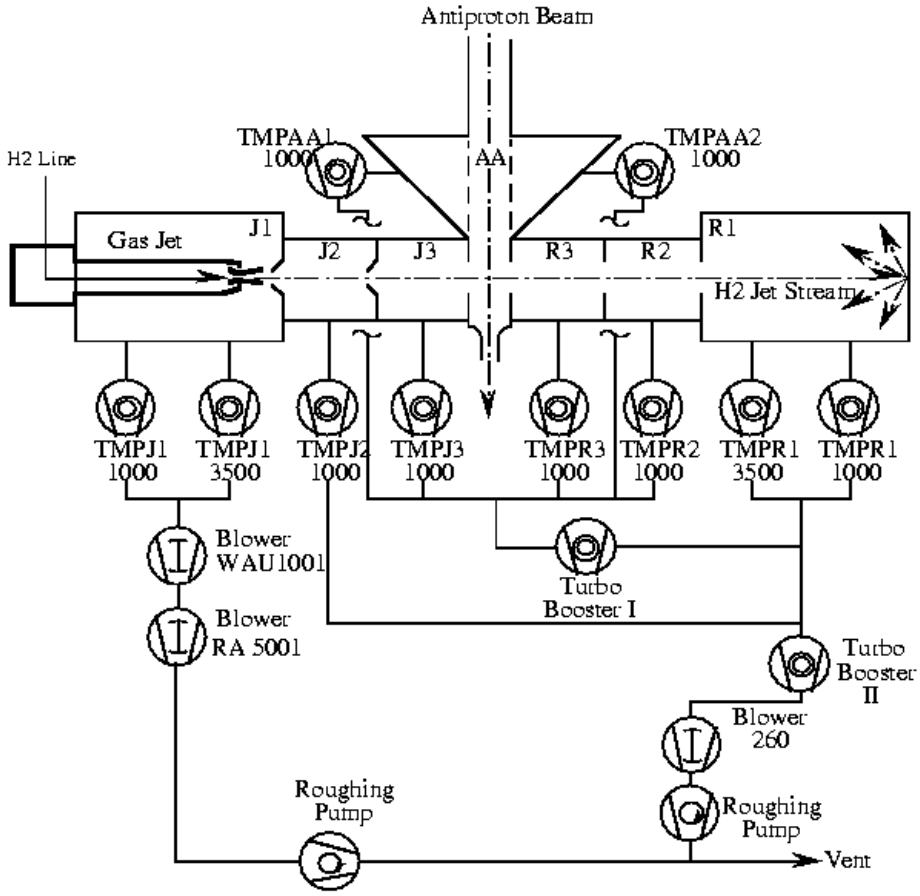

Figure 2.6: A schematic of the pumping system.

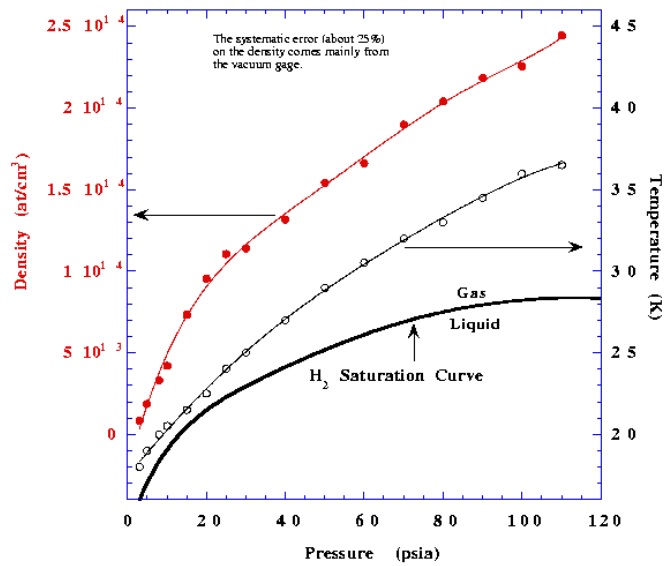

Figure 2.7: The pressure-temperature curve for the Hydrogen gas jet target.

2.3 The E835 Detector

The goal of the E835 detector was to detect charmonium resonances from $\overline{p}p$ collisions amid an enormous hadronic background. To this end, the detector (figure 2.9) was optimized for the detection of electromagnetic final states. Of primary importance for the neutral decays are the Central and Forward Calorimeters (CCAL and FCAL respectively) which were arrays of lead-glass blocks covering polar angles, measured from the beam axis, of 2-70° in the lab with full azimuthal coverage. The CCAL will be discussed in chapter 3.

The FCAL (figure 2.10) was a planar array of 144 SF2 lead-glass blocks made by Schott Glass. Three different sizes of blocks were used and two types of PMTs, summarized in table 2.1. Using $\overline{p}p \rightarrow 3\pi^0 \rightarrow 6\gamma$ events, the energy resolution of the FCAL was determined to be $\frac{\sigma_E}{E} = \frac{6\%}{\sqrt{E}} + 4\%$ and the position resolution was 2.0

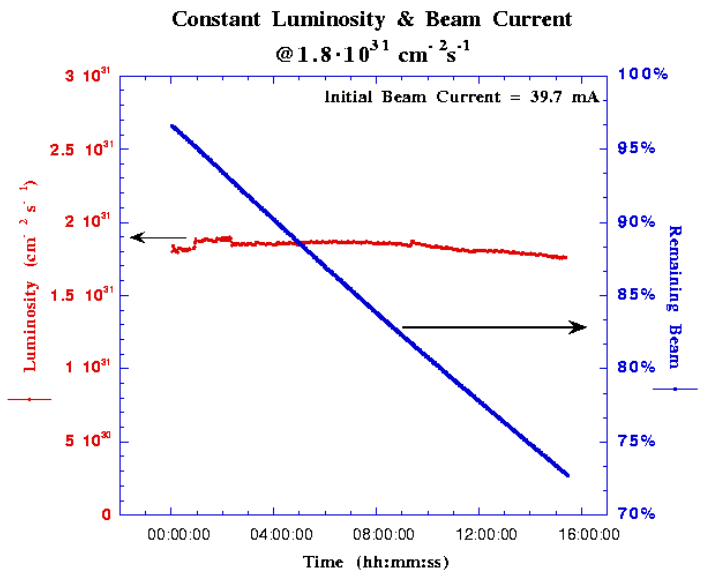

Figure 2.8: A plot of the beam current, and instantaneous luminosity. The luminosity remains nearly constant because the gas jet density is being continually increased.

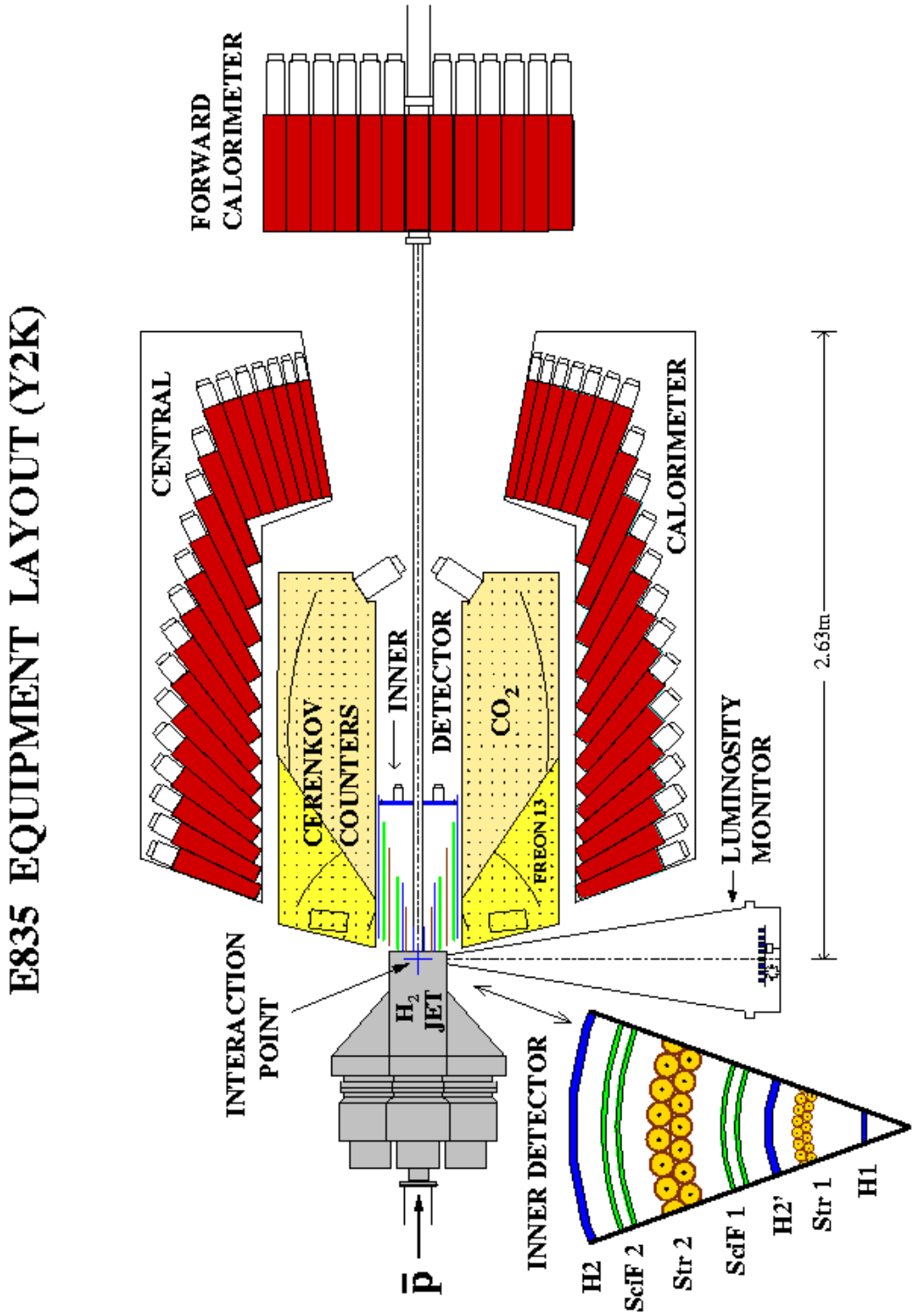

Figure 2.9: The E835 Detector

	Width (cm)	Length (cm)	Rad. Lengths	PMT
Small (48)	6.3	58.6	21	RCA 6342A ($2\frac{1}{2}$")
Medium (80)	10	38	14	RCA 6342A ($2\frac{1}{2}$")
Large (16)	15	36	13	RCA 4335 (5")

Table 2.1: The design of the three types of FCAL blocks.

cm[26]. Energy calibration of each block was performed using $\overline{p}p \rightarrow 3\pi^0 \rightarrow 6\gamma$ events when one of the photons was found in the FCAL by using the 5 photons in the CCAL to determine the FCAL photon energy[27].

Inside the central calorimeter are concentric layers of charged track detectors. These detectors provide information about tracks emanating from the interactin region. The inner tracker consists of three sets of hodoscopes, three sets of scintillating fibers, and two sets of straw chambers. There is also a threshold Čerenkov detector used for electron identification.

The three sets of hodoscopes, H1, H2 and H2$'$, are used for preliminary selection charged events and to perform a dE/dx measurement to aid in electron identification. They are composed of long strips of scintillating plastic oriented parallel to the beam pipe and connected to photomultiplier tubes through lightguides.

Measuring the azimuthal angle ϕ of charged particles are two sets of straw chambers[28]. Each chamber contains two staggered layers of proportional drift tubes, 64 total in each chamber. Three sets of scintillating fibers[29] measure θ with a resolution of $\sim$ 0.7 mrad. . The fibers cover the polar range $15^o < \theta < 65^o$. The light produced by a charged particle passing through a fiber is detected by cryogenic visible light photon counters (VLPCs)[30].

A key part of the charged tracker is the Čerenkov detector (figure 2.11)[31].

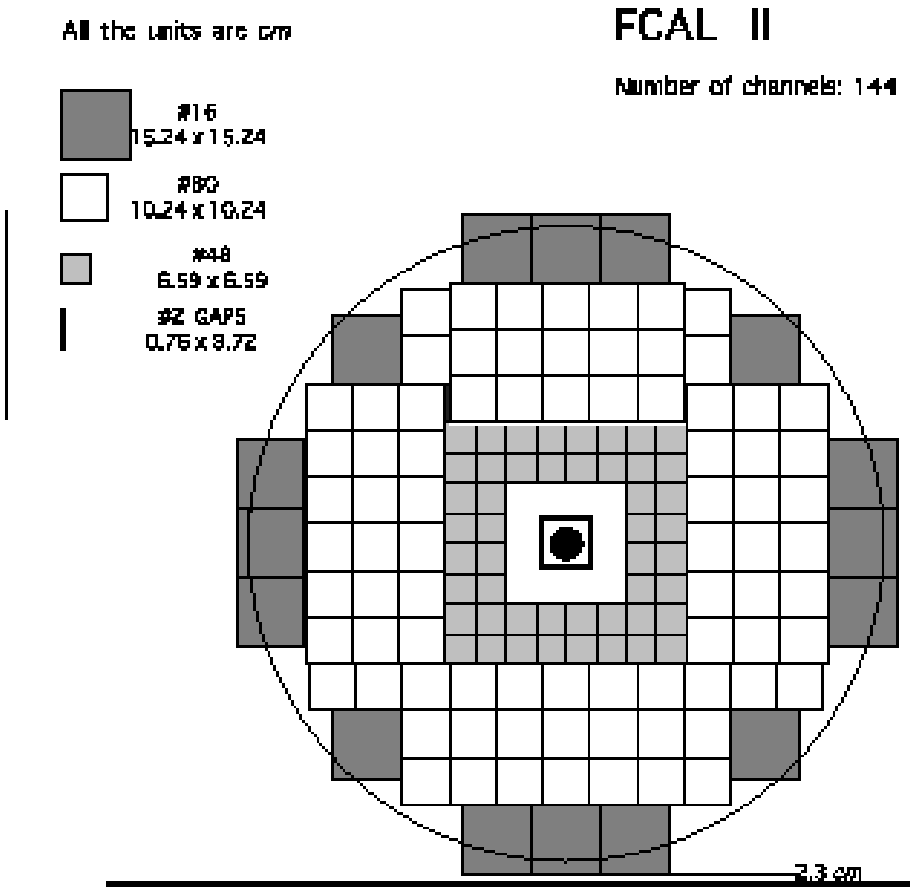

Figure 2.10: A schematic of the E835 forward calorimeter.

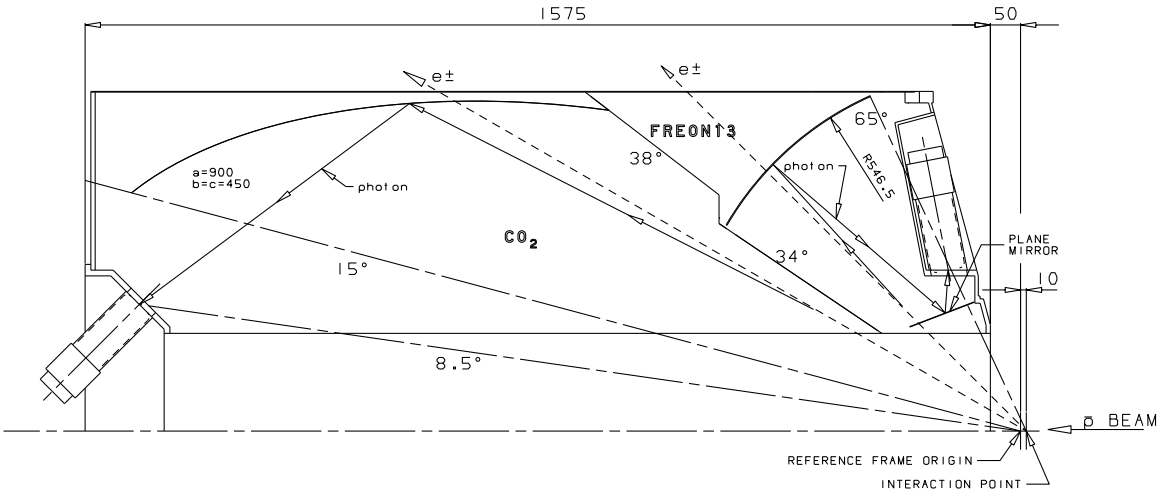

Figure 2.11: The E835 Čerenkov detector. There is a disjoint septum separating the two chambers at $\theta \sim 36^o$.

The Čerenkov detector consists of 2 sets of 8 cells (octants) each and has a coverage of 15-65 degrees. Between the forward and backward octant, there is a septum. The septum is disjoint so that a particle must go through at least one of the octants. The detector operates as a threshold Čerenkov detector such that it gives a signal for electrons and positrons but not for charged pions or muons which pass through. It is important for detecting electrons from J/ψ and ψ' decays.

2.4 The Luminosity Monitor

An absolute luminosity measurement is essential in order to obtain a proper normalization for charmonium cross section measurements. The luminosity monitor[32] measures the slow moving recoil protons from the most forward $\overline{p}p$ elastic scattering. For forward scattering, where the momentum transfer is very small, the interaction is almost entirely electromagnetic. The differential cross section is

given as:

$$\frac{d\sigma}{dt} = |F_c(t)e^{i\delta} + F_n(t)|^2 \tag{2.6}$$

where t is the momentum transfer (GeV^2) of the reaction (related to the angle of scattering) and F_c (F_n) is the Coulombic (nuclear) amplitude of the interaction. The Coulombic contribution is ~95% of the total cross section at small momentum transfers (recoil angle ~90° in the lab) and can be calculated exactly.

The nuclear amplitude can be parameterized as:

$$F_n(t) = \sigma_t(\rho + i)e^{\frac{-b|t|}{2}}/4\sqrt{\pi}\hbar c. \tag{2.7}$$

The three parameters σ_t, ρ, and b have been measured elsewhere [33]. The luminosity is found from the number of forward scatters via the equation:

$$\mathcal{L} = \frac{\mathcal{N}}{(\mathrm{d}\sigma/\mathrm{dt})(\mathrm{dt}/\mathrm{d}\Omega)\mathrm{d}\Omega}. \tag{2.8}$$

The luminosity monitor used a series of solid-state detectors situated near 90° in the lab. It sat directly below the interaction region and was connected to the beampipe via an evacuated horn (figure 2.12). There were 5 detectors directly underneath the beamline and one each on the left and right at 3.496^o and 3.511^o respectively. The asymmetry between the left and right detectors were used to measure any radial beam shifts.

Figure 2.13 shows a sample recoil spectrum measured by the luminosity monitor. There is a background of ~2-3% which is subtracted from the peak. The detector is able to measure the absolute luminosity to within ~2.5%. This error in the luminosity measurement is primarily due to the uncertainty of the size and location of the opening between the beampipe and the luminosity monitor.

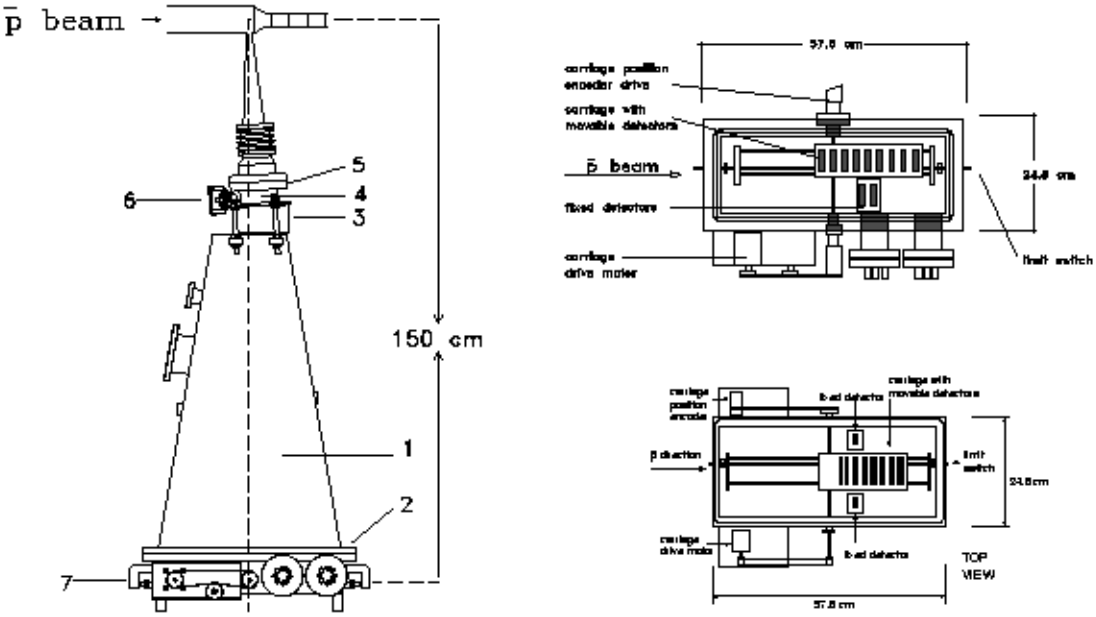

Figure 2.12: A schematic of the E835 luminosity monitor

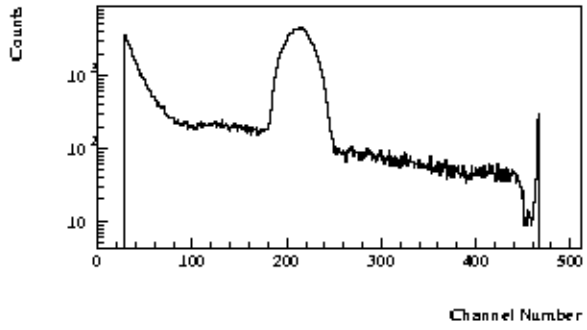

Figure 2.13: A sample spectrum from the luminosity monitor.

2.5 Data Acquisition

The data acquisition system acquires data from four different sources: event data, beam parameter data (ACNET), luminosity monitor data, and scaler data. The event data stream is based on the Fermilab product DART (data acquisition at fixed target). The beam parameter data was delivered via ethernet from the Fermilab beams division. The luminosity monitor and scaler data were recorded and transferred to the computer using CAMAC.

E835 used 163 ADC (LRS4300), 66 TDC (LRS3377), and 23 PCOS (LRS2731) modules in 14 CAMAC crates[2]. There were 3 CAMAC branches which were accessed through two 411 Jorway Interfaces. Since the backplane readout of the CAMAC crate is too slow, the data from the modules were read out through the front ECL ports and stored in a DYC module in each crate. The DYC acts as a temporary buffer, storing the 16-bit input data in a 32-bit FIFO. In each CAMAC crate, the readout modules and the DYC controller are daisy-chained together. The layout of the hardware is shown in figure 2.14.

When an event occurs, the trigger logic programmed into the Master MLU (memory lookup unit) sends a signal to the DYCs telling them to read out the data. The DYC sends the first module a readout-enable signal, prompting its data to be sent to the DYC controller. When the first module has finished sending its data, it sends a pass signal, enabling the next module in the chain to send its data. During readout, the trigger logic received a busy signal to prevent data from piling up.

All of the DYCs are connected to one of the two DC2/DM115 modules. Connected to each DC2 module are two 32MB dual ported memory (DPM) modules

[2]LeCroy Corporation, Chestnut Ridge, NY.

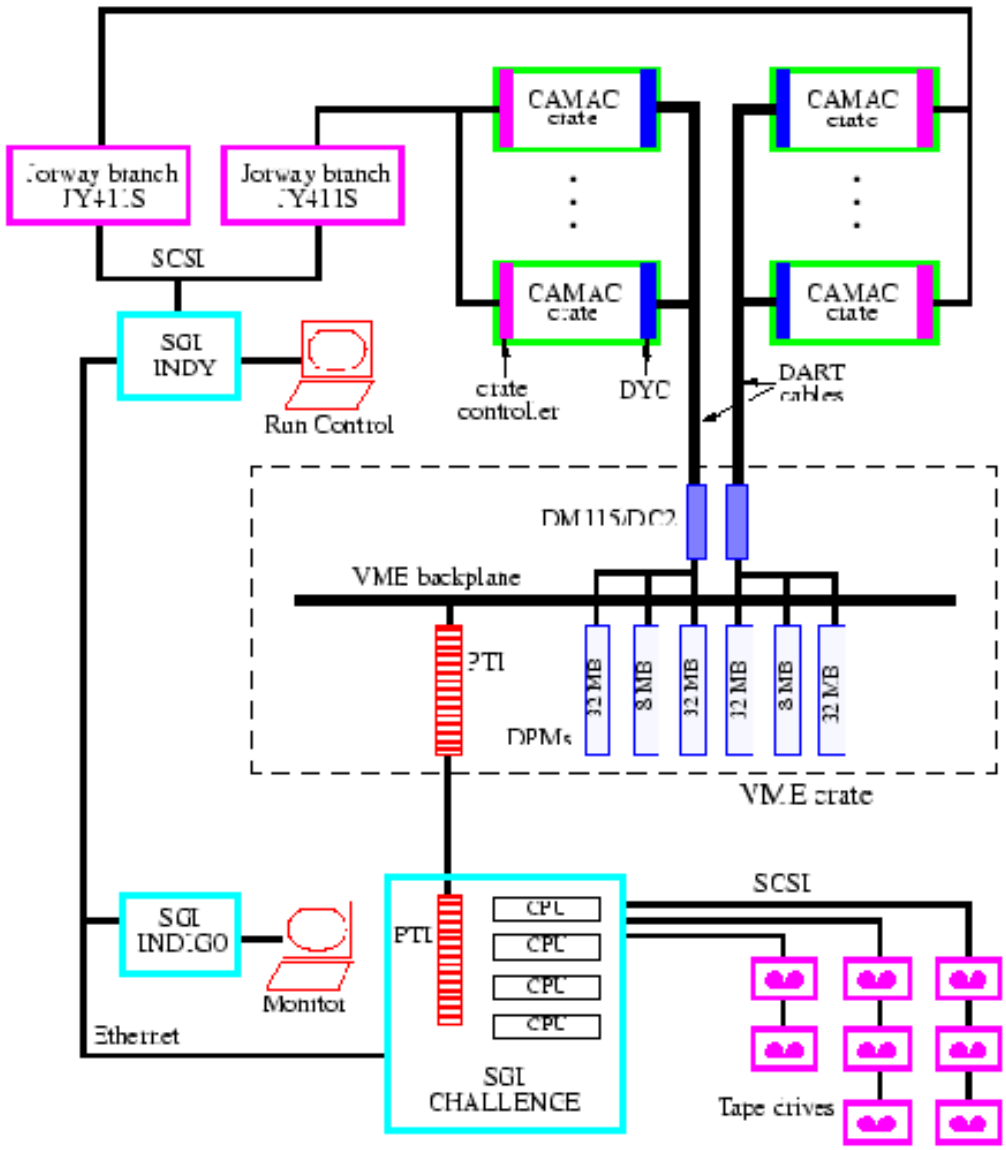

Figure 2.14: A schematic of the E835 DAQ.

and a single 8MB DPM. The DC2 reads out the DYCs and stores exactly N events, a number chosen by the experimenter, into one of the 32MB DPMs. When the N events are written, it begins writing to the other 32MB DPM. There is a process called the *gateway* running on the SGI Challenge that reads out the DPM that is not being written to. The gateway and the DC2 communicate as to which DPM is ready to be read via the 8MB DPM.

The gateway writes the DC2 data to two memory buffers on the SGI Challenge. At this point, each buffer contains roughly half the data from the same N events. Using synchronization numbers provided by the DYCs, the buffers are combined to give N whole events. A unique event header is stamped onto each event with information such as event number, run number, and time.

Each event is then analyzed with an online filter program, one process of which is normally running on each of the 10 CPUs of the SGI Challenge. The online filter will be discussed in the next section. If the event passes the filter, it is sent to one of three streams GK, GN, or GP (for e^+e^- , neutral, and $\phi\phi/\overline{p}p$ respectively) and written to tape. In addition, there are a number of sub-streams used for detector calibration and a quick analysis of the data which are also written directly to disk.

2.6 Hardware and Software Trigger

A hardware trigger is used to select events of interest from an interaction rate of 3 MHz. Due to bandwidth limitations the maximum data rate is limited to 2.5 kHz. There are two broad trigger types in E835: charged and neutral. The charged trigger is designed to locate three classes of events. One of these triggers requires pairs of electrons, for example from $\chi_x \rightarrow J/\psi\ \gamma \rightarrow e^+e^-\ \gamma$. There is also logic in

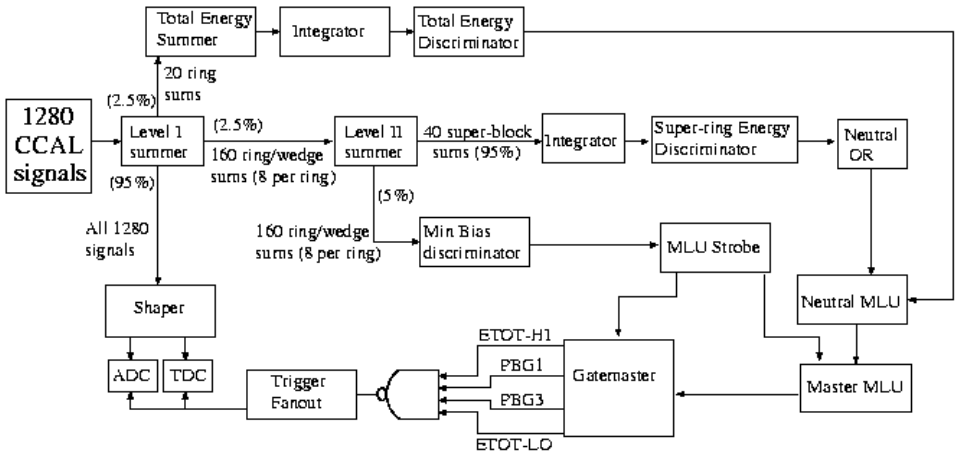

Figure 2.15: The E835 neutral trigger logic.

the trigger to detect the hadronic $\phi\phi$ states, for instance $\overline{p}p \rightarrow \eta_c \rightarrow \phi\phi \rightarrow 4K^{+/-}$. A detailed description of the charged trigger can be found in reference [34].

For the $\gamma\gamma$ channel the neutral trigger is used. The neutral hardware trigger uses the CCAL signals to trigger on accept events which satisfy one of two criteria. The total energy trigger (ETOT) sums all of the energy in the calorimeter and passes the event if it is above a certain threshold. The PBG trigger selects events with two large back-to-back energy deposits.

The logic of the neutral trigger is displayed in figure 2.15. It begins by splitting each CCAL signal into three parts: 95%/2.5%/2.5%. The 95% of the signal goes into shaper boards and then into the ADC and TDC. One the 2.5% fractions is input to a summer which adds up all of the energy in each ring, resulting in 20 ring energy sums. The energy used for the ETOT trigger is then taken to be the energy sum of rings 1-18.

The remaining 2.5% of the signal is used for the PBG trigger. For the purpose

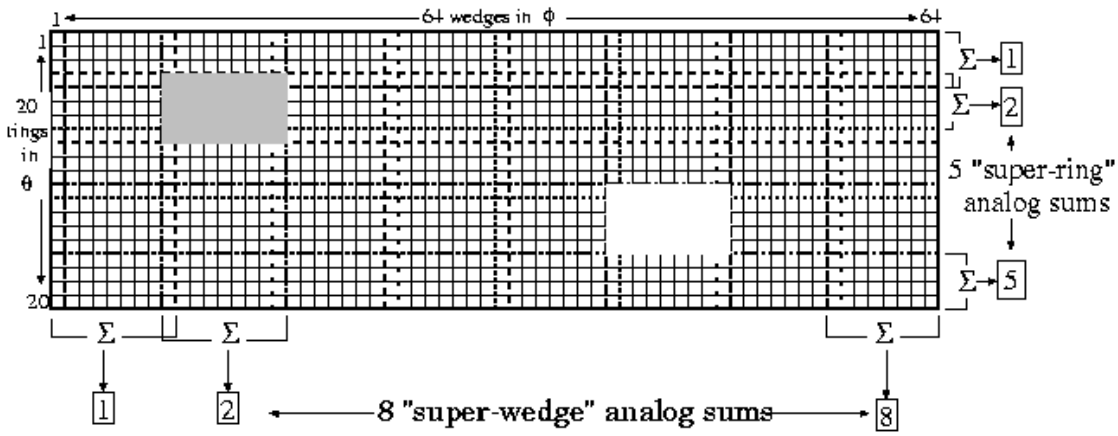

Figure 2.16: A schematic of the CCAL summing algorithm creating super-blocks.

of triggering, the calorimeter is reduced to 40 *super-blocks*, illustrated in figure 2.16. First, the level-1 summer combines the 64 signals for each ring into eight signals, leaving 160 total signals. These signals are divided with 5% being sent to the minimum bias discriminator. If two of the signals arriving at the minimum bias discriminator are above a threshold, a signal (the strobe) is sent enabling the MMLU. The remainder of the signal is sent to the level-2 summer which takes the eight sums/ring and adds them with a weighted sum ring-wise into five super-ring sums. This leaves 40 super-blocks which are sent to a discriminator and then to the neutral MLU (see below). A weighted sum is used because while the photon energy increases with decreasing θ, it is convenient to use a single discriminator threshold. Figure 2.17 shows a diagram of energy vs ring number. Note that each super-block has an overlap of one block in each the ring and wedge directions. This is in order to avoid trigger inefficiencies when a photon hits near a boundary between super-blocks.

The logic for the level-1 hardware neutral trigger is contained in the neutral

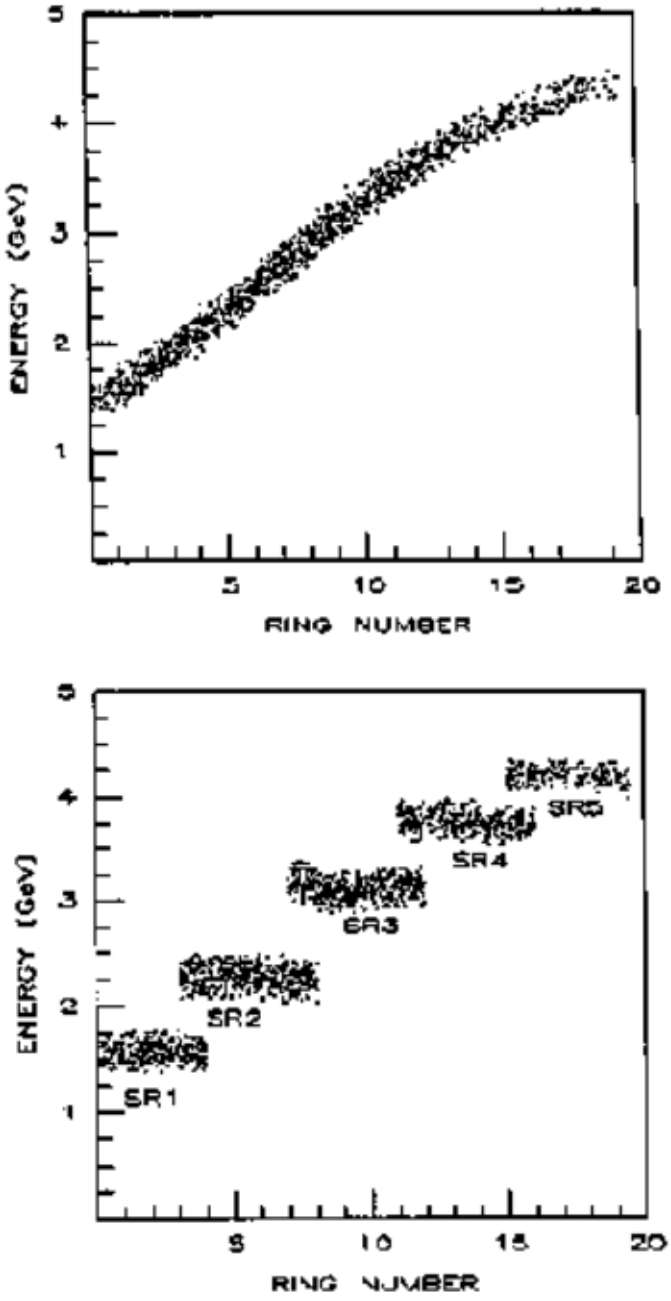

Figure 2.17: Top: The energy of electrons in the CCAL from J/ψ decay as a function of ring number. Bottom: The energy after being weighted as in the level-2 summer. After the weighting, it is feasible to use a single discriminator threshold for each super-ring.

MLU. The first eight inputs of the NMLU (figure 2.18) correspond to a logical-OR of the five discriminated super-block signals in each super-wedge. The other two inputs of the NMLU correspond to ETOT inputs.

There are four logic outputs of the NMLU.

- PBG1: This is true if there are at least two above threshold hits in back-to-back super wedges i.e. the event is consistent with two-body kinematics.
- PBG3: Looser than PBG1, only requires a corresponding hit in one of the three opposing super wedges.
- ETOT-HI: The total energy in the CCAL (rings 1-18) is >80% of the available energy.
- ETOT-LOW: The total energy in the CCAL (rings 1-18) is >70% of the available energy. This is used for efficiency studies.

The outputs of the NMLU are sent to the master MLU. The MMLU is the logic module that send out the main (level-2) hardware trigger. As well as inputs from the NMLU, it also takes signals from the charged and $\phi\phi$ MLUs. There are two triggers from the MMLU which are used in the $\gamma\gamma$ analysis.

- $\gamma\gamma$ trigger: $PBG1 \oplus \overline{H1 \cdot H2'} \oplus \overline{FCH}$
- $ETOT - HI \oplus \overline{H1 \cdot H2'} \oplus \overline{FCH}$

Here $H1$, $H2'$, and FCH signify an OR of the discriminated signals in H1 and H2$'$ hodoscopes and in the forward charged veto respectively. Thus $\overline{H1 \cdot H2'} \oplus \overline{FCH}$ vetoes on charged particles. There are six other triggers sent out by the MMLU, charged and efficiency triggers, which were not part of the data collection used for theis analysis and will not be discussed.

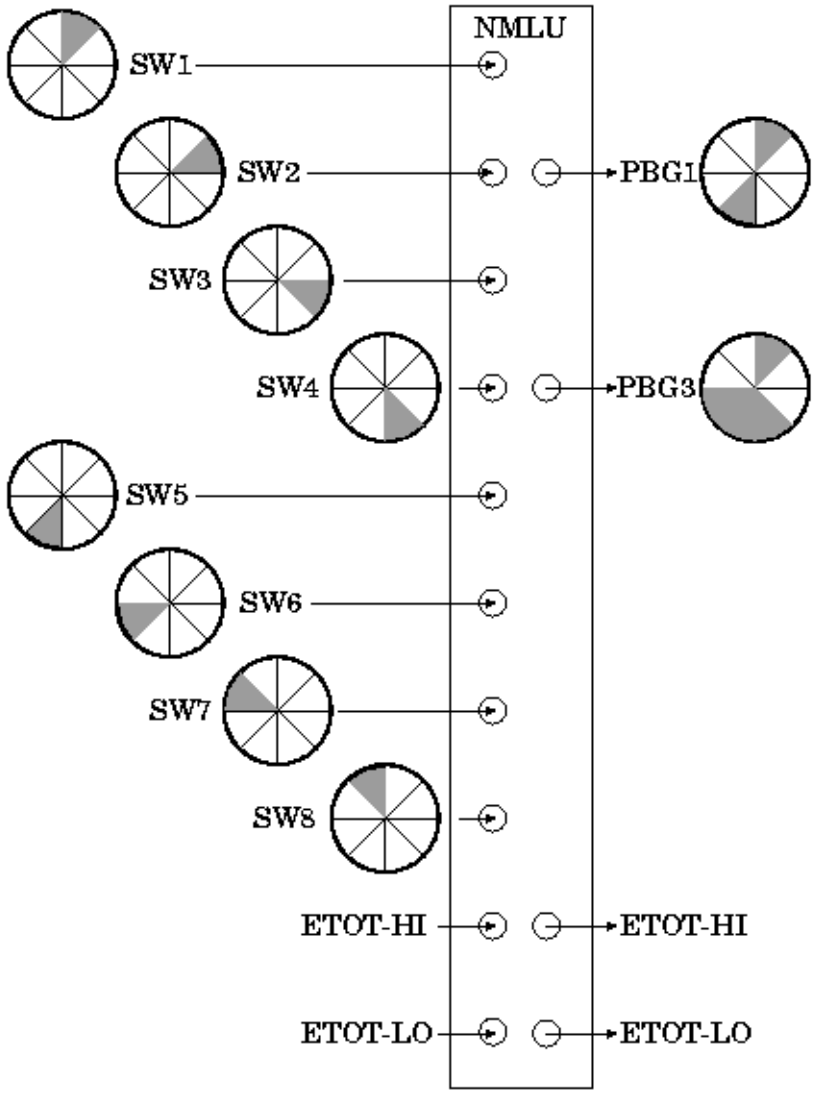

Figure 2.18: The inputs and outputs of the NMLU.

When a level-2 trigger is sent out from the MMLU or elsewhere [3], the gatemaster polls the DYCs and collects the results from the ADCs and TDCs. This data is sent to the software trigger which is an online selection program called PRUDE (Program Rejecting Unwanted Data Events).

The algorithm in PRUDE is a crude event reconstruction. In the algorithm, PRUDE finds local maxima above 50 MeV in the CCAl and sums the energy in the 3x3 grid around it, creating simple clusters. The values for θ and ϕ of each cluster are computed with an energy weighted average.

Then based on this information, useful events are selected and their type is determined. In the $\gamma\gamma$ analysis, there are two criteria that are used. If the invariant mass between any two clusters is greater than 2.2 GeV and the event is neutral, the event is kept and labelled as a "gold gg" event. This is the data sample used for the $\gamma\gamma$ candidates. The algorithm also selects events with π^0s or ηs in the event. This data sample is important because, as will be shown in Chapter 4, $\pi^0\pi^0$ and $\pi^0\gamma$ events are a significant source of background for the $\gamma\gamma$ signal.

[3]The minimum bias, laser monitor, and the random gate triggers have their own hardware. The minimum bias trigger is the OR of the 160 level 1 summer outputs, pre-scaled by a large factor. The laser monitor and random gate triggers come from pulsers, 0.1 Hz and 10kHz respectively.

Chapter 3

The Central Calorimeter

This chapter describes the main electromagnetic calorimeter used in E835, the CCAL. For two photon physics, the CCAL provided most of the information about the events. Special emphasis will be placed on those functions of the CCAL which impact the two photon analysis. In particular the calibration, the clusterization algorithm, and the timing of the detector will be discussed in detail.

3.1 Geometry and Electronics

The CCAL consisted of 1280 lead glass blocks arranged in 20 rings of 64 blocks each covering polar angles $70^o > \theta > 10^o$ (figure 3.1). The blocks were made of Schott F2 lead-glass which has a density of 3.61 g/cm^3 and a radiation length of 3.141 cm. The blocks ranged in length from 12 to 16 radiation lengths with the shorter blocks at larger theta. The CCAL blocks were tapered and aligned to point back to the interaction point. The block cross section decreased with θ so that each ring covered approximately the same interval in cosθ. There was a layer of steel between each ring (0.254 mm) and wedge (1.470 mm) for structural

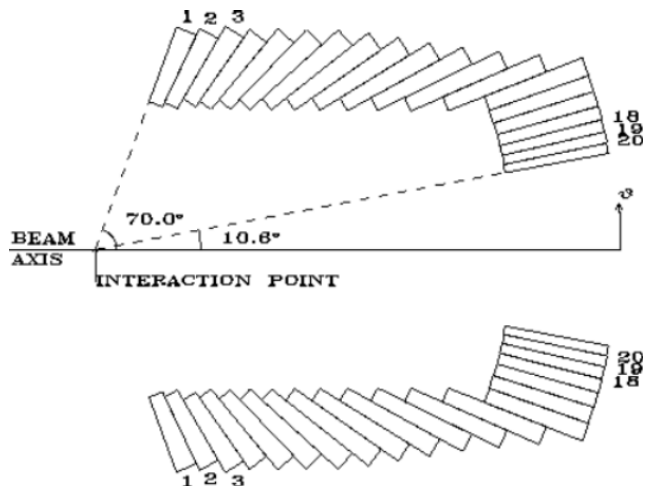

Figure 3.1: A θ view of the Central Calorimeter.

support.

A photomultiplier tube was glued at the end of each block. Four sizes of PMTs were used with diameters ranging from 1.5" to 3.0" with the fractional area covered by each PMT ranging from 47% to 66%. The PMTs had bi-alkali photocathodes with a sensitive range of 300-600 nm.

The energy resolution of the CCAL was measured for E760 in an electron beam and was found to be:

$$\frac{\sigma(E)}{E} = \frac{0.06}{\sqrt{E(GeV)}} + 0.014 \ . \tag{3.1}$$

The angular resolutions of a reconstructed shower in θ, ϕ were 6 mrad and 11 mrad respectively. They were checked *in situ* by using a clean sample of the two body reaction $\psi' \rightarrow e^+e^-$. The results were consistent within errors with the resolutions obtained in the electron beam.

The output signal from each PMT (after being split for the neutral trigger) was delayed so that the signal arrived at the ADCs coincident with the trigger. This

Ring	Length (cm)	Central θ (degree)	$\Delta\theta$ (degree)	Distance from Vertex (cm)	PMT Diameter (in)	PMT Coverage (%)
1	37.80	67.387	5.226	72.44	3.0	47.3
2	38.65	62.259	5.030	75.87	3.0	47.5
3	39.88	57.342	4.803	80.07	3.0	47.6
4	41.50	52.664	4.552	85.08	3.0	47.8
5	43.54	48.246	4.284	90.96	3.0	47.9
6	46.03	44.101	4.007	97.79	3.0	48.1
7	48.98	40.234	3.728	105.62	3.0	48.2
8	50.00	36.644	3.451	114.54	3.0	49.7
9	50.00	33.327	3.183	124.66	3.0	52.0
10	50.00	30.273	2.925	136.07	3.0	54.4
11	50.00	27.472	2.679	148.89	3.0	56.8
12	50.00	24.908	2.449	163.26	3.0	59.3
13	50.00	22.567	2.233	179.34	3.0	61.7
14	50.00	20.434	2.033	197.28	3.0	64.1
15	50.00	18.493	1.848	197.29	2.5	54.6
16	50.00	16.730	1.678	197.29	2.5	66.4
17	50.00	15.131	1.522	197.30	2.0	52.7
18	50.00	13.679	1.380	197.30	2.0	64.4
19	50.00	12.364	1.250	197.30	1.5	44.3
20	50.00	11.174	1.131	197.30	1.5	54.3

Table 3.1: The specifications and geometry of each CCAL ring.

was achieved with ~300 feet of delay cable. The impedence of the cable causes dispersion of the signal pulse causing it to develop a long tail. At high rates, a second signal may occur before the first had been fully discharged, leading to an error in the measurement of the charge in the signal by the ADC. In order to circumvent this, the delayed signal was treated with an amplifier(figure 3.2) with a short shaping time such that it acted to restore the pulse shape, increasing the pulse height and decreasing the length of the tail while keeping the integral of the charge contained in the pulse constant (figure 3.3). The shaped pulse was then sent to the FERA ADC for integration. A discriminator built onto the shaper board supplied a timing pulse that was sent to the TDC.

3.1.1 Laser Monitor System

A laser monitoring system was used to test all of the block/tube assemblies prior to running in 2000 and also during the run to monitor the gains of each block. The laser system is shown in figure 3.4. A Nitrogen laser, emitting a wavelength of 337 nm, was pulsed onto a block of plastic scintillator whose scintillation light was in the blue region at ~430 nm. The scintillation light was then transmitted through a mixing bar coupled to 64 optical fibers. The fibers (one for each wedge) were transmitted by a second mixing bar where it was again split into 20 signals. These fibers were attached to the back of each CCAL block. Additionally, there were a number of fibers attached to the major mixing bar for use in the FCAL in the same manner.

The laser pulse was initiated by a pulser running at 0.1 Hz and the signals in the PMTs were collected on a special trigger initiated by the same pulser. The width of the laser pulses was ~3 nm and the amplitudes were monitored with a

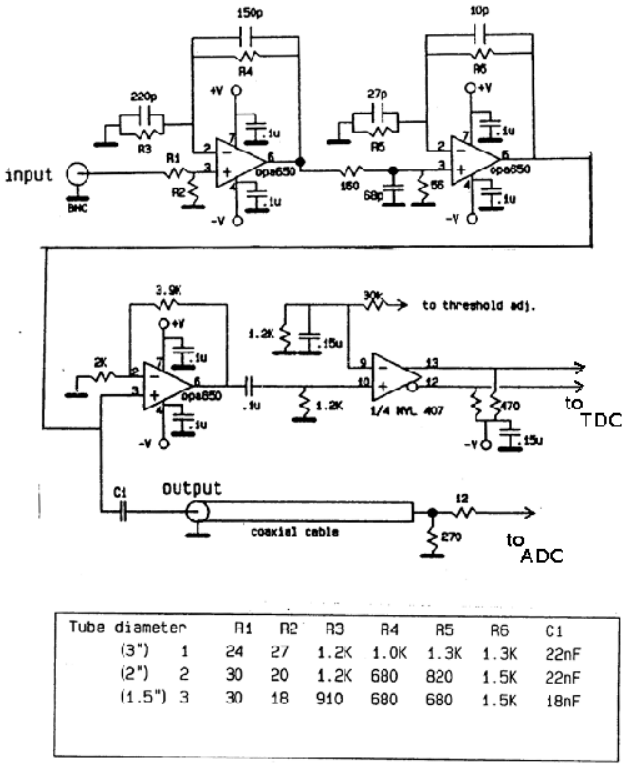

Tube diameter		R1	R2	R3	R4	R5	R6	C1
(3")	1	24	27	1.2K	1.0K	1.3K	1.3K	22nF
(2")	2	30	20	1.2K	680	820	1.5K	22nF
(1.5")	3	30	18	910	680	680	1.5K	18nF

Figure 3.2: A circuit diagram of the shaper boards. There were different configurations for each of the types of PMTs.

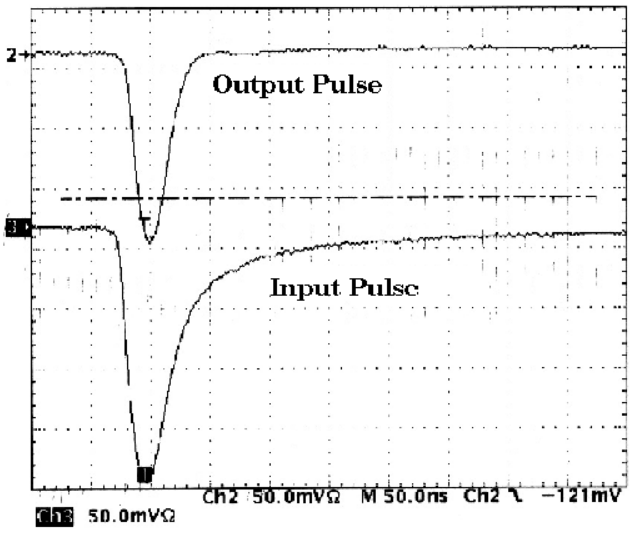

Figure 3.3: The CCAL pulse shape before and after the shaper board.

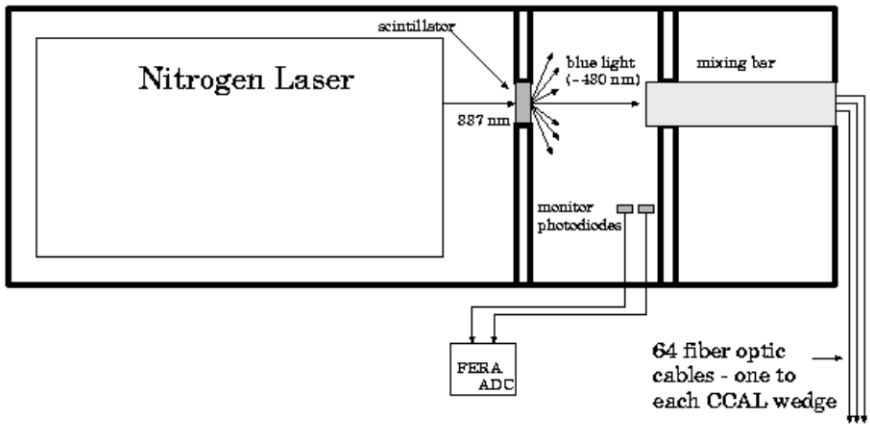

Figure 3.4: A schematic of the laser monitor.

pair of PIN diodes whose outputs were used to eliminate any fluctuations in the laser intensity.

3.2 Clusterization

Photon and electron showers in the CCAL are typically contained in more than a single block. In addition occasionally two photons hit near each other in the CCAL and their energy deposits may overlap. In order to obtain energy and position measurements of the particles, a clustering algorithm is used. The CCAL clustering algorithm is used to differentiate between three different types of clusters: isolated, shared, and split.

In the algorithm, clusterization begins by finding the highest energy block in the calorimeter. If that block has an energy higher than the *seed threshold* the 8 surrounding blocks and the central one (the seed) are flagged as forming a potential cluster. The process is repeated for the next highest block that has not

already been assigned to a 3x3 grid until there are no blocks remaining above the threshold. The energy in each of the 3x3 grids is summed and any that are above the *cluster threshold* then it is accepted as a cluster. The use of a seed and cluster threshold helps reduce background clusters that come from overlaps from previous events and noisy photomultiplier tubes.

If two clusters are near each other, there is a need to share energy in the overlapping blocks. The amount of energy assigned to each cluster depends on the calculated position which in turn depends on the energy. Thus, an iterative process is required to find the energy and position of such *shared* clusters.

It is possible that two photons deposit their energy in adjacent blocks and are thus identified as a single cluster. To take account of this, the invariant mass for each cluster that is not shared is calculated from the formula:

$$M_{cl} \equiv \sqrt{\left(\sum_i E_i\right)^2 - \left(\sum_i \overrightarrow{p}_i\right)^2} \tag{3.2}$$

where the summations are over the 5x5 grid centered on the seed block. This quantity is called the *cluster mass*. If the cluster mass is greater than 100 MeV, the cluster is identified as two clusters very close together; energy sharing is performed and the cluster is labelled as *split*. Typically, split clusters come from a π^0 that has decayed symmetrically.

The details of the position and energy calculations for each cluster type are presented in the following sections.

3.2.1 Isolated Clusters

Isolated clusters are clearly the simplest types of clusters since no energy sharing is required. The energy, before corrections for energy loss in the steel in between

the blocks, is:

$$E = \sum_{i=1}^{9} E_i \tag{3.3}$$

and the θ and ϕ of the hit are determined from a weighted average:

$$x = \frac{\sum_{i=1}^{9} E_i x_i}{\sum_{j=1}^{9} E_j} \tag{3.4}$$

$$y = \frac{\sum_{i=1}^{9} E_i y_i}{\sum_{j=1}^{9} E_j} \tag{3.5}$$

where x and y give the distance from the center of the seed block in the wedge (θ) and ring (ϕ) directions in block units.

Once the position of the hit is found, a small correction to the energy is made to account for energy deposited in the steel between the blocks. Since there are different amounts of steel in the θ and the ϕ directions a different correction must be used. Then the position of the hit is corrected for energy lost in the gap with:

$$x' = A_w \left(1 - e^{\frac{-x}{a_w}}\right) + B_w \left(1 - e^{\frac{-x}{b_w}}\right) \tag{3.6}$$

$$y' = A_r \left(1 - e^{\frac{-x}{a_r}}\right) + B_r \left(1 - e^{\frac{-x}{b_r}}\right) \tag{3.7}$$

and the corrected energy is given by:

$$E' = \frac{E_{meas}}{\left(1 - C_h e^{\frac{-|x|}{c_h}}\right)} \times \frac{1}{\left(1 - D_1 e^{\frac{-|y|}{d_1}} - D_2 e^{\frac{-|y|}{d_2}}\right)}. \tag{3.8}$$

Since the rings are not flush with one another, there are different sets of parameters for the high and low θ edges. The efficacy of the correction is demonstrated in figure 3.5. The measured energy of a photon from a π^0 decay is compared to the predicted energy as a function of its distance from the gap. A clear deficiency is seen at the gap which the energy correction algorithm is able to account for. All of the constants used for the energy correction were determined in E760 from $J/\psi \rightarrow e^+e^-$ events.

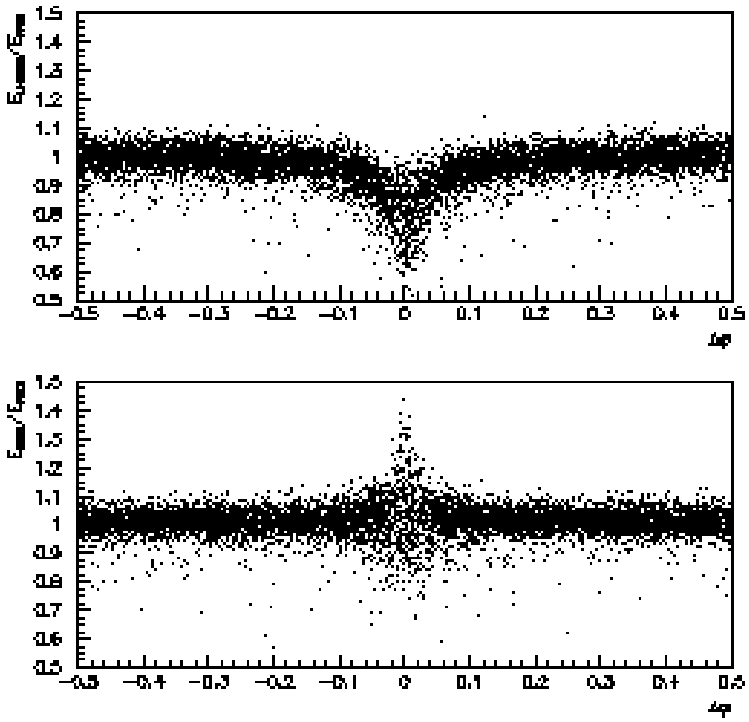

Figure 3.5: Top: The ratio of measured/expected energy of J/ψ electrons in the CCAL as a function of their distance from the gap. Bottom: The same distribution after the energy correction algorithm. The energy lost in the gap is mostly corrected for.

3.2.2 Shared Clusters

When there are two cluster centers within $\sqrt{18}$ block units[1] it is likely that the shower profiles overlap and in order to calculate the correct energies and positions of the clusters, the energy in the overlapping blocks must be correctly assigned.

The algorithm for calculating the energy and position for shared clusters is similar to that for isolated clusters. In order to account for the shared energy, an additional parameter, $f_{i,m}$, is introduced which represents the fraction of energy from cluster, m, in the overlapping block, i.

The initial energies and positions (including energy corrections) are calculated assuming that the clusters are isolated. The energy in the overlapping blocks is included in the total energy for each cluster. Then, $f_{i,m}$ is calculated for all blocks and clusters assuming an exponential lateral shower development:

$$f_{i,m} = \frac{E_m e^{-(|\delta x_{i,m}|+|\delta y_{i,m}|)/0.17}}{E_1 e^{-(|\delta x_{i,1}|+|\delta y_{i,1}|)/0.17} + E_2 e^{-(|\delta x_{i,2}|+|\delta y_{i,2}|)/0.17}} \tag{3.9}$$

where $\delta x_{i,m}$ ($\delta y_{i,m}$) is the distance from the center of the ith block to the position of the mth cluster in ring (wedge) units. E_m is the energy in the mth cluster. For blocks that are not shared, $f_{i,m}$ is 1 or 0.

The energies and positions are then recalculated using the $f_{i,m}$s using the formulae:

$$E'_m = \sum_{i=1}^{9} f_{i,m} E_i$$

$$x'_m = \frac{\sum_{i=1}^{9} f_{i,m} E_i x_i}{\sum_{j=1}^{9} f_{j,m} E_j}$$

[1]One block unit corresponds to the distance between two subsequent rings or wedges. For example, the distance between the blocks in ring 15 wedge 6 and ring 18 wedge 6 is three block units. The distance between the blocks in ring 10 wedge 54 and ring 12 wedge 51 is $\sqrt{13}$ block units.

$$y'_m = \frac{\sum_{i=1}^{9} f_{i,m} E_i y_i}{\sum_{j=1}^{9} f_{j,m} E_j}.$$

Then, the new positions are entered into the $f_{i,m}$ of equation 3.9 and the process is repeated until the energy of each cluster changes by less than 30 MeV and θ and ϕ change by less than 5 mrad.

3.2.3 Split Clusters

For π^0s that decay symmetrically, the angle between the two photons can be small enough such that there will be only one local maximum. The size of the CCAL blocks was chosen so that the two photons from a π^0 decaying completely symmetrically, where the opening angle is a miniumum, would open with an angle corresponding to approximately 1.5 blocks at the highest energy. Thus, symmetric π^0 decays give only one maxima in the CCAL but the apparent size of the deposit is larger than would be expected for a single photon. We can use the cluster mass, as described earlier, to identify these deposits as coming from two photons rather that one.

The splitting algorithm is similar to the sharing algorithm. The centers of the two clusters are chosen as the highest energy block and the highest energy block diagonally adjacent. In order to maximize the information from the tails of the shower, the energy is taken from the 5x5 grid about each cluster center. The center block of the other cluster is not included in the sum. The process described for shared clusters is performed with the exception that the cluster centers are not shared. This has the effect of slightly over-estimating the separation of the two clusters and thus overestimating the invariant mass. Since it is only π^0s that create split clusters, this discrepancy is of little importance; the fact that the clusters are split is enough to identify the π^0.

3.3 Calibration

The *in situ* energy calibration of the CCAL is performed using $\pi^0\pi^0$ events, which are produced in abundance in $\overline{p}p$ interactions. During data taking, prospective $\pi^0\pi^0$ events were written directly to disk for rapid analysis. These events were further analyzed off-line to obtain a clean $\pi^0\pi^0$ sample. Since $\pi^0\pi^0$ production satisfies two-body kinematics, the energy of the π^0s can be calculated from the angle of the reaction in the laboratory. The CCAL calibration constants can be derived using the knowledge of the π^0 energies[35].

The measured energy of the *jth* π^0 is given by:

$$M_j = \sum_{i=1}^{n} g_i A_{ij} \tag{3.10}$$

where g_i is the calibration constant of the *ith* block with A_{ij} the number of ADC counts in that block for the *jth* π^0. The sum is over all of the blocks in both clusters associated with the π^0. The energy of the π^0 can be predicted from two-body kinematics if its angle, θ, is known. The angle is calculated from the measured energy of the two photons:

$$tan\theta_{\pi^0} = \frac{\sqrt{(P_{Ax} + P_{Bx})^2 + (P_{Ay} + P_{By})^2}}{P_{Az} + P_{Bz}} \tag{3.11}$$

where $P_{A,Bk}$ is the momentum in the k direction of photons A, B. The energy of the π^0 is then:

$$E_{\pi^0} = \frac{E_{cm}(1 + A\beta cos\theta_{\pi^0})}{2\gamma(1 - \beta^2 cos^2\theta_{\pi^0})}$$

with:

$$A^2 \equiv 1 - \frac{4\gamma^2 m_\pi^2 (1 - \beta^2 cos^2\theta_{\pi^0})}{E_{cm}^2}. \tag{3.12}$$

The predicted energy is dependent on the gain constants since it is calculated from the measured photon energy.

Using the measured and predicted π^0 energies, the χ^2 is calculated:

$$\chi^2 \equiv \sum_{j=1}^{N} \frac{(M_j - E_j)^2}{\sigma_j^2} \tag{3.13}$$

where σ_j is the estimated uncertainty in the predicted energy. Minimizing χ^2 and solving for the gain constants gives:

$$g_k = \frac{\sum_{j=1}^{N} \left(\frac{A_{k,j}}{\sigma_j^2}\right) \left(E_j - \sum_{i=1, i\neq k}^{n} A_{i,j} g_i\right)}{\sum_{j=1}^{N} \frac{A_{k,j}^2}{\sigma_j^2}}. \tag{3.14}$$

For each stack, the calibration constants were calculated for every block using the above equations. There are 1280 simultaneous equations with 1280 unknowns. To avoid having to solve this system of equations, the calculation was done using an initial set of constants and then iterating until the χ^2 changed by less than 1%.

It was sometimes the case that there too few events in a block to get a reasonable calibration. For these circumstances the laser monitor was used to track the gain constants. The amplitude of the laser pulse by itself can give only a relative gain; it can be used to track changes over time of the gain constant for each block. The mean of the $\pi^0\pi^0$ gain constants over all stacks was used to set the calibration scale. If the calibration constant measured using $\pi^0\pi^0$ events was significantly different from the one given by the laser, the constant derived from the laser monitor was used.

3.4 Timing

The timing information of CCAL hits is essential for analyzing data collected at a high rate in order to differentiate the hits associated with the trigger and random

hits. Each CCAL block had a signal fed into a multi-hit TDC with 1 ns resolution. The TDC ran in common-stop mode, which means that hits with higher TDC counts came earlier. The TDC signal pulse came from the discriminator on the shaper board. The threshold on the discriminator, in ADC counts, was measured by looking at the pulse height versus the fraction of time a TDC hit is registered (figure 3.6). These curves were fit to:

$$f = 0.5 \times (erf(M \times (ADC - T)) + 1.0). \tag{3.15}$$

Here M and T are the free parameters.

Different pulse heights cross the threshold at different times relative to the start pulse. This effect is known as *slewing*. The measured time was corrected with a function (a slew curve) that was obtained by fitting the recorded time versus the number of ADC counts (figure 3.7). For each block, the slew curves were fit to:

$$TDC = T_0 + B_0 \times (1 - \frac{A_0}{ADC}) \times ln(ADC + E_0) \tag{3.16}$$

where T_0 (A_0) is the TDC (ADC) counts for at-threshold hits (obtained from data). B_0 and E_0 are free parameters. Using these parameters, the time was corrected via the equation:

$$TDC_{corr} = T_{nominal} - TDC_{raw} - T_0 + B_0 \times (1 - \frac{A_0}{ADC}) \times ln(ADC + E_0) \tag{3.17}$$

The slew corrected times give a distribution for each block around $T_{nominal}$.

If a block has a time within ± 10 ns of 1000 ns, the hit is labelled *in-time*; if it is outside this window, the hit is *out-of-time*. If there is no TDC information for a hit, the block is called *undetermined*. In addition, each cluster has associated timing information. If there is a TDC hit in the seed block, the cluster time corresponds to the seed's. If the seed block is undetermined, the cluster time is

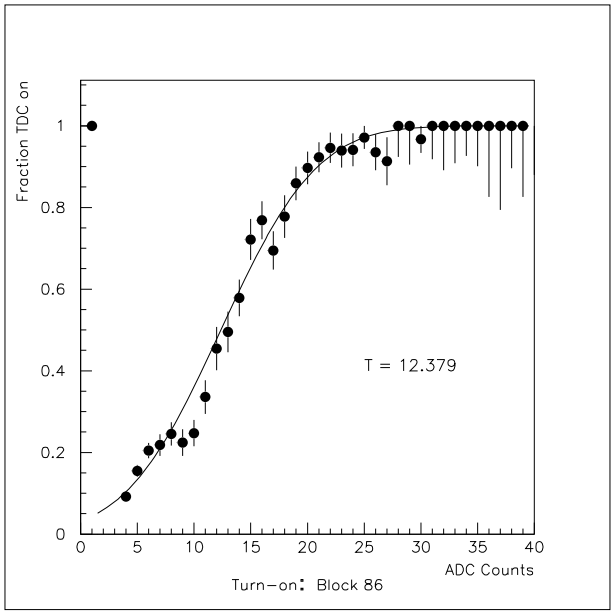

Figure 3.6: A typical TDC turn-on curve. Ignore the point at 0 ADC counts.

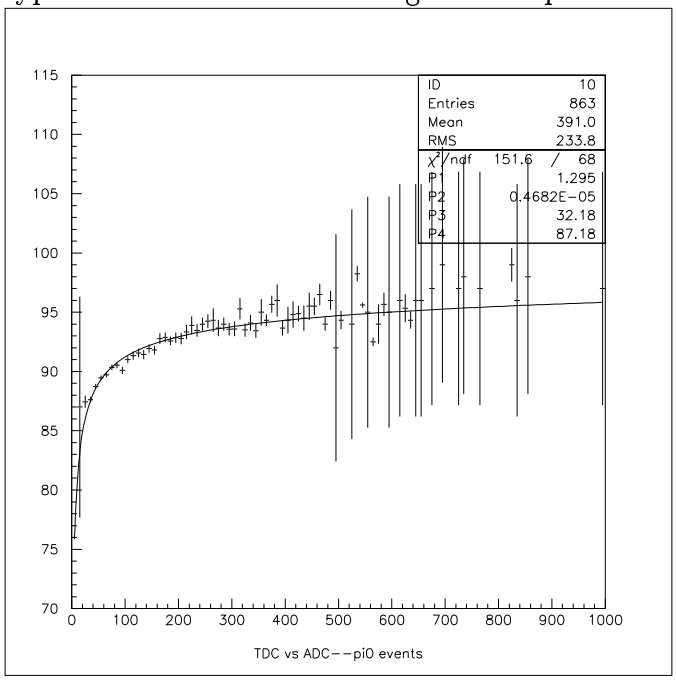

Figure 3.7: A typical slew curve. The horizontal axis is ADC counts and the vertical axis is leading edge time. The fit is described in the text.

taken as the time of the second highest energy block in the cluster. For instances where they are both below threshold, the cluster is undetermined. Nearly all clusters above $\sim$75 MeV had timing information.

Cluster timing is crucial for the $\gamma\gamma$ analysis. It allows for the rejection of a large fraction of the $\pi^0\pi^0$ and $\pi^0\gamma$ background events, since there is a high chance that these events will have an third or fourth in-time cluster.

Chapter 4

The Background Calculation

Although the detector was designed to efficiently detect electromagnetic final states in order to overcome a large hadronic background, the $\gamma\gamma$ final state still has a relatively large background. The background comes from $\overline{p}p \rightarrow \pi^0\gamma$ and $\overline{p}p \rightarrow \pi^0\pi^0$ events where one or two photons escape detection. The background from these sources, called the *feeddown* background, can be calculated if the probability of a $\pi^0\gamma$ or $\pi^0\pi^0$ to mimic a $\gamma\gamma$ event is known. The knowledge of this background will be used to extract the $\gamma\gamma$ partial width.

Generally speaking, one of the two photons from a π^0 decay can escape detection and cause the π^0 to mimic a single photon. There are two reasons why a photon will not be recognized. If the π^0 decays asymmetrically, the low energy photon may be below the detection threshold of the CCAL or go out the back of the detector. In this case one photon from the π^0 carries practically all of the energy. Also, if a high energy π^0 decays symmetrically, the two photons will hit the CCAL very close together and may be mistaken as a single photon. A simulation of the CCAL is used in order to calculate the probability that a $\pi^0\pi^0$ or

$\pi^0\gamma$ event looks like a $\gamma\gamma$ event. In this chapter the CCAL simulation and how it is used to calculate the feeddown background is described.

4.1 The $\gamma\gamma$ Feeddown and the CCAL Simulation

The $\gamma\gamma$ feeddown cross section is given by the expression:

$$\sigma_{feed} \sim \sigma_{\pi^0\pi^0} P_\gamma^2 + \sigma_{\pi^0\gamma} P_\gamma \tag{4.1}$$

The CCAL simulation (also known as the fast Monte Carlo or fMC) is used in the $\gamma\gamma$ feeddown to calculate the probability that $\pi^0\pi^0$ and $\pi^0\gamma$ events imitate $\gamma\gamma$ events (P_γ) and also to calculate detection efficiencies for $\pi^0\pi^0$, $\pi^0\gamma$, and $\gamma\gamma$ cross sections in the χ_{c0} region. The fast Monte Carlo uses photons generated by a phase space generator, extrapolates them into the CCAL, and simulates their shower response in the lead glass. The program uses 14 parameters to simulate the shower profile and energy smearing. These parameters were tuned so that the simulation and the data matched to an acceptable degree. Special attention was paid to the variables that have a direct impact on the systematic error in the feeddown cross section from the fMC.

The fast Monte Carlo simulates showers in the CCAL as a sum of two exponentials (a core and a tail) centered at the hit position in both the ring and wedge directions. The shower profiles are given as:

$$E_r(R) = 10 * exp\left(\frac{-|R - R_{hit}|}{LA_r}\right) + B_r exp\left(\frac{-|R - R_{hit}|}{LB_r}\right)$$
$$E_w(W) = 10 * exp\left(\frac{-|W - W_{hit}|}{LA_w}\right) + B_w exp\left(\frac{-|W - W_{hit}|}{LB_w}\right)$$

The first term in each expression describes the shower core while the second

term corresponds to its tail. The shower profile is normalized to the energy of the particle obtained from the generator less the energy that would be lost in the cracks. The energy lost in the cracks is calculated from the incident photon position using the CCAL crack correction algorithm. The energy from a shower is assumed to be contained in a 3×3 grid of blocks centered at the block containing the hit. The energy in each block is found by integrating the profile over the bounds of the block. Energies are converted to ADC hits and inserted into the hit arrays. From this point on, the treatment of the event is exactly the same as for the data. The tail amplitudes and the core and tail decay lengths give 6 parameters used to adjust the size and shape of the shower. Changes to these parameters result in changes in measured hit positions and cluster mass.

The energy deposited in each individual block is smeared. The energy in the center block of the 3×3 grid is smeared separately from the other eight blocks since the center block's energy is not modified by the crack correction. The energy smearing affects the widths of the distributions of the acoplanarity, akinematics, and total energy. The remaining eight parameters are used to take account of the energy fluctuations which include both the smearing for energy lost in the cracks between blocks and fluctuations of the pedestal.

The method used to tune the fMC parameters was to use collected $\overline{p}p \rightarrow \pi^0\pi^0$ events at the χ_0 and compare their event topology with events generated by the Monte Carlo for different values of the parameters[36]. Special attention was paid to the distributions to which the feeddown calculation was particularly sensitive. These were the cluster mass, akinematics, acoplanarity, π^0 mass, and π^0 asymmetry. Parameters were tuned so that these distributions generated by the fMC matched with the data as closely as possible.

When the tuning procedure was complete, the akinematics, acoplanarity, and π^0 mass distributions had excellent agreement with the same plots made with real data and the fMC. In the first run of E835, a large part of the feeddown systematic error was attributed to an underestimation of the highly asymmetric π^0s detected[37]. In this tuning, we saw no such deficit. This is probably due to the fact that the fMC for the first E835 was tuned at the η_c (2980 MeV) where as it was tuned at 3415 MeV for this analysis. The greatest disagreement between the fMC and the data is seen in the cluster mass distribution. This has a significant effect on the feeddown calculation and is discussed in a later section.

4.2 The Feeddown Calculation

The $\gamma\gamma$ feeddown is calculated for each energy point around the χ_0 from the $\pi^0\pi^0$ and $\pi^0\gamma$ cross sections. The $\pi^0\pi^0$ cross section calculation is readily measured from the data but the $\pi^0\gamma$ cross section is itself complicated by feeddown events from the $\pi^0\pi^0$ channel. Using the fMC, the probability for a $\pi^0\pi^0$ event to feeddown to a $\pi^0\gamma$ event can be calculated and subtracted. Similarly, the probabilities for $\pi^0\pi^0$ and $\pi^0\gamma$ to each mimic $\gamma\gamma$ events can be calculated with the fMC and from these two numbers and the $\pi^0\pi^0$ and $\pi^0\gamma$ cross sections, the $\gamma\gamma$ feeddown can be calculated.

4.2.1 $\pi^0\pi^0$ Cross Section

The $\pi^0\pi^0$ events are selected by requiring the event satisfy the following requirements:

- 4 in-time or undetermined (i.o.u.) clusters in the CCAL (25/50 MeV cluster

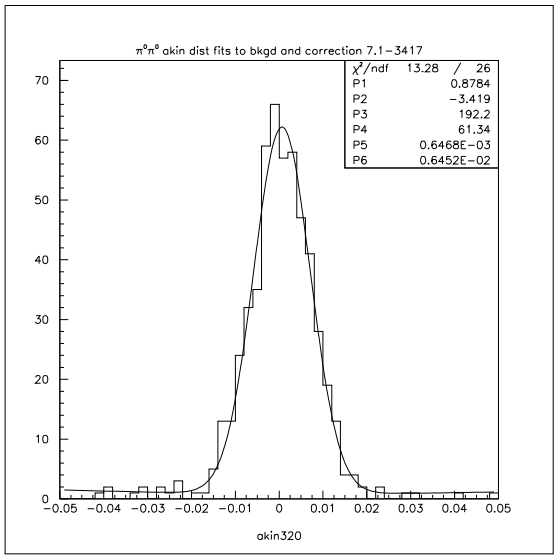

Figure 4.1: The $\pi^0\pi^0$ akinematics distribution. The small amount of background is subtracted from the signal as described in the text.

thresholds)

- Akinematics$\equiv |\theta_{1pred}(\theta_{2meas}) - \theta_{1meas}|$ <12 mrad
- Acoplanarity $\equiv ||\phi_1 - \phi_2| - \pi|$<32 mrad
- $|M_{\gamma\gamma} - 135 MeV/c^2|$ <35 MeV/c^2 or split cluster

There is a small amount of background in this data sample which comes mainly from $3\pi^0$ and $\pi^0\omega$ events[38]. The akinematics distribution is cut into slices of $\cos\theta^*$ (prior to the akinematics cut) and fit to a quadratic polynomial (background) and a Gaussian function (signal). The polynomial is then integrated in the region of the akinematics cut and the integral is subtracted from the total number of events to give the number of $\pi^0\pi^0$ events (figure 4.1).

The fast MC is used to generate $\pi^0\pi^0$ events with a flat distribution in $\cos\theta^*$. The analysis efficiency versus $\cos\theta^*$ is then calculated by dividing the number of events selected in a bin of $\cos\theta^*$ by the number of events that were generated within the same range of $\cos\theta^*$. The $\pi^0\pi^0$ cross section is given as:

$$\frac{d\sigma_{\pi\pi}}{dcos\theta^*} = \frac{N_{\pi\pi,\mathrm{bkgsub}}}{\mathcal{L}\epsilon_{\mathrm{tot}}\mathrm{a}} \tag{4.2}$$

where a is the geometric acceptance and ϵ_{tot} is given as:

$$\epsilon_{tot} = \epsilon_{trig}\epsilon_{ndst}\epsilon_{anal}(1 - P_{dalitz})^2(1 - P_{conv})^4. \tag{4.3}$$

The efficiencies are:

- ϵ_{trig} →The neutral trigger efficiency. See appendix B.
- ϵ_{ndst} →The neutral data summary tape efficiency. See appendix C.
- ϵ_{anal} →The analysis efficiency. This is derived from the fast Monte Carlo. It includes the efficiency for extra, random clusters (see appendix A on the random gate DSTs).
- 1-$P_{dalitz} = 0.988$ →The probability the π^0 decays to $e^+e^-\ \gamma$.
- 1-$P_{conv} = 0.988$ →The probability of a photon conversion to occur prior to charged veto logic[39].

It is possible for a photon generated in one bin by the MC to be reconstructed in a different bin by the clusterizer. To remedy this, the angular distribution of the cross section found with the data is fit to a 6th degree polynomial and the function is used as a weight function for the MC events. This process is iterated until the cross sections change by less than 1%. The initial weight function is taken to be flat. It usually took five iterations for the cross section to stabilize.

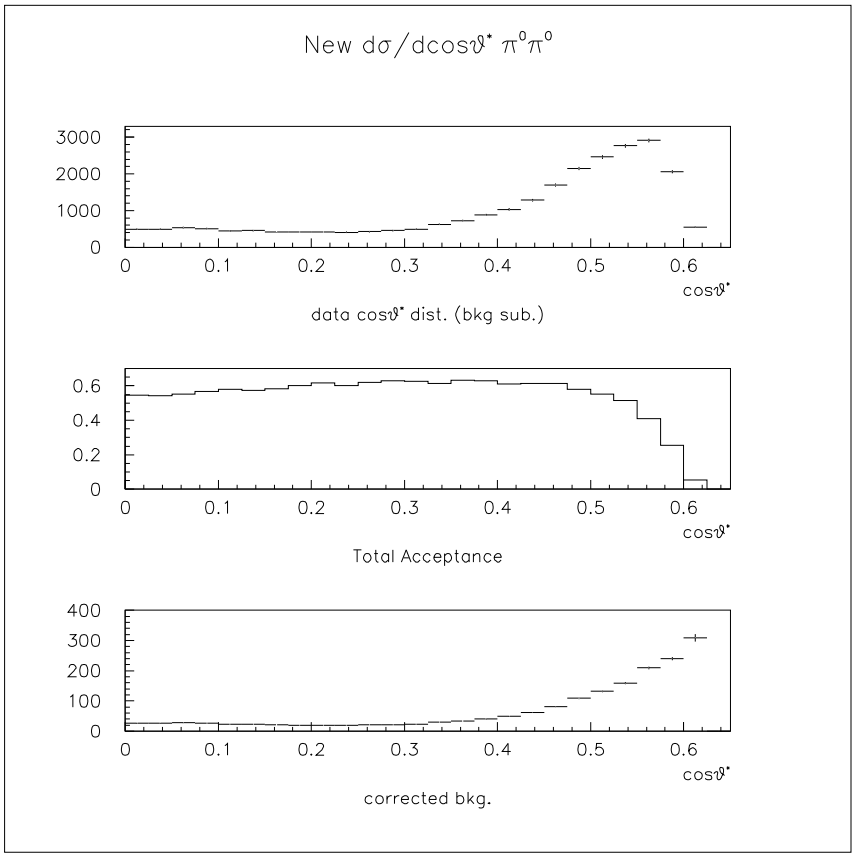

Figure 4.2: The angular distributions of $\pi^0\pi^0$ data events (top), detection efficiency (middle), and cross section for a sample χ_0 stack.

Figure 4.2 shows the $\pi^0\pi^0$ differential cross section as a function of $\cos\theta^*$. The cross section distribution is highly forward peaked. This suggests that the feeddown background to $\gamma\gamma$ will also be forward peaked. Figure 4.3 displays the integral of the $\pi^0\pi^0$ cross section up to different values of $\cos\theta^*$. The decay of χ_0 to $\pi^0\pi^0$ can be observed at a center-of-mass energy of $\sim$ 3415 MeV.

4.2.2 $\pi^0\gamma$ Cross Section

$\pi^0\gamma$ candidates are selected from events satisfying:

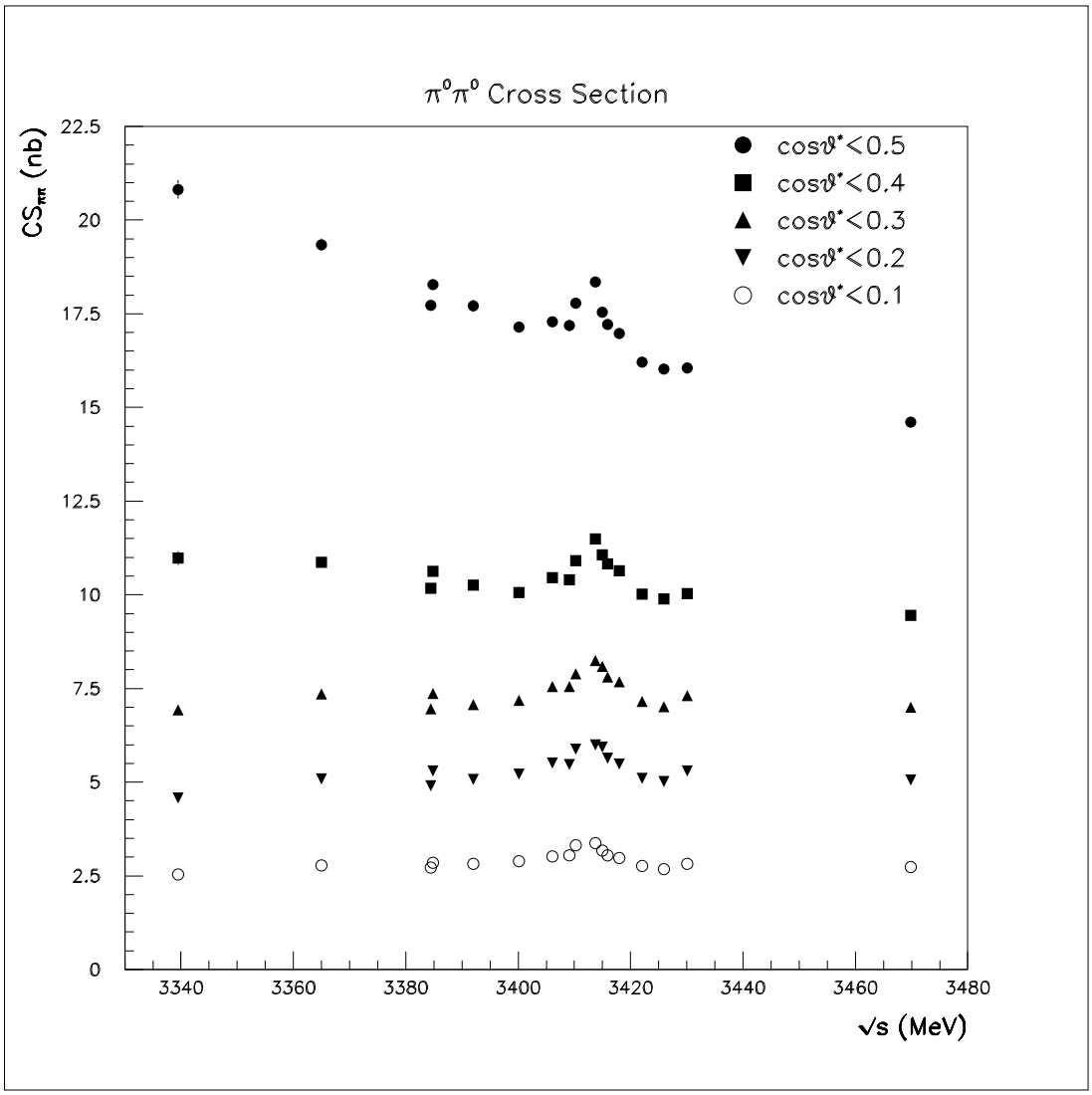

Figure 4.3: The $\pi^0\pi^0$ cross section for different $\cos\theta^*$ cuts plotted versus energy in the χ_0 region. The resonant $\chi_0 \rightarrow \pi^0\pi^0$ can be observed near 3415 MeV.

- 3 i.o.u. clusters in the CCAL (25/50 MeV cluster thresholds)
- Confidence Level($\overline{p}p \rightarrow \pi^0\gamma \rightarrow 3\gamma$) >0.1–5C fit
- $|M_{\gamma\gamma} - 135 MeV/c^2|$ <35 MeV/c^2 or split cluster

The fMC is used to obtain the probability that a $\pi^0\pi^0$ event mimics a $\pi^0\gamma$ event. This probability is about 0.045 at the χ_0 (3415 MeV/c^2) for 25/50 MeV cluster thresholds. Once found, this probability is then multiplied bin by bin in $\cos\theta^*$ by the $\pi^0\pi^0$ cross section. The resulting distribution is then subtracted from the measured $\pi^0\gamma$ cross section to obtain the feeddown subtracted $\pi^0\gamma$ cross section. Figure 4.5 shows the $\pi^0\gamma$ cross section before and after the $\pi^0\pi^0$ feeddown subtraction. This procedure is described symbolically by:

$$\sigma_{\pi^0\gamma} \sim \frac{1}{\mathcal{L} \times \epsilon_{\text{trig}} \times \epsilon_{\text{anal}}} [N_{tot} - \sigma_{\pi^0\pi^0} \times P_{\pi^0\pi^0 \rightarrow \pi^0\gamma} \times \epsilon_{trig} \times \mathcal{L}] \tag{4.4}$$

One test of the efficacy of the feeddown method is the $\pi^0\gamma$ asymmetry. By charge invariance, the $\pi^0\gamma$ cross section should be symmetric about $\cos\theta^*$=0. Clearly, prior to the feeddown subtraction (lower left figure 4.4), the data is much higher in the positive $\cos\theta^*$ region than in the negative region[1]. The feeddown restores much of the symmetry. Figure 4.6 shows the $\pi^0\gamma$ asymmetry, as defined as:

$$A_{\pi^0\gamma} = \frac{\sigma_{\pi^0\gamma}(cos\theta^* = 0 \rightarrow 0.4) - \sigma_{\pi^0\gamma}(cos\theta^* = -0.4 \rightarrow 0)}{\sigma_{\pi^0\gamma}(cos\theta^* = -0.4 \rightarrow 0.4)}$$

for all of the stacks in the χ_0 region as a function of $\cos\theta^*$. Averaging over all of the points yields a slight negative asymmetry, which suggests a small overcorrection by the feeddown.

[1]The angle is measured from the π^0.

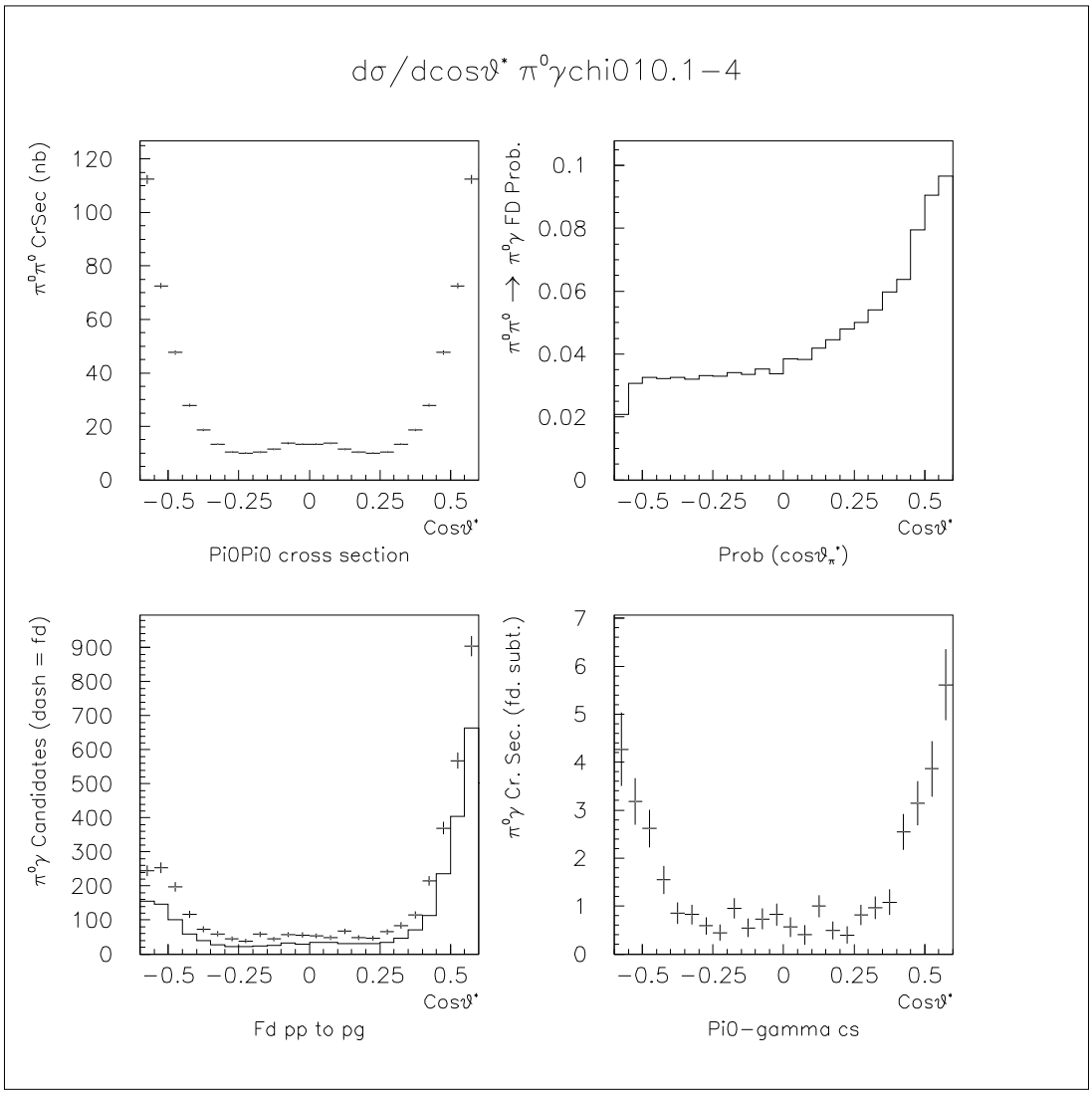

Figure 4.4: Top left: the $\pi^0\pi^0$ differential cross section. Top right: the $\pi^0\pi^0 \rightarrow \pi^0\gamma$ feeddown probability. Bottom left: the $\pi^0\gamma$ candidate events (error bars) and the calculated number of feeddown events from $\pi^0\pi^0$. Bottom right: feeddown subtracted $\pi^0\gamma$ differential cross section.

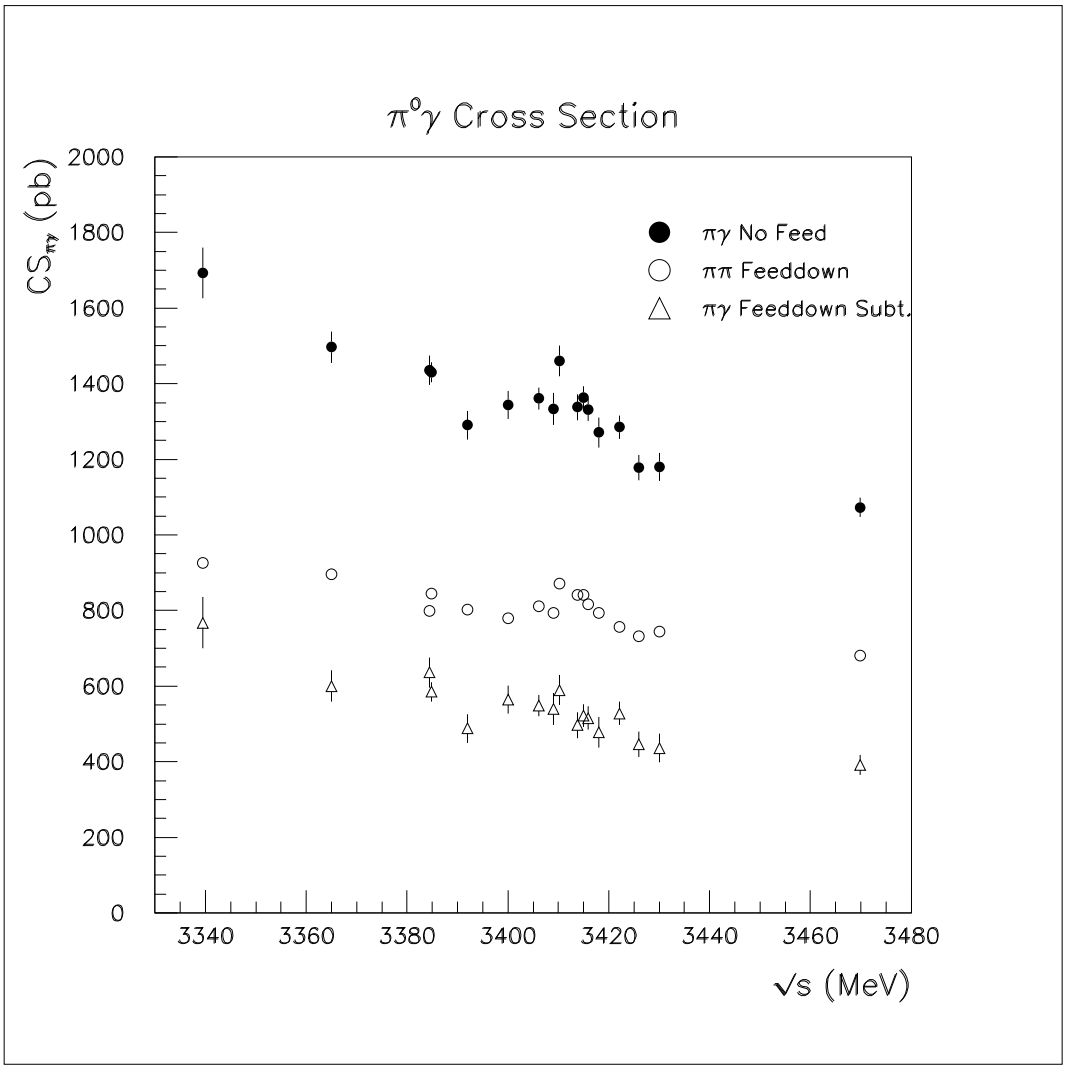

Figure 4.5: The $\pi^0\gamma$ candidate cross section (black circles), $\pi^0\pi^0 \rightarrow \pi^0\gamma$ feeddown cross section (open circles), and feeddown subtracted $\pi^0\gamma$ cross section (triangles).

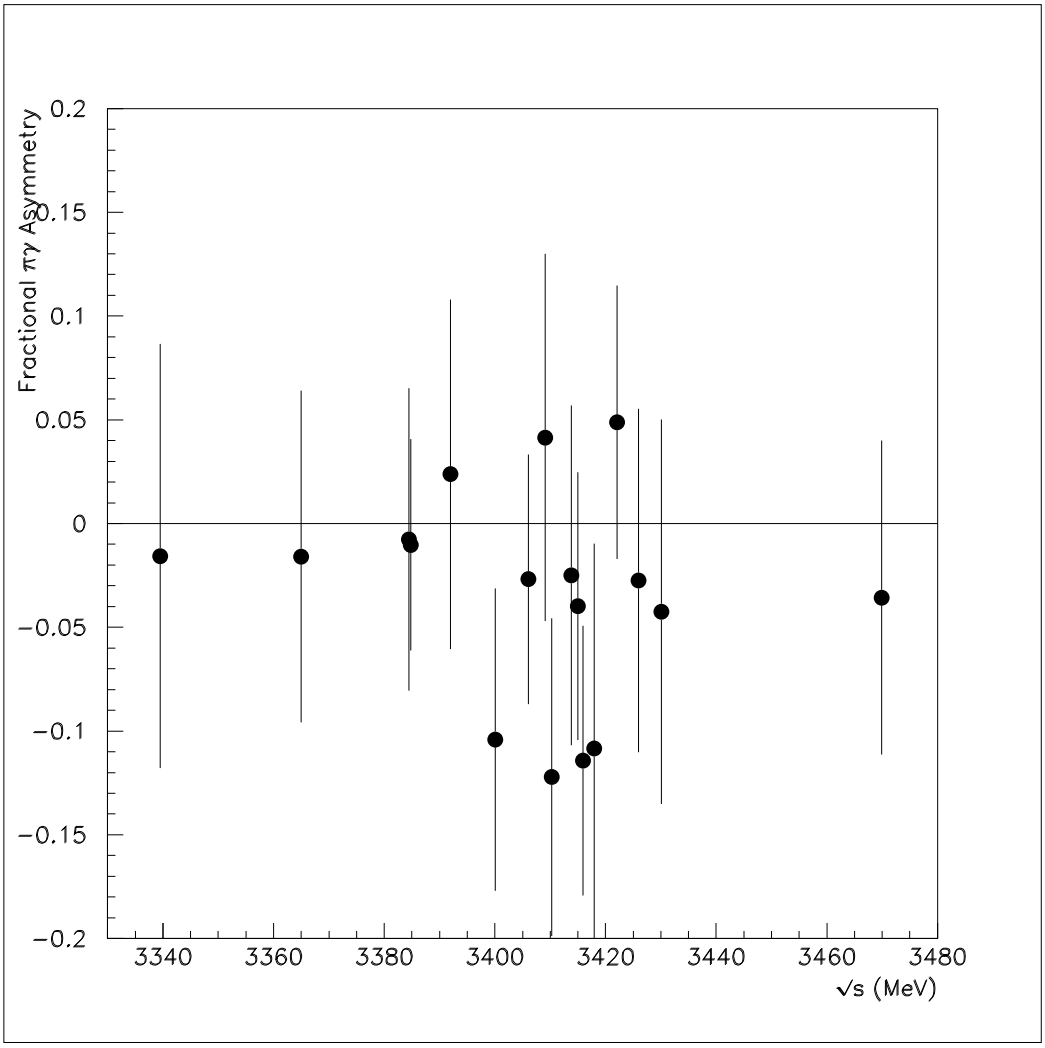

Figure 4.6: The $\pi^0\gamma$ asymmetry. Negative asymmetry means the measured cross section is higher in the backward region.

4.2.3 $\gamma\gamma$ Feeddown

The feeddown to two photons is calculated by generating $\pi^0\pi^0$ and $\pi^0\gamma$ events and calculating the probability that these events mimic a $\gamma\gamma$ event. The events are selected with the following criteria:

- Satisfies a 4C fit with CL($\overline{p}p \rightarrow \gamma\gamma$)>0.1.
- Two in-time CCAL clusters and any number of out-of-time or undetermined clusters.
- $|\mathrm{M}_{\gamma-extracluster}\text{-}\mathrm{M}_{\pi^0}| < 35\ MeV/c^2$.
- $\mathrm{M}_{cluster} < 100\ MeV/c^2$.

Chapter 5 will have a detailed discussion of these cuts.

The calculation of the $\gamma\gamma$ feeddown proceeds in a way similar to the $\pi^0\gamma$ feeddown calculation. The fMC is used to calculate the probabilities $P_{\pi\pi\rightarrow\gamma\gamma}$ and $P_{\pi\gamma\rightarrow\gamma\gamma}$. The variations of these probabilities with $\cos\theta^*$ is shown in the middle row or figure 4.7. These probabilities are then used to estimate based on the appropriate cross sections and luminosity bin-by-bin, the number of feeddown events . Figure 4.8 shows the individual feeddown rates with $\cos\theta^* \leq 0.4$. The $\chi_0 \rightarrow \pi^0\pi^0$ resonance contribution can be clearly seen in the $\pi^0\pi^0$ feeddown contribution.

4.2.4 Feeddown Correction

In spite of the fact that the fast Monte Carlo has been tuned, there remain some small discrepancies between the fMC event distribution and the data. The most important of these is the difference between the data and the Monte Carlo for

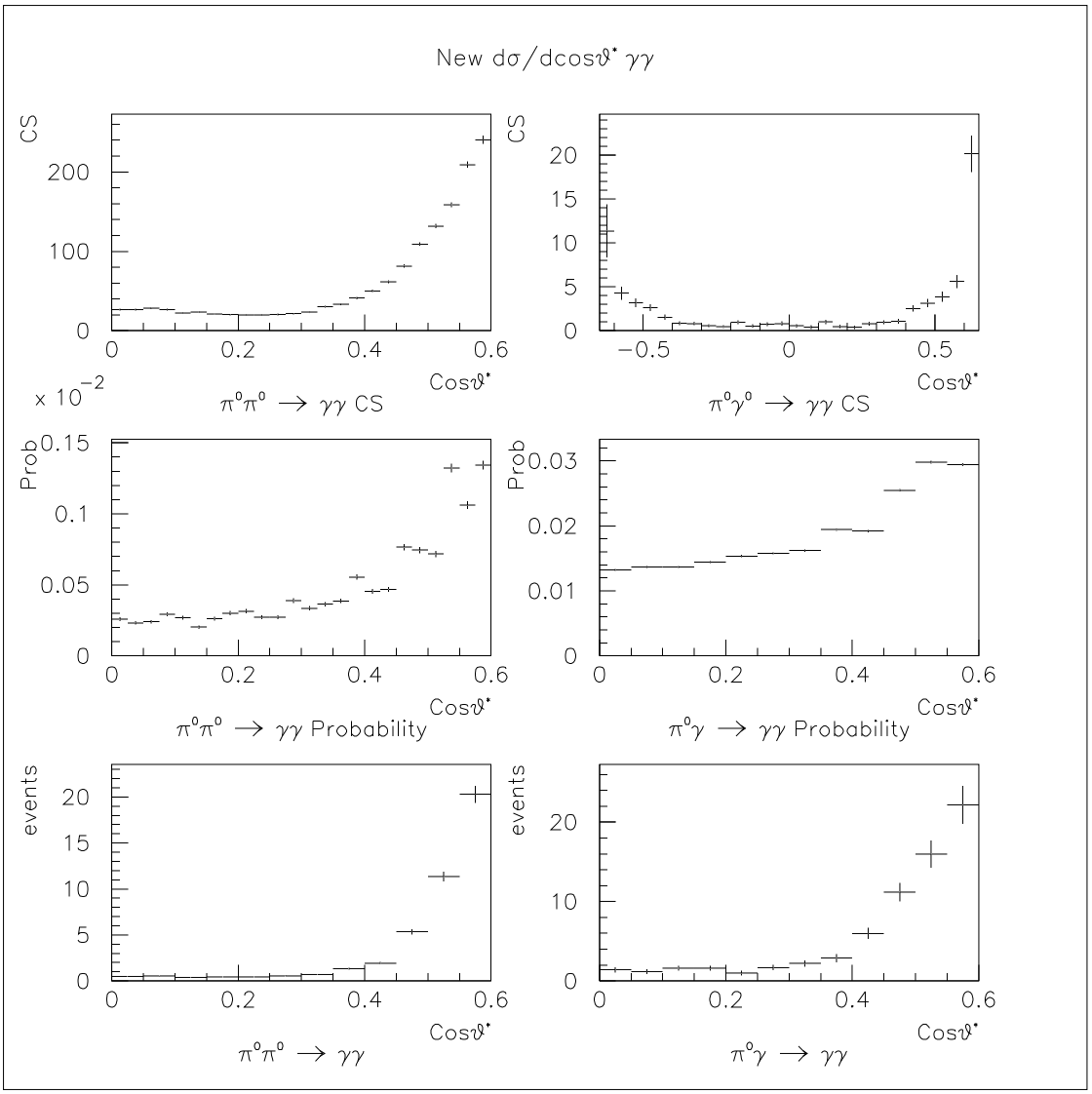

Figure 4.7: The $\gamma\gamma$ feeddown calculation for a sample stack. Top: the $\pi^0\pi^0$ and $\pi^0\gamma$ differential cross sections. Middle: the $\gamma\gamma$ feeddown probabilities. Bottom: the calculated number of feeddown events.

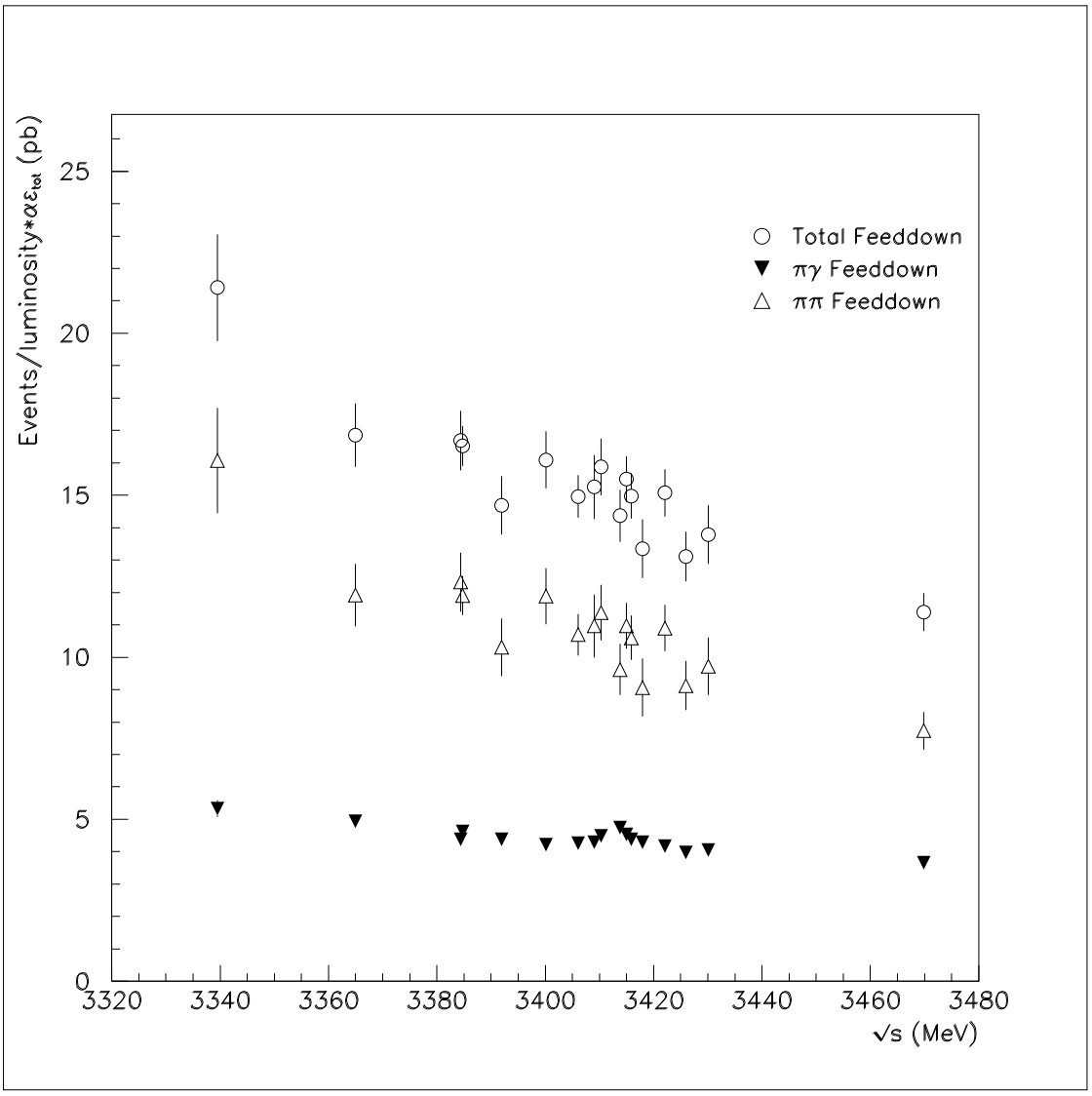

Figure 4.8: The $\pi^0\pi^0$ (black triangles), $\pi^0\gamma$ (open triangles), and total $\gamma\gamma$ feed-down cross sections for $\cos\theta^* \leq 0.4$.

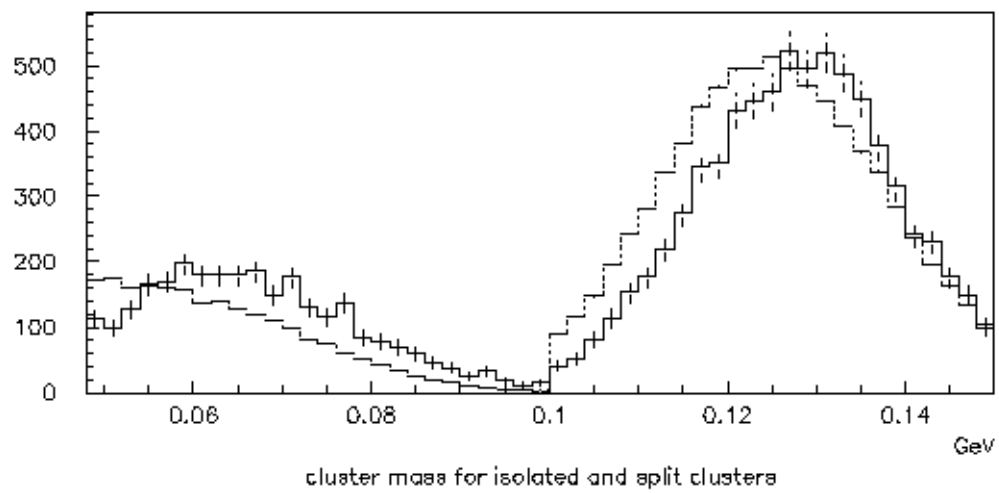

Figure 4.9: The cluster mass distribution for split and isolated π^0 clusters. The solid histogram is data; the dashed is from the fast Monte Carlo.

the cluster mass of split clusters (symmetric π^0s). Figure 4.9 shows the cluster mass distributions for isolated and split (>100 MeV) clusters. The fMC generated distribution peaks at lower cluster mass than the data for split clusters resulting in overestimation in the number of undetected symmetric π^0s. Since symmetric π^0s with a cluster mass below 100 MeV are identified as single high energy photons, this results in an overestimation of the feeddown.

This overestimation can be quantified and corrected for. The fraction of misidentified symmetric π^0s (henceforth known as MS π^0s) in the data and the fMC can be estimated by fitting the split cluster peak to a Gaussian function and integrating from -∞ to 100 MeV. These fractions are to be 0.01$\pm$0.002 for the fMC and 0.005$\pm$0.002 for the data.

Using equation 4.1 to calculate the shift in the feeddown cross section gives:

$$\begin{aligned}\Delta\sigma_{FD} = \sigma_{FD,MC} - \sigma_{FD,data} &= (P_\gamma + \Delta P_\gamma) \times [(\sigma_{\pi\pi} + \Delta\sigma_{\pi\pi}) \\ &\quad - P_\gamma(\sigma_{\pi\pi}P_\gamma + \sigma_{\pi\gamma}) + (\sigma_{\pi\gamma} + \Delta\sigma_{\pi\gamma})] \quad (4.5)\end{aligned}$$

where $\sigma_{FD,MC}$ signifies the feeddown cross section calculated by the fMC and $\sigma_{FD,data}$ the real feeddown cross section in the data.

The MS π^0s do not affect the $\pi^0\pi^0$ cross section so $\Delta\sigma_{\pi\pi} = 0$. They do however affect the $\pi^0\gamma$ cross section, since there is a feeddown contribution from $\pi^0\pi^0$ events. Simplifying equation 4.5 to first order in Δ gives:

$$\Delta\sigma_{FD} = 2\Delta P_\gamma \sigma_{\pi\pi} P_\gamma + \Delta P_\gamma \sigma_{\pi\gamma} + \Delta\sigma_{\pi\gamma} P_\gamma. \tag{4.6}$$

Since the effect will be the same for the $\pi^0\gamma$ cross section, the shift is:

$$\frac{\Delta\sigma_{\pi\gamma}}{\sigma_{\pi\gamma}} = -\frac{\Delta P_\gamma}{P_{\pi\gamma}} \tag{4.7}$$

where $P_{\pi\gamma}$ is the probability for $\pi^0\pi^0$ to feeddown to $\pi^0\gamma$. The term is negative because it decreases the $\pi^0\gamma$ cross section.

Using the fact that $P_\gamma\sigma_{\pi\gamma} \sim \frac{2}{3}\sigma_{FD}$ and $P_\gamma^2\sigma_{\pi\pi} \sim \frac{1}{3}\sigma_{FD}$ gives:

$$F \equiv \frac{\Delta\sigma_{FD}}{\sigma_{FD}} = \left(\frac{4}{3}\frac{1}{P_\gamma} - \frac{2}{3}\frac{1}{P_{\pi\gamma}}\right)\Delta P_\gamma(\sqrt{s}). \tag{4.8}$$

The only part left is to determine ΔP_γ. P_γ can be written as:

$$P_\gamma \sim P_{below\ thresh} + P_{out\ of\ accept} + f_{mis-id} \times f_{coalesced}. \tag{4.9}$$

The fMC does an excellent job of estimating the probabilities that a π^0 photon is below threshold or out of the acceptance. The third term is the one of interest. It includes the MS π^0 probability multiplied by the fraction of coalesced π^0s, which has a linear energy dependence (figure 4.10). The fMC also overestimates the fraction of coalesced π^0s so this too must be included in the correction. The overestimate of the fraction of coalesced π^0s is not energy dependent.

The knowledge of $f_{coalesced}$ and f_{mis-id} gives:

$$\Delta P_\gamma(\sqrt{s}) \sim \Delta f_{mis-id} \times f_{coalesced}(\sqrt{s}) + f_{mis-id} \times \Delta f_{coalesced} \tag{4.10}$$

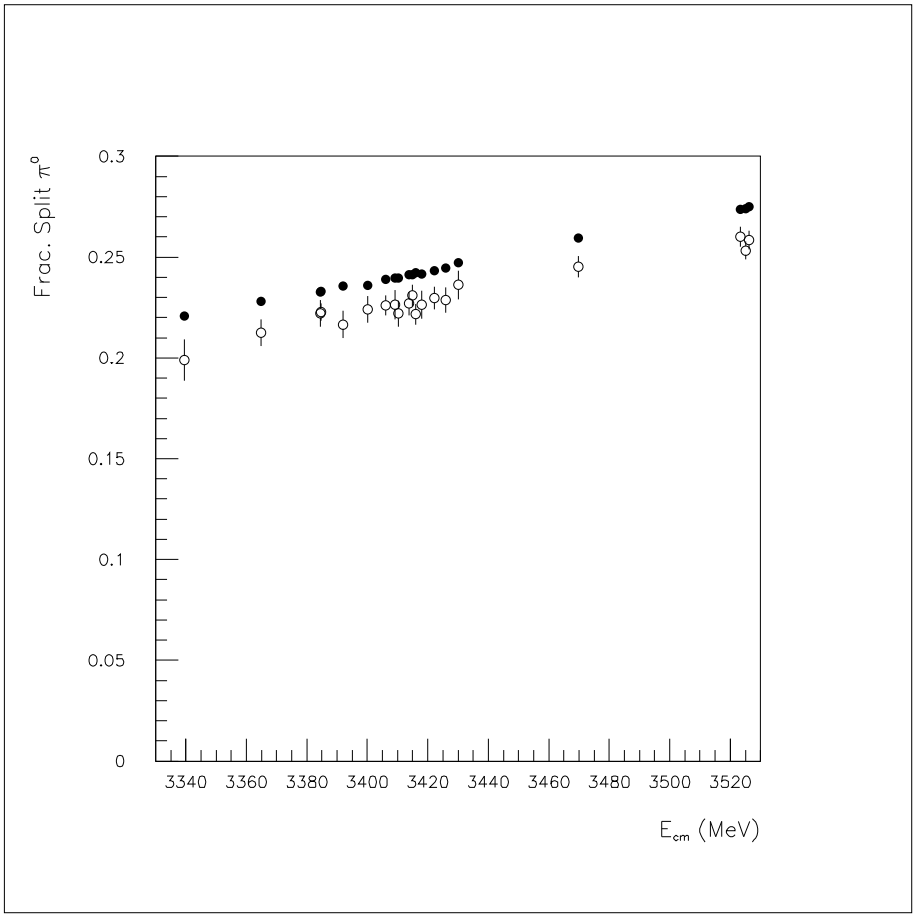

Figure 4.10: The fraction of split π^0s in $\pi^0\pi^0$ and $\pi^0\gamma$ events for data (open circles) and fast Monte Carlo (solid circles).

P_γ	0.0175
$P_{\pi^0\pi^0\to\pi^0\gamma} \equiv P_{\pi^0\gamma}$	0.045
$f_{misid,fMC}$	0.01
f_{spl}	0.235+4.4x$10^{-4}\times$(3415.0-$\sqrt{s}$)
Δf_{misid}	0.005
Δf_{spl}	0.015

Table 4.1: The inputs to the feeddown systematic error calculation.

Finally, the feeddown correction can be calculated. Using all of the variables given in table 4.1, an approximately 8% reduction in the feeddown at 3415 MeV is calculated. Over the range of data taken for the χ_0, the correction goes from $\sim$7% to $\sim$9%.

4.2.5 Feeddown Systematic Error

Using the fast MC to calculate efficiencies and feeddown probabilities will introduce a systematic error into the feeddown cross section. There are three sources of systematic error in the feeddown. The first two come from the errors in the $\pi^0\pi^0$ and $\pi^0\gamma$ cross sections due to the fMC efficiency calculation. These errors are estimated by varying the cuts by $\pm$10% and noting how the cross sections change. Tables 4.2 and 4.3 summarize the results. The error in the $\pi^0\pi^0$ cross section is less that 1% while the error in the $\pi^0\gamma$ is estimated to be $\sim$2.5%, mainly stemming from the confidence level cut.

The third source of systematic error comes from the feeddown correction, described in the previous section. The uncertainty in f_{misid} dominates the error in the correction. From equation 4.8:

$$\sigma_F = \left(\frac{4}{3}\frac{1}{P_\gamma} - \frac{2}{3}\frac{1}{P_{\pi\gamma}}\right)\sigma_{\Delta P_\gamma} \tag{4.11}$$

and

$$\sigma_{\Delta P_\gamma} = \sqrt{(f_{spl}\sigma_{\Delta f_{misid}})^2 + (\Delta f_{spl}\sigma_{f_{misid}})^2}. \tag{4.12}$$

Since $\Delta f_{spl} \ll f_{spl}$ the second term is ignored. The uncertainties in f_{misid}, give $\sigma_{\Delta f_{misid}}$=0.0028 and σ_F=0.043.

The total feeddown systematic error is then given by:

$$\left(\frac{\Delta\sigma_{feed}}{\sigma_{feed}}\right)^2 \sim \left(\frac{1}{3}\frac{\Delta\sigma_{\pi^0\pi^0}}{\sigma_{\pi^0\pi^0}}\right)^2 + \left(\frac{2}{3}\frac{\Delta\sigma_{\pi^0\gamma}}{\sigma_{\pi^0\gamma}}\right)^2 + \left(\frac{\Delta_F}{1-F}\right)^2 \tag{4.13}$$

Here Δ is used instead of σ to signify the error so as to set it apart from the cross section. For simplicity, the energy dependence of F is ignored and F is taken to be 0.08. Inserting the appropriate values into equation 4.13, the total feeddown systematic error is 5%.

Systematic Error for $2\pi^0$ Cross-section				
	CS($\cos\theta^*$ <0.4)(nb)	Ratio	CS(all $\cos\theta^*$)(nb)	Ratio
Akinematics				
10 mrad	419.4	1.004	1482.1	0.997
12 mrad	417.9	1.0	1486.8	1.0
14 mrad	416.3	0.996	1482.1	0.997
Acoplanarity				
27 mrad	412.6	0.987	1480.8	0.996
32 mrad	417.9	1.0	1486.8	1.0
37 mrad	417.3	0.999	1473.9	0.991
π^0 **mass**				
$\pm$ 30 MeV	416.6	0.997	1483.8	0.998
$\pm$ 35 MeV	417.9	1.0	1486.8	1.0
$\pm$ 40 MeV	418.9	1.002	1478.6	0.994

Table 4.2: The $\pi^0\pi^0$ cross section for different cuts. The systematic error is estimated to be $< 1\%$.

Systematic Error for $\pi^0\gamma$ Cross-section		
	CS(all $\cos\theta^*$)(nb)	Ratio
Confidence Level		
0.08	31.4	1.019
0.10	30.8	1.0
0.12	29.9	0.971
π^0 **mass**		
$\pm$ 30 MeV	31.2	1.013
$\pm$ 35 MeV	30.8	1.0
$\pm$ 40 MeV	30.6	0.994

Table 4.3: The $\pi^0\gamma$ cross section for different cuts. I estimate the systematic error is estimated to be 2.5%, mainly from the CL cut.

Chapter 5

$\gamma\gamma$ Analysis

In this chapter the details of the two photon analysis are described. This same analysis is applied to events generated by the fast Monte Carlo to determine the remaining background from $\pi^0\pi^0$ and $\pi^0\gamma$ events. The feeddown and data will be examined for off-resonance points and at high $\cos\theta^*$ in order to estimate how accurately the feeddown describes the background.

5.1 $\gamma\gamma$ Cuts

As discussed in the previous chapter, most of the $\gamma\gamma$ background comes from $\pi^0\pi^0$ or $\pi^0\gamma$ events where the low energy photons are not detected or the π^0 has coalesced to a point to where it is no longer distinguishable from a single high energy photon. These background sources are unavoidable and always contaminate the final $\gamma\gamma$ sample. The goal of making cuts is to eliminate as many of the $\pi^0\pi^0$ and $\pi^0\gamma$ events as possible, while maintaining a reasonable $\gamma\gamma$ detection efficiency.

Starting with the neutral events which have two clusters with an invariant mass of at least 2.6 GeV, the cuts imposed are:

- Satisfies a 4 constraint fit with confidence level($\overline{p}p \rightarrow \gamma\gamma$)>0.1 (figure 5.1)
- 2 in-time CCAL clusters; any number of out-of-time or undetermined clusters
- $|\mathrm{M}_{\gamma-extracluster} - M_{\pi^0}|$ <35 MeV/c^2
- $\mathrm{M}_{cluster}$ <100 MeV/c^2

The confidence level cut selects events that are consistent with two body decays and leaves mainly $\pi^0\gamma$ and $\pi^0\pi^0$ events where the π^0(s) decay somewhat asymmetrically. Recalling that we have timing information for clusters above about 75 MeV, a cut requiring there be only two in-time CCAL clusters rejects most of the remaining events. A few of the remaining background π^0's can be rejected by calculating the invariant mass between each extra cluster and the "gamma" and rejecting events which have a mass close to that of the π^0 (figure 5.2).

A small but significant portion of the background comes from π^0's when the two clusters have coalesced and the cluster is misidentified as a photon. As described in chapter 3, coalesced π^0's are identified by the splitting algorithm in the clusterizer. The splitting fails in two instances: the calculated cluster mass is less than 100 MeV or there is a small energy deposit near the π^0 which gets shared with the π^0 deposit. For π^0's with a cluster mass less than the split threshold, there is nothing that can be done short of reducing the split-cluster threshold. However, lowering the threshold increases the systematic error of the feeddown calculation.

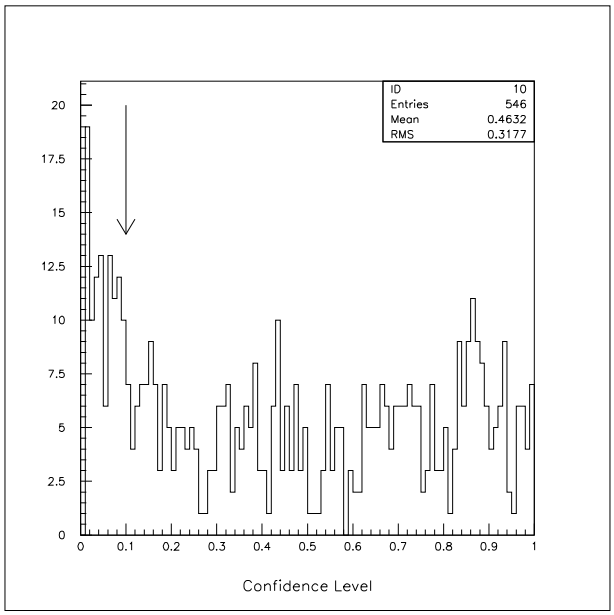

Figure 5.1: The confidence level for $\gamma\gamma$ candidates after all other cuts are implemented. The arrow shows the cut at 0.1.

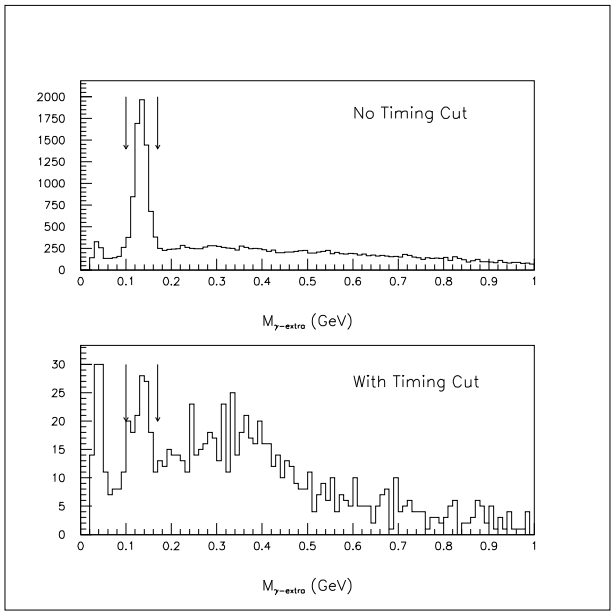

Figure 5.2: The invariant mass between the photon candidates and extra clusters in the event before and after the requirement on two in-time clusters. The arrows denote the π^0mass region.

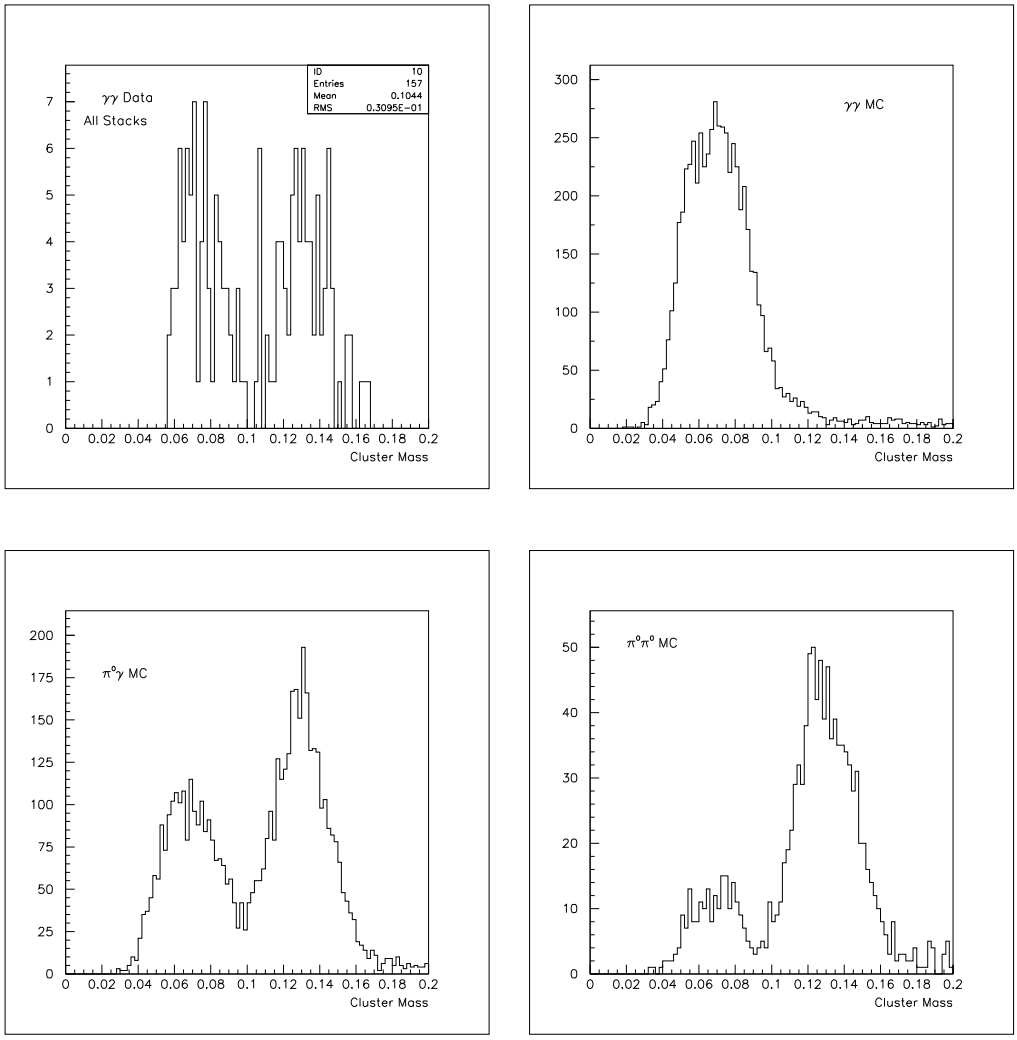

Figure 5.3: The cluster mass distributions for shared photon candidates. Clockwise from top left: photon candidates from data, $\gamma\gamma$ Monte Carlo, $\pi^0\gamma \rightarrow \gamma\gamma$ Monte Carlo, $\pi^0\pi^0 \rightarrow \gamma\gamma$ Monte Carlo. The peak at high cluster mass in the $\pi^0\pi^0$ and $\pi^0\gamma$ come from coalesced π^0s which have a random gate nearby.

A second way that a coalesced π^0 can be misidentified is that in the clusterizer algorithm the first step is to look for two local maxima within $\sqrt{18}$ CCAL blocks. If there is a small deposit (above the cluster threshold) near a coalesced π^0, say from a pileup event, the deposits will be labelled two shared clusters instead of two split clusters shared with a third, low energy cluster. One of the resulting shared clusters will correspond to the energy of the π^0, while the other will have the energy of the low energy cluster. Thus, the π^0 will mimic a shared high energy photon. However, one can use the cluster mass to identify these events; these "shared gammas" which are truly π^0s, will have a large cluster mass. Consistent with the split cluster threshold, a cluster mass cut of 100 MeV/c^2 is used on shared gammas. Figure 5.3 shows the cluster mass distributions for shared clusters for data and the three Monte Carlos. These plots show that the cluster mass cut rejects significant background without a large loss of efficiency.

Finally, a cut on the angle of the decay is made. Both the $\pi^0\pi^0$ and $\pi^0\gamma$ cross sections are forward peaked while the probability to mimic a $\gamma\gamma$ event is fairly uniform. Therefore, the $\gamma\gamma$ background will be forward peaked. Noting that the $\chi_0 \rightarrow \gamma\gamma$ decay is uniform in $\cos\theta^*$, a cut on the angle is implemented to optimize the signal-to-noise ratio(figure 5.4). The cut was chosen to be $\cos\cos\theta^* < 0.4$. The possibility of a significant $\gamma\gamma$ continuum complicates the issue as there may be interference between the continuum and resonance signals. This will be discussed further in the following sections.

5.1.1 $\gamma\gamma$ Efficiencies

The analysis efficiency for the $\gamma\gamma$ analysis is calculated using the fast Monte Carlo, with each event being overlaid with a random gate event. Overall, the

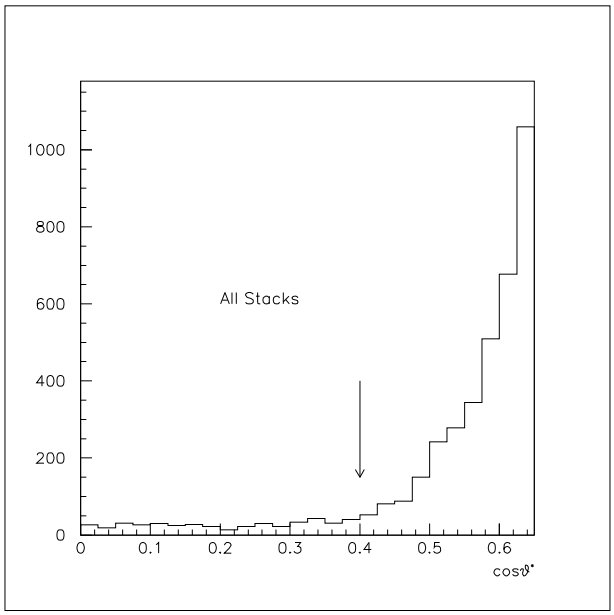

Figure 5.4: The angular distribution of $\gamma\gamma$ candidate events.

total efficiency is:

$$\epsilon_{\gamma\gamma} = \epsilon_{trig}\epsilon_{det}(1 - P_{conv})^2$$

where ϵ_{trig} is the neutral trigger efficiency, ϵ_{det} is the analysis efficiency calculated by the Monte Carlo, and P_{conv} is the photon conversion probability. It should be noted that the $\gamma\gamma$ analysis is performed on all events collected so that compression efficiencies of the subsequent data reduction are not relevant. Figure 5.5 shows the total efficiency for each stack as a function of energy and instantaneous luminosity. The change in efficiency due to the rate of pile-up events is clear in the plot of efficiency versus instantaneous luminosity (top). From the lower plot it is evident that the energy dependence is minimal.

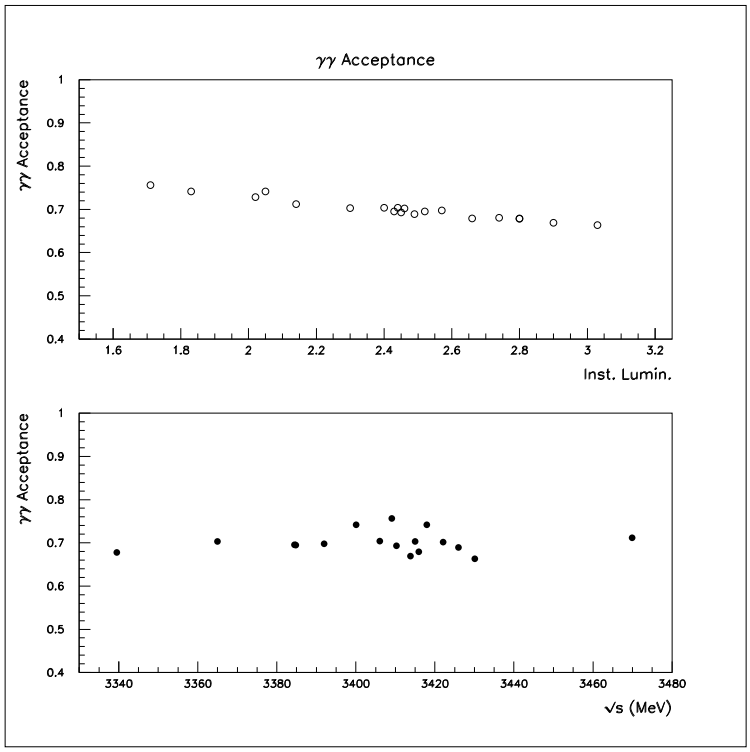

Figure 5.5: Top: $\gamma\gamma$ efficiency verses instantaneous luminosity. Bottom: $\gamma\gamma$ efficiency verses energy.

5.2 $\gamma\gamma$ Data and Feeddown

Applying the cuts described earlier to both the data and feeddown Monte Carlo events ($\pi^0\pi^0$ ($\gamma\gamma$) and $\pi^0\gamma$ ($\gamma\gamma$)), a total of 4301 data events pass the cuts, and 440 of these have $\cos\theta^*$ less than 0.4, in the 17 stacks around the χ_0. Table 5.1 summarizes the results.

Figure 5.6 shows the angular distribution of events in six different energy regions. These regions are:

1. Low Background: 3340-3391 MeV–Integrated Luminosity=$\mathcal{L}$=8.5 pb^{-1}

2. Low Resonance: 3406-3413 MeV–$\mathcal{L}$=8.3 pb^{-1}

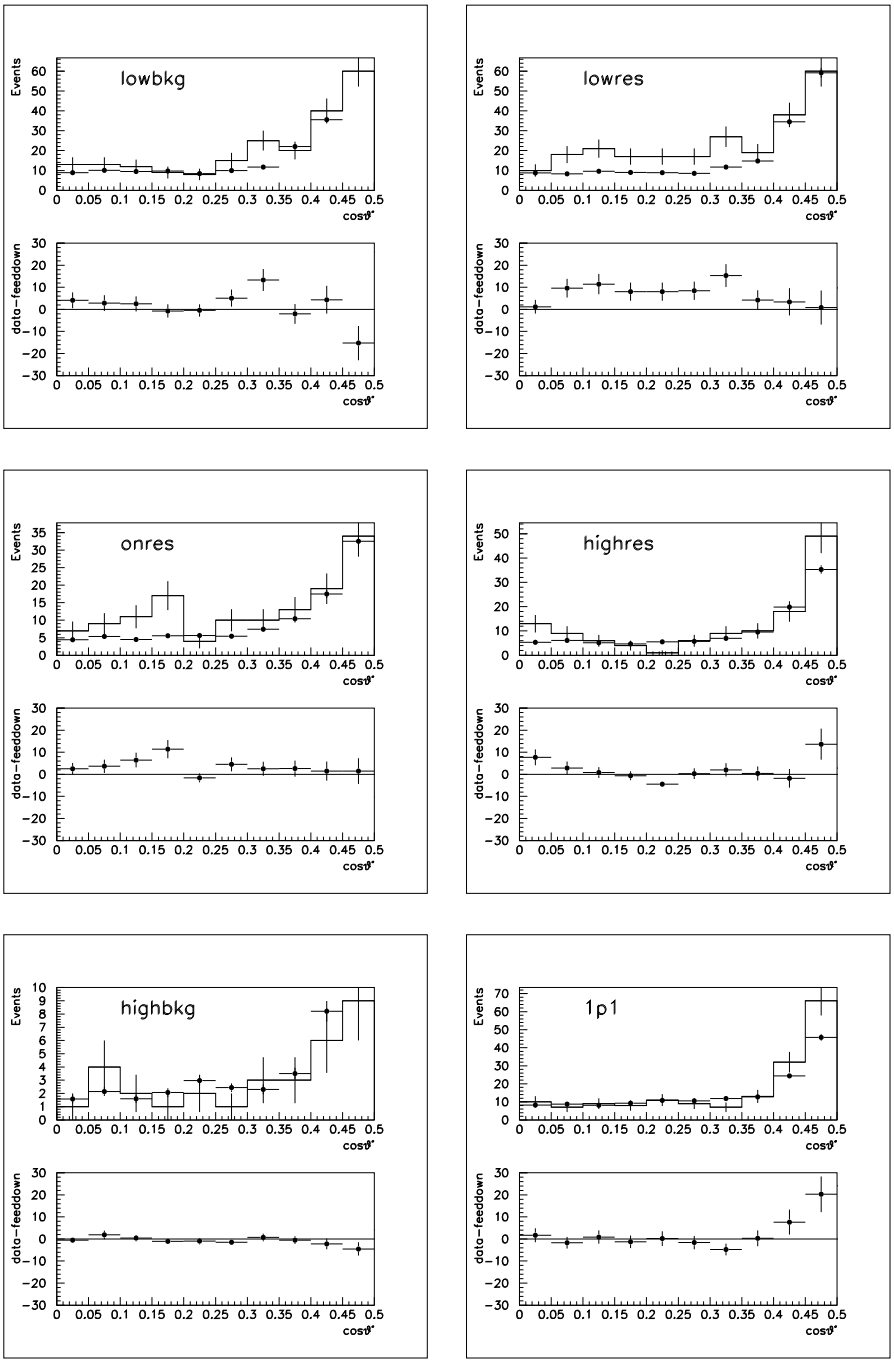

Figure 5.6: Top of each plot: Data and feeddown (dots) events versus $\cos\theta^*$ for different regions of $\sqrt{s}$. Bottom of each plot: Data−Feeddown.

3. On Resonance: 3415 MeV–$\mathcal{L}$=5.1 pb^{-1}

4. High Resonance: 3418-3425 MeV–$\mathcal{L}$=5.5 pb^{-1}

5. High Background: 3470 MeV–$\mathcal{L}$=2.5 pb^{-1}

6. χ_1-$^1P_1$ Region: 3511-3525 MeV–$\mathcal{L}$=12.4 pb^{-1}

There should be no signal in the χ_1-$^1P_1$ region and it is shown simply as a test of how well the feeddown calculation estimates the background. It was not used in any of the fits discussed here. Each plot in figure 5.6 shows the data and feeddown events in each region as well as the difference between the two. There is good agreement between the data and the feeddown in the background regions.

Figures 5.7 and 5.8 show the data and feeddown cross sections as a function of energy for slices and integrals of $\cos\theta^*$ respectively. There is a clear $\gamma\gamma$ signal seen for $\cos\theta^*$ less than 0.4. Above 0.4 the feeddown background begins to obscure the resonance.

5.3 $\gamma\gamma$ Continuum

Up to now, only the incoherent $\gamma\gamma$ background from $\pi^0\pi^0$ and $\pi^0\gamma$ events has been described. There is, however, the possibility of coherent direct production of two photons ($\overline{p}p \rightarrow \gamma\gamma$) present in the data sample and this needs to be examined. A number of experiments have studied the inverse channel, $\gamma\gamma \rightarrow \overline{p}p$, most notably the VENUS[40] and CLEO[41] collaborations. By using detailed balance, these two cross sections can be related.

The cross section for a two body process can be written generally as:

$$\sigma(ab \rightarrow cd) \propto (2s_c + 1)(2s_d + 1)p_{c,d}^2 \times |\mathcal{M}_{\mathrm{ab}\rightarrow\mathrm{cd}}|^2 \tag{5.1}$$

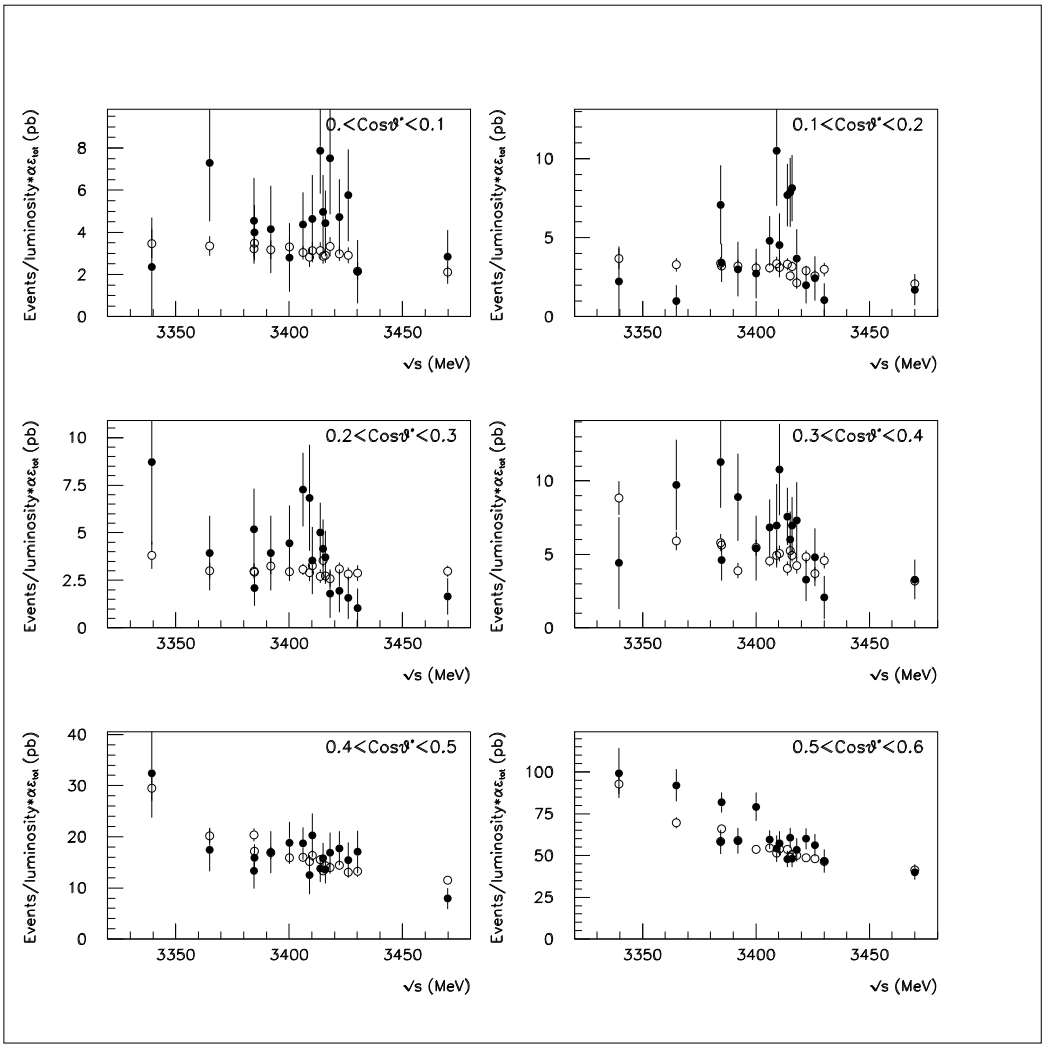

Figure 5.7: $\gamma\gamma$ cross section versus $\sqrt{s}$ for different slices of $\cos\theta^*$.

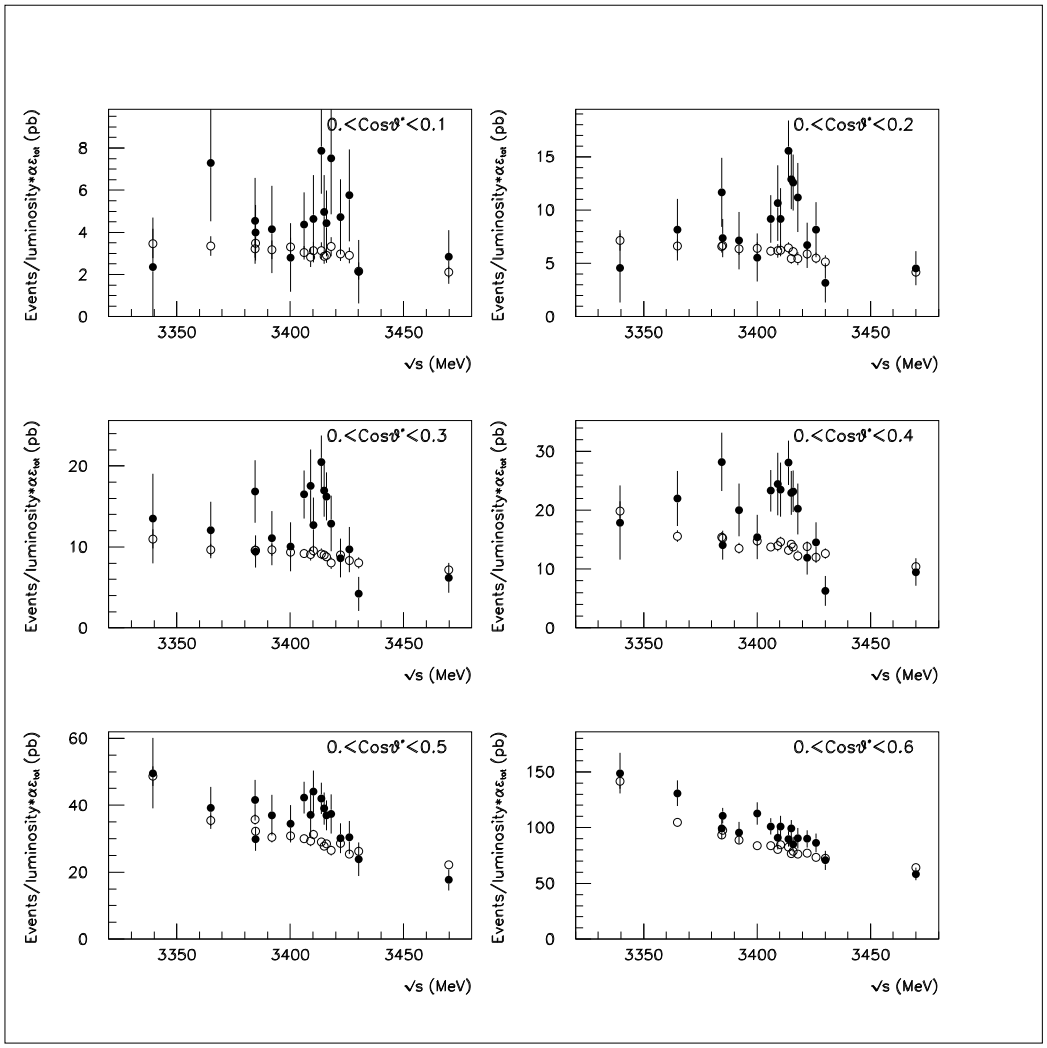

Figure 5.8: $\gamma\gamma$ cross section versus $\sqrt{s}$ for different integrals of $\cos\theta^*$.

where s_c and s_d are the spins of the final particles, $p_{c,d}$ is the particle's momentum, and $\mathcal{M}$ is the matrix element for the process. The matrix elements for a processes and its inverse are the same. Hence, the relationship between the two cross sections ($\overline{p}p \rightarrow \gamma\gamma$ and $\gamma\gamma \rightarrow \overline{p}p$) is given by:

$$\sigma(\overline{p}p \rightarrow \gamma\gamma) = \frac{(2s_\gamma + 1)(2s_\gamma + 1)}{(2s_{\overline{p}} + 1)(2s_p + 1)} \times \frac{p_\gamma^2}{p_p^2} \times \sigma(\gamma\gamma \rightarrow \overline{p}p). \tag{5.2}$$

Although photons are spin-one particles, there are only two possible spin orientations since longitudinally polarized photons are not physical. Thus the spin factor, $(2s_\gamma + 1)$, is 2 instead of 3 for the photons. The ratio $\frac{p_\gamma^2}{p_p^2}$ is 1.42 at the χ_0. The $\overline{p}p \rightarrow \gamma\gamma$ cross section then becomes:

$$\sigma(\overline{p}p \rightarrow \gamma\gamma) \sim 1.42 \times \sigma(\gamma\gamma \rightarrow \overline{p}p). \tag{5.3}$$

The published values of the $\gamma\gamma \rightarrow \overline{p}p$ cross sections are shown in the top plot of figure 5.9. Unfortunately, there is little data near the χ_0. The highest energy point available at 3.3 GeV has very few events so extrapolation is required. To do this, we have fit the VENUS data for $\cos\theta^* < 0.6$ to a power law and extrapolated it to the center of mass energy of the χ_0. This function, corrected for the inverse channel via equation 5.3, along with the feeddown subtracted $\gamma\gamma$ signal from the current analysis for $\cos\theta^* < 0.6$ is shown in figure 5.10 . The data is in good agreement with the extrapolation.

Since this amounts to strong evidence for a direct two-photon continuum in our data sample, the consequences of this need to be examined. In the VENUS/CLEO data (figures 5.10, 5.9), the angular distribution of the continuum is forward peaked and figure 5.9 suggests the forward peaking gets more pronounced with increasing energy. Unfortunately the lack of data at high energy prevents us from making a direct estimate of the $\overline{p}p \rightarrow \gamma\gamma$ for lower values of $\cos\theta^*$ at the χ_0.

Stack	Energy (MeV)	Lum (pb^{-1})	Data Evt	FD Evt	FD Error	ϵ_{anal}
47.2	3339.5	0.66	8	9.56	0.74	0.678
47.1	3365.0	1.42	22	16.88	0.98	0.703
42.1	3392.0	1.43	20	14.66	0.90	0.698
10.1	3384.4	1.63	32	18.93	1.04	0.695
31.1	3384.8	3.37	33	38.72	1.45	0.695
34.2	3400.1	1.48	17	17.70	0.97	0.742
14.2	3406.1	2.68	44	28.22	1.23	0.704
32.2	3409.1	1.13	21	13.09	0.84	0.757
12.1	3410.3	1.60	26	17.56	0.96	0.693
33.1	3413.8	2.93	55	28.14	1.57	0.669
9.1	3415.0	2.35	38	25.64	1.18	0.703
13.1	3415.9	2.73	43	27.74	1.29	0.679
7.1	3418.0	1.47	22	14.52	0.98	0.742
32.1	3422.1	2.15	18	22.77	1.10	0.702
11.1	3426.0	1.80	18	16.26	0.95	0.689
34.1	3430.1	1.44	6	13.15	0.86	0.664
8.1	3469.9	2.51	17	20.37	1.05	0.712
43.1	3510.6 (χ_1)	1.87	13	12.12	0.83	0.707
21.1	3525.2 ($^1P_1$)	3.71	17	25.31	1.18	0.680
23.1	3523.3 ($^1P_1$)	3.06	27	22.91	1.11	0.729
17.1	3526.6 ($^1P_1$)	3.71	22	23.80	1.16	0.676

Table 5.1: Energy sorted point-by-point results of $\chi_0 \to \gamma\gamma$ data and feeddown analyses up to $\cos\theta^* = 0.4$.

However, the possibility of substantial $\overline{p}p \to \gamma\gamma$ continuum interference with the $\chi_0 \to \gamma\gamma$ resonance cannot be ruled out.

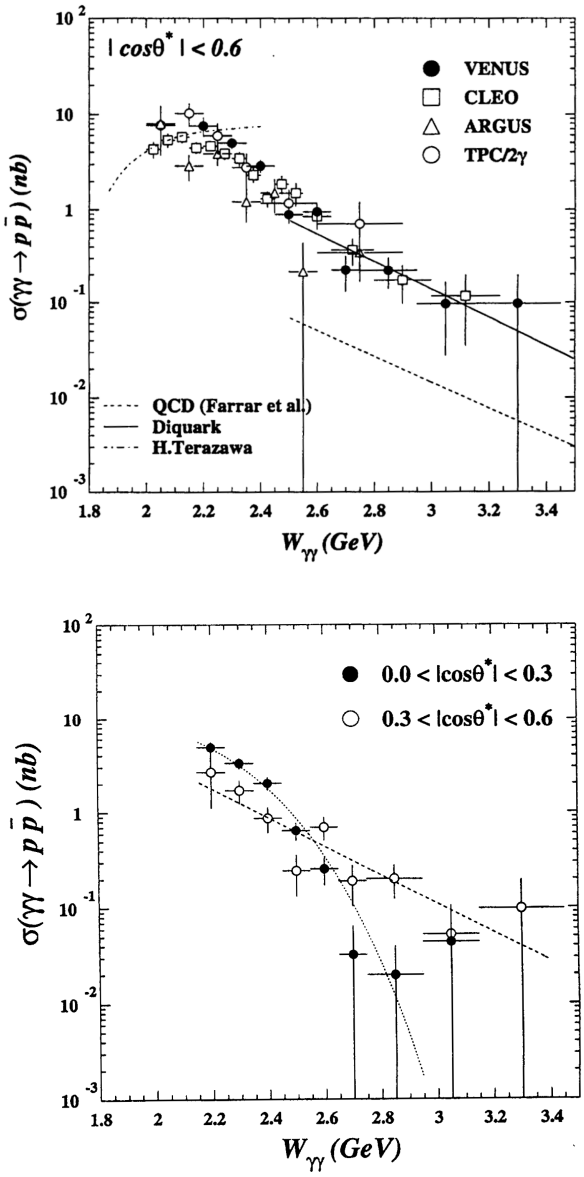

Figure 5.9: Top: The $\gamma\gamma \rightarrow \overline{p}p$ cross section for $\cos\theta^*$ <0.6. Bottom: The $\gamma\gamma \rightarrow \overline{p}p$ cross sections for two different ranges of $\cos\theta^*$.

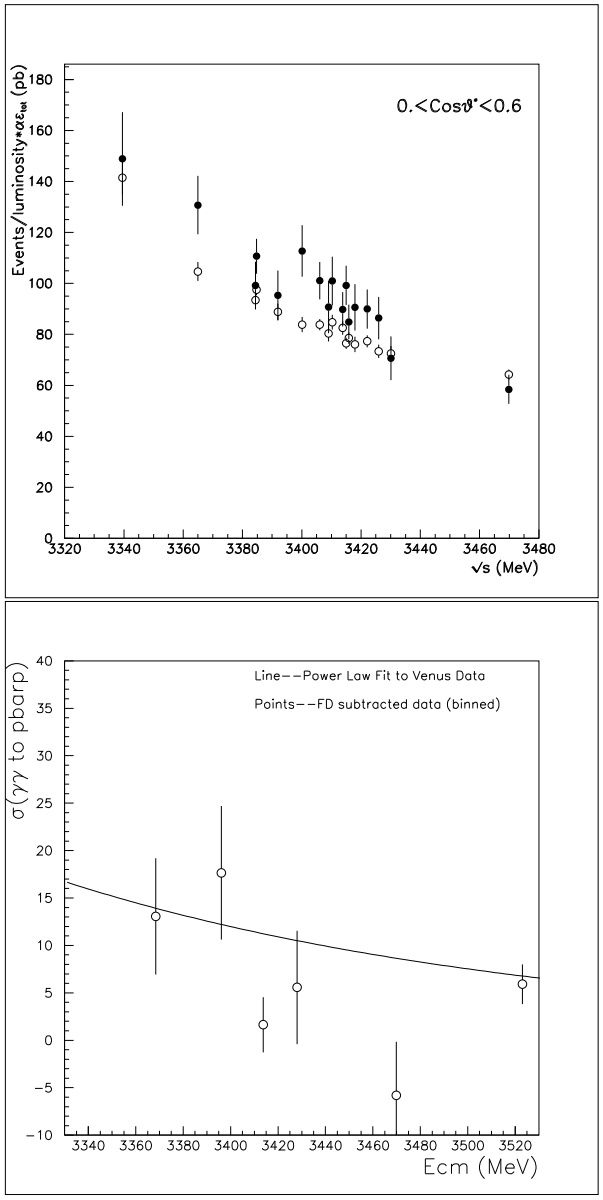

Figure 5.10: Top: the data (solid circles) and calculated feeddown (open circles) cross sections for $\cos\theta^*$ <0.6. Bottom: data-feeddown (points) with the fitted continuum cross section from VENUS.

Chapter 6

Results

In this chapter the methods used to fit the data to a Breit-Wigner resonance is described. The feeddown cross section is used to estimate the background and the possibility of an interfering $\overline{p}p \rightarrow \gamma\gamma$ continuum process is discussed. The Breit-Wigner fit gives the product of branching ratios $\mathrm{BR}(\overline{p}p \rightarrow \chi_0) \times \mathrm{BR}(\chi_0 \rightarrow \gamma\gamma)$. Using this result, various methods for extracting the partial width are described.

6.1 Likelihood Fit

The data and feeddown are fit using the maximum likelihood method. The likelihood function, shown below, uses a Poisson distribution for the probability density function of the data and a Gaussian distribution for the feeddown[1].

$$L = \prod_{j=1}^{N_{data}} \frac{\nu_j^{n_j} e^{-\nu_j}}{n_j!} \prod_{k=1}^{N_{feed}} \frac{1}{\sqrt{2\pi}\sigma_k} e^{\left(n_{feed,k} - \epsilon_{tot,k}\mathcal{L}_{\mathrm{k}}\sigma_{\mathrm{feed,k}}\right)^2/2\sigma_k^2} \tag{6.1}$$

[1]Since the feeddown calculation is based on hundreds of $\pi^0\pi^0$ and $\pi^0\gamma$ events for each stack, a Gaussian distribution is a very good approximation to the real, Poisson-like, distribution.

In the equation, n_j is the observed number of $\gamma\gamma$ candidates and ν_j is the fitted number of events given by:

$$\nu_j = \epsilon_{tot,k}\mathcal{L}_{\mathrm{k}} \left[\sigma_{\mathrm{feed,j}} + \int_{\alpha_{\mathrm{min}}}^{\alpha_{\mathrm{max}}} \left| \mathrm{Ae}^{\mathrm{i}\delta} - \frac{\mathrm{B}}{\mathrm{x}+\mathrm{i}} \right|^2 \mathrm{d}\cos\theta^* \right] \tag{6.2}$$

where:

$$\mathrm{x} \equiv \frac{2(\mathrm{M}_{\chi_0} - \sqrt{\mathrm{s}})}{\Gamma_{\chi_0}} \tag{6.3}$$

There are a few remarks that should be made about equation 6.2. First, the background due to the feeddown is taken to be the calculated feeddown cross section. In past analyses, the feeddown cross section has been fit simultaneously with the resonance [42]. Since, as will be shown later, there is a resonant contribution to the $\pi^0\pi^0$ cross section at the χ_0, the calculated feeddown is more appropriate. There may also be real stack-to-stack fluctuations in the π^0 detection efficiency that would be smoothed over in a fit. By excluding the feeddown cross section from the fit, the likelihood function simplifies to:

$$L = \prod_{j=1}^{N_{data}} \frac{\nu_j^{n_j} e^{-\nu_j}}{n_j!} \prod_{k=1}^{N_{feed}} \frac{1}{\sqrt{2\pi}\sigma_k}.$$

Also in equation 6.2, a complex term allows for interference between the resonance and continuum $\overline{p}p \rightarrow \gamma\gamma$. The parameter A represents the square root of the continuum cross section while B is the square root of the peak resonant cross section. The $\gamma\gamma$ branching ratio is related to B by:

$$B^2 = \frac{\pi(2J+1)}{k^2} B(\chi_0 \rightarrow \overline{p}p) B(\chi_0 \rightarrow \gamma\gamma) \tag{6.4}$$

with:

$$k^2 = \frac{M_{\chi_0}^2 - 4m_p^2}{4\hbar^2}$$

and δ is the phase between the resonant and continuum amplitudes.

Using data collected at the same energy points in the $\chi_0 \rightarrow J/\psi\ \gamma$ channel, E835 was able to improve the measurement of the mass and width of the χ_0. The mass and width were determined to be 3415.4±0.4±0.2 MeV and 9.8±1.0±0.1 MeV respectively [43]. These measurements are the most precise to date and for the fit to the two photon data, the mass and width have been fixed to these values.

The typical χ^2 statistic used for testing goodness-of-fit is obtained by assuming the data follows a Gaussian distribution. However, in the case of counting experiments with a low number of events, like in the $\gamma\gamma$ analysis, the data will follow a Poisson distribution. According to Baker and Cousins [44], a χ^2 statistic can be constructed for Poisson distributed data by using the likelihood ratio test theorem. The definition of the χ^2 in this case is:

$$\chi^2 = 2\Sigma \left[N_i^{th} - N_i^{obs} + N_i^{obs} ln(N_i^{obs}/N_i^{th}) \right] . \tag{6.5}$$

All of the values for χ^2 in what follows are calculated in this manner.

6.2 Interference and the $\cos\theta^*$ Cut

The optimum angular range which maximizes the signal-to-noise ratio needs to be determined. This should be used to extract the $\gamma\gamma$ partial width. From the feeddown cross section, it appears that a cut of $\cos\theta^*$ less than 0.4 would be appropriate since it is there that the forward peaking becomes prominent and errors in the subtraction begin to dominate. However, in the presence of a $\gamma\gamma$ continuum, the choice of the $\cos\theta^*$ cut may change, especially if there is interference with the resonant production.

With this in mind, the need for an interference term in the cross section for $\cos\theta^*$ less than 0.4 is demonstrated in figure 6.1. The value of χ^2 for the fit

	No Interference (A=0)		With Interference			
$\cos\theta^*$	$B_{\gamma\gamma}\times B_{\overline{p}p}$ x10^8	χ^2	$B_{\gamma\gamma}\times B_{\overline{p}p}$ x10^8	A^2 (pb)	δ_0	χ^2
0.2	6.52±1.18	8.3	5.58±4.54	0.15±0.27	3.3±1.0	6.9
0.3	5.09±0.90	17.9	5.27±3.00	0.92±0.58	0.3±0.9	10.0
0.4	5.05±0.81	31.8	5.36±2.90	1.73±0.80	3.5±0.8	17.9
0.5	4.39±0.83	13.3	4.51±4.67	1.10±1.00	3.4±1.0	8.7
0.6	-	-	-	11.2±2.0	-	20.0/15

Table 6.1: Results from the likelihood fits with and without interference.

with A=0 (dashed) is 31/15 NDF while it is 18/13 NDF allowing for interference (solid).

Even more telling is the comparison of the spectrum for $\cos\theta^* < 0.2$ with that for $0.2 < \cos\theta^* < 0.4$ (figure 6.2). For the central region, allowing the interference terms to be free has little effect on the result. For the region $0.2 < \cos\theta^* < 0.4$ however, it is impossible to understand the spectrum without assuming interference. The χ^2 is reduced from 32/15 NDF to 18/13 NDF by including the interference terms in the fit.

Table 6.1 shows the results of the fits with and without interference for different $\cos\theta^*$ cuts. The product of branching ratios does not change much, but the uncertainty increases by a factor of 3 by adding the two free parameters. The fitted continuum cross section appears to be forward peaked as would be expected based on the earlier observations by VENUS/CLEO.

In order to extract the resonance production rate with the least uncertainty we have chosen the cut at $\cos\theta^* < 0.2$, where the continuum is consistent with zero, and to exclude interference from the fit. The possible effect of interference will be taken into account as a systematic error.

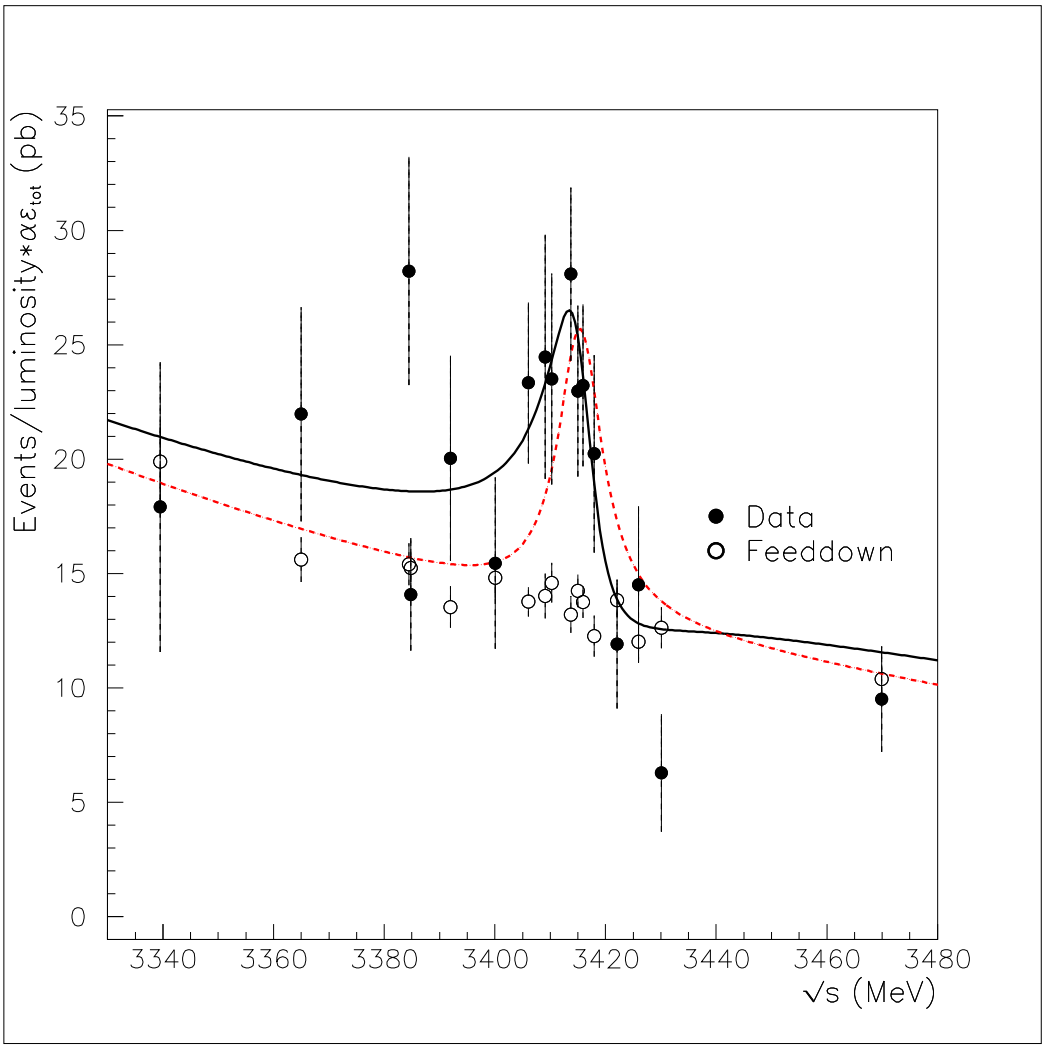

Figure 6.1: The $\gamma\gamma$ spectrum fit as described in the text for $\cos\theta^*$ <0.4 with the interference terms free (solid) and without interference (dashed).

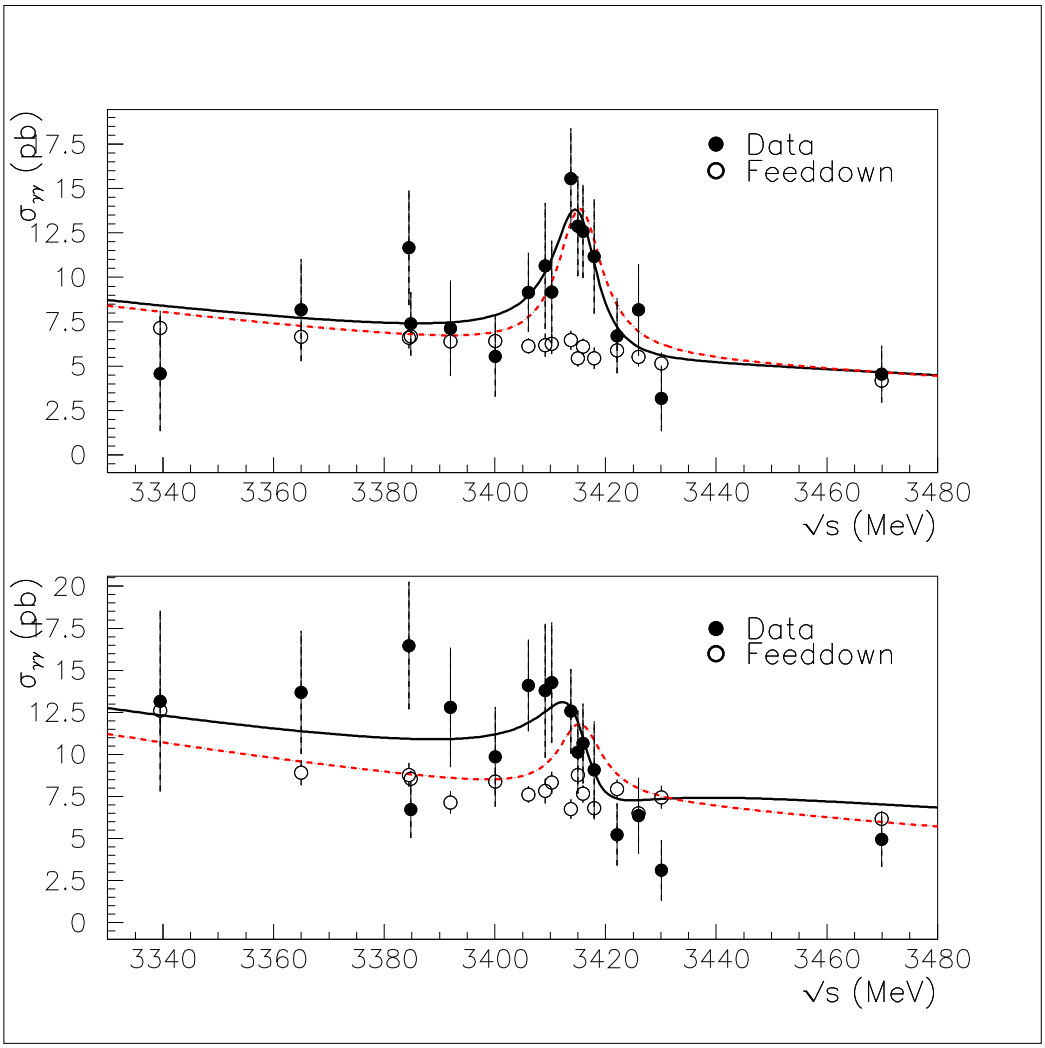

Figure 6.2: Two ranges of the $\gamma\gamma$ spectrum fit with (solid) and without (dashed) interference.

χ_0 Mass	0.6%
χ_0 Width	3.2%
Feeddown Correction	6.0%
Interference	5.0%
Luminosity	2.5%
Total	8.8%

Table 6.2: A summary of the sources of systematic error in the $\chi_0 \to \gamma\gamma$ branching ratio.

6.3 $\chi_0 \to \gamma\gamma$ Partial Width

Fitting the data below $\cos\theta^*$ =0.2 without continuum gives the product of $\mathrm{BR}_{in}\mathrm{BR}_{out}$ to be:

$$BR(\chi_0 \to \overline{p}p) \times BR(\chi_0 \to \gamma\gamma) = (6.52 \pm 1.18(sta) \pm 0.55(sys)) \times 10^{-8}.$$

The sources of the systematic error are summarized in table 6.2. The systematic errors from the uncertainties in the χ_0 mass and width were obtained by fixing their values to $\pm 1\sigma$ and refitting, taking as the error the largest change in the branching ratio. The error due to the feeddown was found in a similar way.

The $\gamma\gamma$ partial width is an interesting property theoretically. There are different ways to derive the partial width from our measured product of the branching ratios. The most straightforward way is divide the product by $\mathrm{BR}(\chi_0 \to \overline{p}p)$= $(2.2 \pm 0.5) \times 10^{-4}$ obtained from the PDG and then multiplying by the total width $\Gamma_{\chi_0} = 9.8 \pm 1.0$ MeV as measured by E835. This gives:

$$\Gamma_{\gamma\gamma,1} = 2.90 \pm 0.59(sta + sys) \pm 0.66(BR) \pm 0.3(width)\ keV. \qquad (6.6)$$

An alternative method is to use our measured product $\mathrm{BR}(\chi_0 \to \overline{p}p) \times \mathrm{BR}(\chi_0 \to J/\psi\ \gamma)$ (see table 6.4) to cancel the $\overline{p}p$ contribution and then use the PDG value for

BR($\chi_0 \rightarrow J/\psi\ \gamma$) to obtain the $\gamma\gamma$ partial width.

$$\begin{aligned}\Gamma_{\gamma\gamma,2} &= \Gamma_{\chi_0} \times \frac{BR(\overline{p}p \rightarrow \chi_0 \rightarrow \gamma\gamma)}{BR(\overline{p}p \rightarrow \chi_0 \rightarrow J/\psi\gamma)} \times BR(\chi_0 \rightarrow J/\psi\gamma) \\ &= 2.40 \pm 0.41(sta + sys) \pm 0.53(BR) \pm 0.24(width)\ keV. \qquad (6.7)\end{aligned}$$

A recent article by Patrignani[46] has made the point that it is very rare that one makes a direct experimental measurement of a single branching ratio. In the case of e^+e^- experiments, measurements of the χ states typically involve the branching ratio for $\psi' \rightarrow \chi\gamma$. In the case of E835, the product of BR($\chi_0 \rightarrow \overline{p}p$)BR($\chi_0 \rightarrow$X) is measured. The usual method of extracting the rate of interest is to divide out the so-called "known" branching ratio(s), as we have done in the previous paragraphs. This has led to measurements entering the PDG which are highly correlated with each other and, in some cases, has led to a propagation of systematic errors. Patrignani has introduced a global fit to all of the available data for ψ' and χ decays using each experimentally measured quantity (i.e. products of branching ratios) to extract individual branching ratios. This method overcomes the problem of propagating systematic effects from one measurement to another. The fit does not take into account possible correlations of systematic errors. The results of the global fit are used in the PDG's 2002 Review of Particle Physics [45].

E835 has recently made four new measurements at the χ_0: BR($\chi_0 \rightarrow \overline{p}p$)$\times$BR($\chi_0 \rightarrow J/\psi\ \gamma$), BR($\chi_0 \rightarrow \overline{p}p$)$\times$BR($\chi_0 \rightarrow \gamma\gamma$), BR($\chi_0 \rightarrow \overline{p}p$)$\times$BR($\chi_0 \rightarrow \pi^0\pi^0$), and the total width of the χ_0 (table 6.4). Instead of doing the complete fit over all of the χ and ψ' measurements, a fit has been performed using just the available χ_0 data. This fit includes all of the χ_0 measurements used in the 2002 PDG fit along with those listed in table 6.4. These measurements are decoupled from ψ' decays by fixing $\psi' \rightarrow J/\psi\ \pi^+\pi^-$ and $\psi' \rightarrow \chi_0\gamma$ to their 2002 PDG values. Table 6.3 shows the

	No E835(2000)	With E835(2000)	Improvement
Γ_{χ_0}	15.0±2.1	10.6±0.9	1.65
BR($\chi_0 \to J/\psi\ \gamma$)	1.02±0.17%	1.16±0.13%	1.43
BR($\chi_0 \to \overline{p}p$)	$(2.43\pm0.50)\times10^{-4}$	$(2.27\pm0.25)\times10^{-4}$	1.86
BR($\chi_0 \to \gamma\gamma$)	$(1.89\pm0.45)\times10^{-4}$	$(2.65\pm0.43)\times10^{-4}$	1.48
BR($\chi_0 \to 2(\pi^+\pi^-)$)	$(2.58\pm0.41)\times10^{-2}$	$(2.57\pm0.35)\times10^{-2}$	1.16
BR($\chi_0 \to \pi^0\pi^0$)	$(2.49\pm0.31)\times10^{-3}$	$(2.51\pm0.28)\times10^{-3}$	1.14
BR($\psi' \to J/\psi\ \gamma$)	8.67±0.73%	8.73±0.70%	1.05
χ^2/NDF	27.4/13	33.2/17	

Table 6.3: Results of the fit to χ_0 measurements with and without the 2000 E835 results.

Γ_{χ_0}[43]	9.8±1.0±0.1 MeV
BR($\chi_0 \to \overline{p}p$)×BR($\chi_0 \to J/\psi\ \gamma$)[43]	$(1.58\pm0.15\pm0.08)\times10^{-6}$
BR($\chi_0 \to \overline{p}p$)×BR($\chi_0 \to \gamma\gamma$)	$(6.52\pm1.18\pm0.55)\times10^{-8}$
BR($\chi_0 \to \overline{p}p$)×BR($\chi_0 \to \pi^0\pi^0$)[47]	$(5.1\pm0.8)\times10^{-7}$

Table 6.4: Summary of the χ_0 results from the 2000 run of E835.

results of the fit with and without the four E835 measurements. Also shown is the improvement in the fractional error defined as:

$$Improv = \left(\frac{\sigma_{NoE835}}{M_{NoE835}}\right) / \left(\frac{\sigma_{w/E835}}{M_{w/E835}}\right).$$

This measurement is in good agreement with previous measurements, as shown in Figure 6.3. In the figure the partial width derived by dividing the our measurement by the $\overline{p}p$ branching ratio as well as the partial width calculated by the semi-global fit are displayed. The results from earlier experiments in figure 6.3 and table 6.5 have been recalculated using branching ratio values published in the 2002 PDG.

CBALL(85)([48])	$\psi' \to\chi_0\gamma,\chi_0\to\gamma\gamma$	4.0±2.8
CLEO(90)([49])	$\gamma\gamma \to\chi_0\to$hadrons	<6.2(95%)
CLEO(95)([50])	$\gamma\gamma \to\chi_0\to$hadrons	1.7±0.8
E835(99)([51])	$\overline{p}p\to\chi_0\to\gamma\gamma$	1.6±1.1
CLEO(01)([52])	$\gamma\gamma \to\chi_0\to\pi^+\pi^-\pi^+\pi^-$	3.07±0.72

Table 6.5: Previous results for the partial width $\chi_0\to\gamma\gamma$ in keV.

This result can be compared with various predictions made for this process, which are shown as lines in figure 6.3. Our measurement agrees well with the prediction by Huang and Chao [19] (the errors in the prediction are not included in the plot) which was based on a NRQCD calculation with next-to-leading order QCD corrections. As described in chapter 1, NRQCD includes higher order color-octet Fock states in the calculation of hadronic decays. The decay rate of the χ_0 to two photons is a strong confirmation of the NRQCD approach.

6.4 Perturbative QCD and the Calculation of α_s

Within the framework of perturbative QCD, factors containing the charmonium wave function cancel in the ratio of the the $\gamma\gamma$ and gluon-gluon partial widths, leaving only terms containing the electromagnetic and strong coupling constants. This ratio given by [17]:

$$\frac{\Gamma_{\gamma\gamma}}{\Gamma_{gg}} = \frac{8\alpha^2}{9\alpha_s^2}\frac{\left[1+\frac{0.2}{\pi}\alpha_s\right]}{\left[1+\frac{9.5}{\pi}\alpha_s\right]}. \tag{6.8}$$

To a very good approximation, the partial width of χ_0 to two gluons is the same as the total width. Thus, this ratio is simply the $\gamma\gamma$ branching ratio.

This expression can be used in two different ways. By assuming a value of α_s of 0.28, also assumed by [17], and a total χ_0 width of 9.8 MeV, the PQCD

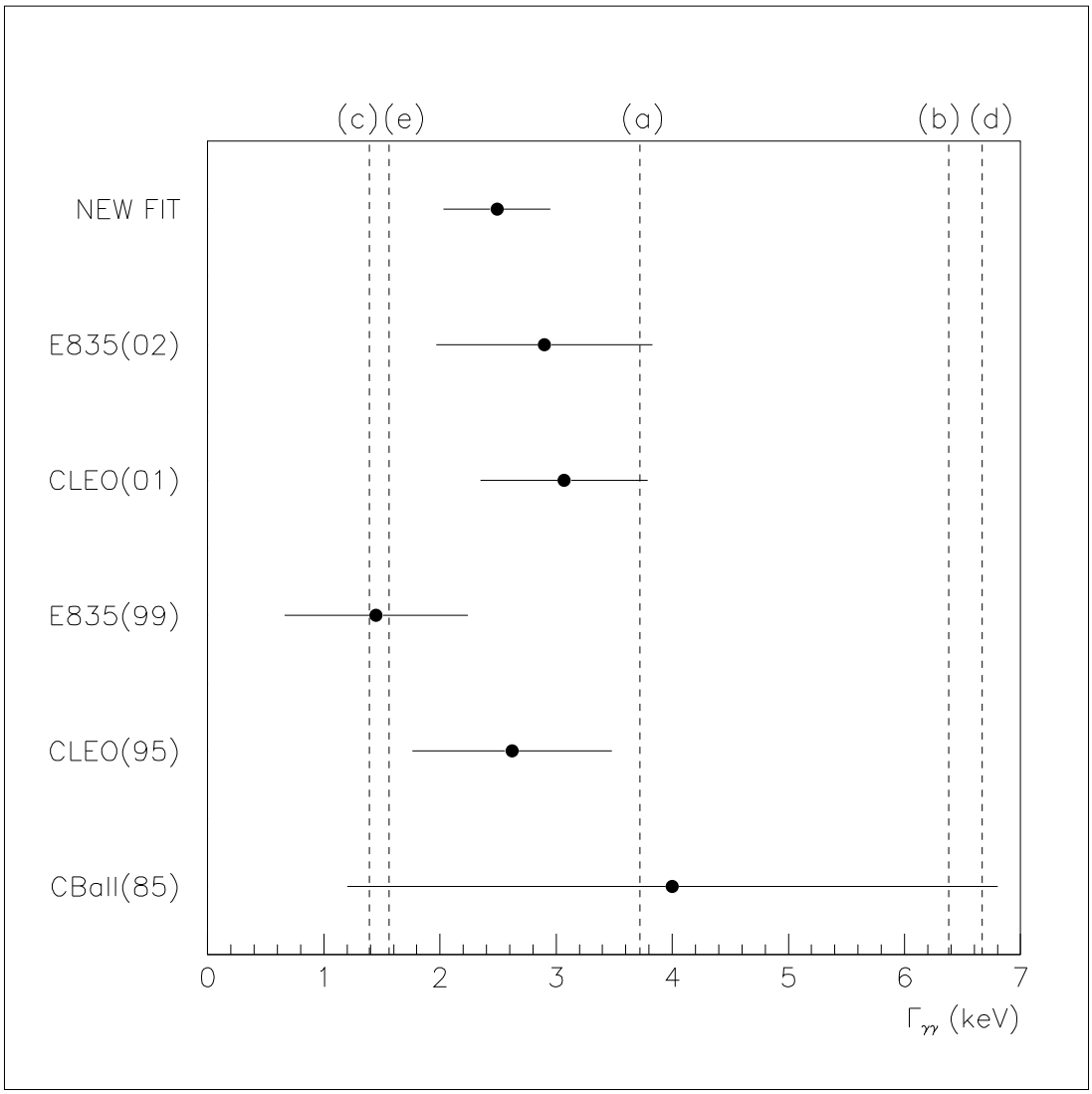

Figure 6.3: A summary of the measured $\Gamma_{\gamma\gamma}$ results along with the predicted values (dashed lines) compiled in table 1.1. The point labelled "New Fit" is the value derived from the semi-global fit described in the text.

prediction for the partial width is:

$$\Gamma_{\gamma\gamma,PQCD} = 3.26 \pm 0.33keV \tag{6.9}$$

which agrees with the current measurement.

Alternatively, this ratio can be used to calculate the strong coupling constant at the scale of the charm mass, about 1.5 GeV. Using our result for the branching ratio, we get a value of 0.29±0.04 for α_s. Figure 6.4 shows our result compared to previous measurements and the calculated value of the running coupling constant calculated at the Z_0 (91.1 GeV/c^2). Our result agrees with the running of the coupling constant from the Z_0 and with the measurement at 1777 MeV/c^2 derived from the lifetime of the τ lepton[53]. Although this result for α_s has a large uncertainty, it is nevertheless remarkable that a result based on perturbative QCD is in such good agreement with other measurements of this fundamental constant of QCD.

6.5 Conclusions

The value of the χ_0 two photon partial width derived from E835's measured product of branching ratios is in agreement with previous measurements. When E835's newest measurements are included in a fit with all of the previous χ_0 measurements, the uncertainty in the two branching ratio decreases by ~50%. There are also significant improvements in the χ_0 total width and branching ratios to $J/\psi\ \gamma$ and $\overline{p}p$. The two-photon width calculated from the global fit rules out all predictions except the one based on NRQCD, providing strong support for this approach. In addition, when calculated within the framework of PQCD, the value for the strong coupling constant, α_s, is in agreement with both the measurement

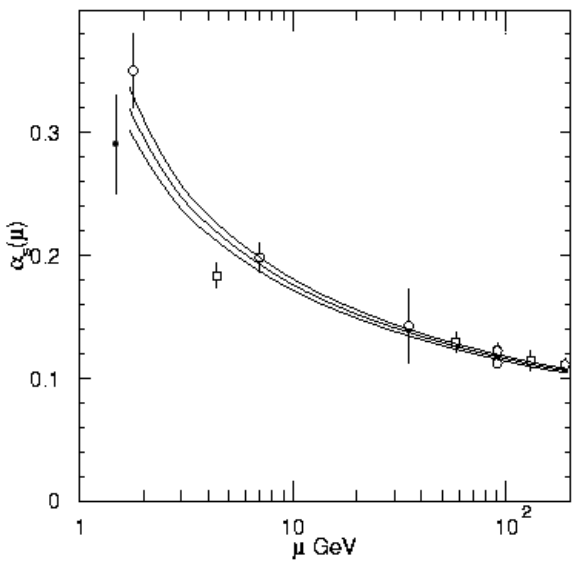

Figure 6.4: The strong coupling constant versus energy scale. The line is the value of α_s ($\pm 1\sigma$) running from the Z_0. The value obtained from our $\gamma\gamma$ result is the solid circle at $\sim$1.5 GeV.

done at the mass of the τ lepton and with the running of the coupling constant from the Z_0.

Appendix A

Random Gates

There is a rate dependent efficiency for the $\pi^0\pi^0$, $\pi^0\gamma$, and $\gamma\gamma$ analyses due to the cut on the number of clusters and on the requirement that the neutral veto be off. In order to simulate the pileup of hits in the detector, random snapshots of the detector were overlayed on top of each Monte Carlo event. The random gates were taken during each run at a rate of 10 Hz.

Approximately 1 million random gate events were recorded per stack. In order to get a true picture of the occupancy of the detector during the stack, the number of MC events generated was an integral number of total RG events for that stack. For example, if there were 900,000 random gate events for a stack, the number of MC events generated could be 1,800,000 but not 2 million. If the random gate file is not used in its entirety, the events at the beginning of the stack, which tend to be at a higher rate, will have a greater weight.

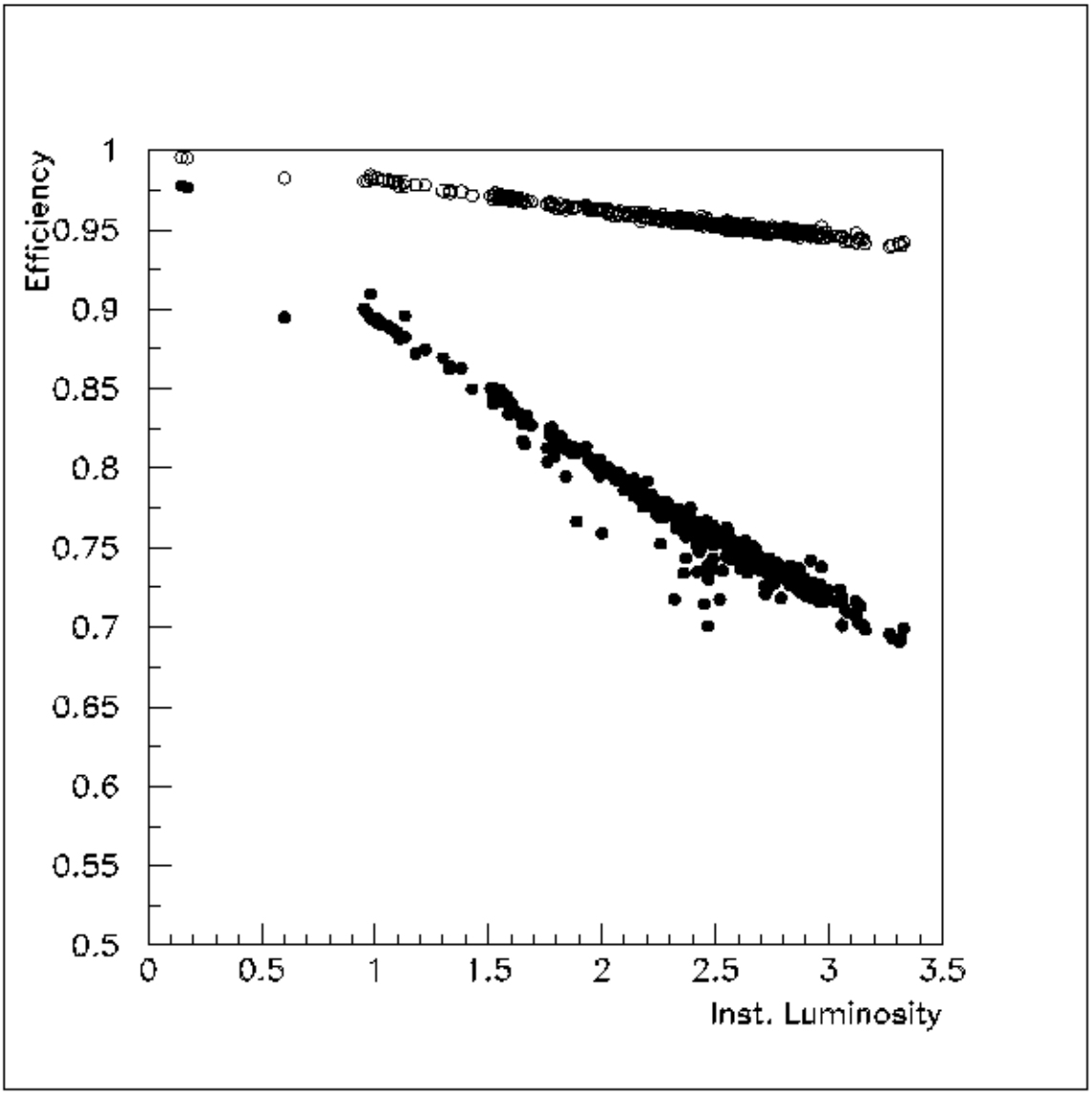

Figure A.1: The fraction of events without an in-time random cluster (open circles) and any random cluster (dark circles) as a function of instantaneous luminosity. This plot is made with 5/20 (seed/cluster) thresholds.

Appendix B

Trigger Efficiencies

As described in the text, there are two branches of the neutral trigger: ETOT and PBG. The efficiencies of these two branches are found by taking data with less restrictive requirements and counting how many of the events that pass the loose requirement would pass the more stringent one. The efficiencies are then calculated using $\pi^0\pi^0$ events which pass the ETOT-LOW trigger ($\geq$70% of available energy).

Inefficiency in the ETOT trigger comes about when a combination of energy loss in the cracks and shower fluctuations result in a 20% loss of the total energy of the interaction. Inefficiency in the PBG trigger occurs when one of the π^0s decays asymmetrically and the two photons do not land in the same super-block.

For the ETOT branch, a sample of events which pass the ETOT-LOW trigger are used. The efficiency is calculated using $\pi^0\pi^0$ events from the ETOT-LOW sample and finding how many of those events would pass the ETOT-HI requirement and have a hardware bit set for ETOT-HI. The efficiency of ETOT was around 0.99 for the χ_0 stacks.

The PGB efficiency was calculated in a similar way, using $\pi^0\pi^0$ events from the ETOT-LOW trigger. Offline, the logic of the PBG trigger is mimicked. First, the energy in the super-blocks is reconstructed from the signals in the CCAL blocks. If the energy in two opposing super-blocks are above the discriminator threshold settings, a PBG hit is recorded. The efficiency is the number of events with both a hardware and software PBG hit divided by the number with just the software hit. The PGB efficiency for χ_0 stacks was typically 0.995.

Since $\pi^0\pi^0$, $\pi^0\gamma$, and $\gamma\gamma$ events can come in both channels, the overall trigger efficiency will be a combination of the two individual ones. The efficiency is given as:

$$\epsilon_{neuttrig} = \epsilon_{ETOT} + (1 - \epsilon_{ETOT})\epsilon_{PBG}. \tag{B.1}$$

This equation assumes that the inefficiencies in the two branches are uncorrelated. For all stacks, the overall efficiency was extremely close to 1.0.

There is one more factor concerning the trigger. There are a number of study triggers with looser requirements which are pre-scaled either in hardware or software. The reactions of interest may be allowed to pass on some of these triggers. Events coming in on the study triggers are not used for analysis, thus amounting to an inefficiency. With regards to the neutral analyses, there are three study triggers involved: ETOT, PBG, and minimum bias. The ETOT and PBG study triggers simply passes every 1 out of 100 events which pass the appropriate hardware trigger without going through the software trigger. The minimum bias study trigger automatically passes every 1 out of 5000 events which passes the minimum bias requirements. The inefficiency from the study triggers, called the auto-pass efficiency, is then:

$$(1 - \epsilon_{auto}) = 1/p_{etot} + 1/p_{pbg} + 1/p_{min-bias} \tag{B.2}$$

where p_x is the pre-scale factor for each trigger. The resulting ϵ_{auto} is 0.98.

Appendix C

Neutral DSTs

In order to expedite data analysis, all neutral events were pre-analyzed and sorted into data summary tapes (NDSTs)[54]. Events were sorted into three broad data sets. The sets were: CCAL with 25/50 MeV (seed/cluster) thresholds, CCAL+FCAL with 25/50 MeV thresholds, and CCAL with 5/20 MeV thresholds. The cuts made on the events were:

- 2<Number of clusters<9
- $|P_z - P_{\overline{p}}| < 0.15 \times P_{\overline{p}}$
- $\sqrt{P_x^2 + P_y^2} < 350 MeV$.

Events passing these cuts were further sorted depending on how many clusters the events had. The data sets used in my analysis were the CCAL 25/50 3- and 4-cluster events. The $\gamma\gamma$ data analysis used the neutral gold data set that had looser requirements.

The efficiency for these cuts was determined by looking at $\pi^0\pi^0$ events[55]. Events were selected using cuts similar to those used in this thesis on events from

the a run of raw data and the corresponding 4-cluster NDST. This was done for each energy point. There was no noticeable angular or rate dependence in the efficiency but a small energy dependence there was observed (bottom figure C.1). For the calculation of the $\pi^0\pi^0$ and $\pi^0\gamma$ cross sections, the NDST efficiency as calculated for the appropriate energy point was used.

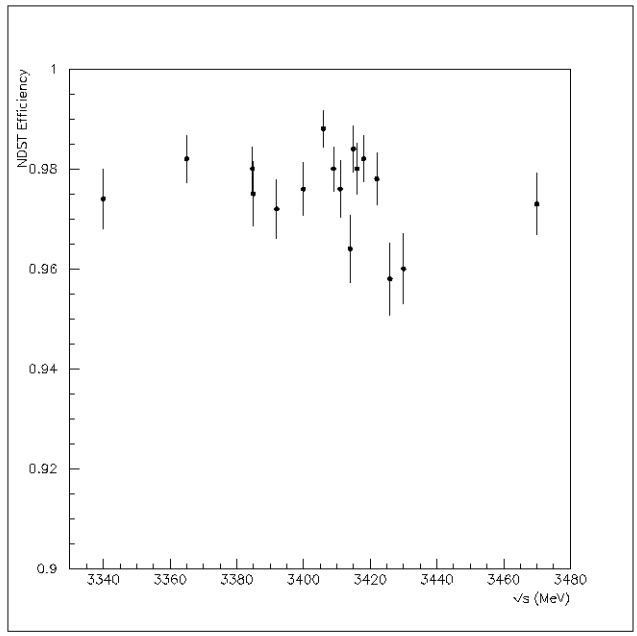

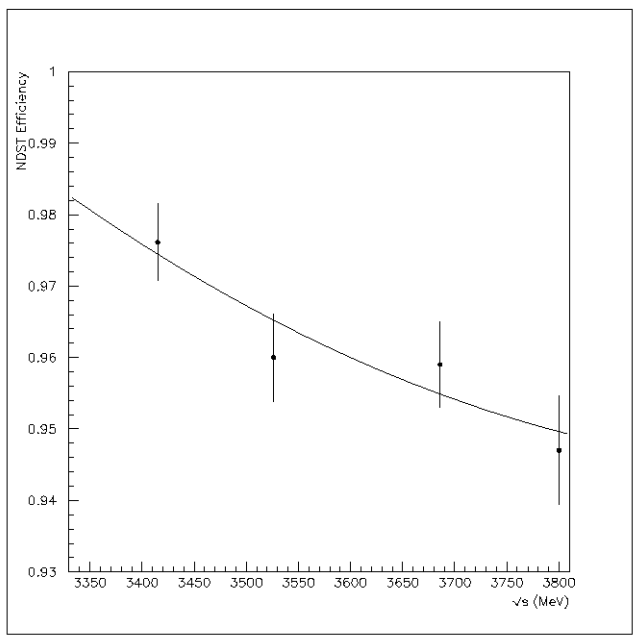

Figure C.1: The neutral DST efficiency near the χ_0 (top) and for the entire range of data taken in the 2000 E835 run (bottom).

References

[1] M. Gell-Mann, "A Schematic Model Of Baryons And Mesons," Phys. Lett. **8**, 214 (1964).

[2] S. L. Glashow,"Partial Symmetries Of Weak Interactions," Nucl. Phys. **22**, 579 (1961).

[3] S. Weinberg,"A Model Of Leptons," Phys. Rev. Lett. **19**, 1264 (1967).

[4] J. E. Augustin *et al.*, "Discovery Of A Narrow Resonance In E+ E- Annihilation," Phys. Rev. Lett. **33**, 1406 (1974).

[5] G. S. Abrams *et al.*, "The Discovery Of A Second Narrow Resonance In E+ E- Annihilation," Phys. Rev. Lett. **33**, 1453 (1974).

[6] J. J. Aubert *et al.*, "Experimental Observation Of A Heavy Particle J," Phys. Rev. Lett. **33**, 1404 (1974).

[7] G. S. Abrams *et al.*,"The Decay Of Psi (3700) Into Psi (3100)," Phys. Rev. Lett. **34** (1975) 1181.

[8] S. L. Glashow, J. Iliopoulos and L. Maiani, "Weak Interactions With Lepton - Hadron Symmetry," Phys. Rev. D **2**, 1285 (1970).

[9] W. E. Burcham and M. Jobes, *Nuclear and Particle Physics*, Prentice Hall, 1995, pgs 409-413.

[10] T. Appelquist and H. D. Politzer,"Orthocharmonium And E+ E- Annihilation," Phys. Rev. Lett. **34**, 43 (1975).

[11] S. Okubo, "Phi Meson And Unitary Symmetry Model," Phys. Lett. **5**, 165 (1963).

[12] D. Aschman [Crystal Ball Collaboration], "Radiative Decays Of The Psi And Psi-Prime," in *C80-03-09.23* SLAC-PUB-2550 *Invited talk presented at XVth Rencontre de Moriond, Les Arcs, France, Mar 9-21, 1980.*

[13] E. Eichten, K. Gottfried, T. Kinoshita, K. D. Lane and T. M. Yan, "Charmonium: Comparison With Experiment," Phys. Rev. D **21**, 203 (1980).

[14] H. J. Schnitzer, "The P - States Of Charmonium And The Forces That Confine Quarks," Phys. Rev. Lett. **35**, 1540 (1975).

[15] J. Pumplin, W. Repko and A. Sato, "Fine Structure Corrections And Electromagnetic Decays Of Charmonium," Phys. Rev. Lett. **35**, 1538 (1975).

[16] B. J. Bjorken and S. D. Drell, *Relativistic Quantum Mechanics*, McGraw-Hill Book Company, New York, 1965.

[17] W. Kwong, P. B. Mackenzie, R. Rosenfeld and J. L. Rosner, "Quarkonium Annihilation Rates," Phys. Rev. D **37**, 3210 (1988).

[18] G. T. Bodwin, E. Braaten and G. P. Lepage, "Rigorous QCD analysis of inclusive annihilation and production of heavy quarkonium," Phys. Rev. D **51**, 1125 (1995)

[19] H. W. Huang and K. T. Chao,"QCD Radiative Correction to the Hadronic Annihilation Rate of 1 +− Heavy Quarkonium," Phys. Rev. D **54**, 3065 (1996) [Erratum-ibid. D **56**, 7472 (1997 ERRAT,D60,079901.1999)] [arXiv:hep-ph/9601283].

[20] S. N. Gupta, J. M. Johnson and W. W. Repko, "Relativistic two-photon and two-gluon decay rates of heavy quarkonia," Phys. Rev. D **54**, 2075 (1996)

[21] C. R. Munz, "Two-Photon Decays of Mesons in a Relativistic Quark Model," Nucl. Phys. A **609**, 364 (1996)

[22] T. Barnes,"Two photon couplings of quarkonia with arbitrary J(PC)," ORNL-CCIP-92-05 *Invited paper to Int. Workshop on Photon-Photon Collisions, La Jolla, CA, Mar 22-26, 1992.*

[23] T. A. Armstrong *et al.* [E760 Collaboration], "Measurement of the J / psi and psi-prime resonance parameters in anti-p p annihilation," Phys. Rev. D **47**, 772 (1993).

[24] C. Baglin *et al.* [R704 Collaboration], "Formation Of The Chi(1) And Chi(2) Charmonium Resonances In Anti-Proton - Proton Annihilation And Measurements Of Their Masses And Total Widths," Phys. Lett. B **172**, 455 (1986).

[25] D. Allspach *et al.* [E835 Collaboration], "The variable density gas jet internal target for experiment 835 at Fermilab," Nucl. Instrum. Meth. A **410**, 195 (1998).

[26] M. Graham and S.S. Seo, "Modifications to the FCAL2000 Clusterizer," E835 Internal Memo.

[27] M. Graham,S.S. Seo, and R. Rusack, "FCAL2000 Calibration," E835 Internal Memo.

[28] S. Bagnasco *et al.*, "A Straw Chambers' Tracker For The High Rate Experiment 835 At The Fermilab Accumulator," Nucl. Instrum. Meth. A **409**, 75 (1998).

[29] D. Bettoni *et al.*, "Experimental Study Of a Cylindrical Scintillating Fiber Detector", IEEE Trans. Nucl. Sci., 44 (1997),460-463.

[30] M. Atac *et al.*, "Scintillating fiber tracking for the SSC using visible light photon counters," Nucl. Instrum. Meth. A **314**, 56 (1992).

[31] S. Bagnasco *et al.*, "The Threshold Gas Cherenkov Counter Of Charmonium Experiment 835 At Fermilab," Nucl. Instrum. Meth. A **424**, 304 (1999).

[32] S. Trokenheim, M. Sarmiento, K. K. Seth and L. Bartoszek, "A P Anti-P Luminosity Monitor For Fermilab Experiment E760," Nucl. Instrum. Meth. A **355**, 308 (1995).

[33] T. A. Armstrong *et al.* [E760 Collaboration],"Precision Measurements Of Anti-Proton Proton Forward Elastic Scattering Parameters In The 3.7-Gev/C To 6.2-Gev/C Region," Phys. Lett. B **385**, 479 (1996).

[34] M. Ambrogiani *et al.*, "Experiment E835 at Fermilab", to be published.

[35] G. Lasio and M. Stancari, "Calibration of the Central Calorimeter in E835," E835 Internal Memo.

[36] M. Graham, "Tuning the CCAL Shower Monte Carlo and the Impact on the Feeddown Systematic Error," E835 Internal Memo.

[37] M. Stancari, Ph.D. thesis, University of California-Irvine, 1999.

[38] T. A. Armstrong *et al.* [Fermilab E760 Collaboration],"Two body neutral final states produced in anti-proton - proton annihilations at 2.911-GeV <= s**(1/2) <= 3.686-GeV," Phys. Rev. D **56**, 2509 (1997).

[39] M. Orbertino, "Studio dei Decadimenti Dello Stato $^3P_0(\chi_{c0})$ del Charmonio: $\chi_0 \to J/\psi\ \gamma \to e^+e^-\ \gamma$ and $\chi_0 \to \gamma\gamma$ Nell'ambito Dell'esperimento E835 del Fermilab," PhD Dissertation.

[40] H. Hamasaki *et al.* [VENUS Collaboration], "Measurement of the proton antiproton pair production from two-photon collisions at TRISTAN," Phys. Lett. B **407**, 185 (1997).

[41] M. Artuso *et al.* [CLEO Collaboration], "Measurement of cross-section for gamma gamma → p anti-p," Phys. Rev. D **50**, 5484 (1994).

[42] T. A. Armstrong *et al.* [E760 Collaboration],"Study of the eta(c) (s wave singlet) state of charmonium formed in anti-p p annihilations and a search for the eta(c)-prime (s wave doublet)," Phys. Rev. D **52**, 4839 (1995).

[43] S. Bagnasco *et al.* [Fermilab E835 Collaboration], "New Measurements Of The Resonance Parameters Of The Chi/C0(1(3)P(0)) State Of Charmonium," Phys. Lett. B **533**, 237 (2002).

[44] S. Baker and R. D. Cousins, "Clarification Of The Use Of Chi Square And Likelihood Functions In Fits To Histograms," Nucl. Instrum. Meth. A **221**, 437 (1984).

[45] K. Hagiwara *et al.* [Particle Data Group Collaboration], "Review Of Particle Physics," Phys. Rev. D **66**, 010001 (2002).

[46] C. Patrignani,"On the particle data group evaluation of chi/c(1P) and psi'(2S) branching ratios," Phys. Rev. D **64**, 034017 (2001).

[47] S. Bagnasco *et al.*, to be published.

[48] R.A. Lee, Ph.D. thesis, Stanford University, 1985, Report No. SLAC-0282.

[49] W. Y. Chen *et al.*,"Measurement Of Gamma Gamma Widths Of Charmonium States," Phys. Lett. B **243**, 169 (1990).

[50] V. Savinov and R. Fulton, "Measurements of the two photon widths of the charmonium states eta(c), chi(c0) and chi(c2),"arXiv:hep-ex/9507006.

[51] M. Ambrogiani *et al.*, "Study Of The Gamma-Gamma Decays Of The Chi(C2) (1**3 P(2)) And Chi(C0) (1**3 P(0)) Charmonium Resonances," Phys. Rev. D **62**, 052002 (2000).

[52] B. I. Eisenstein *et al.* [CLEO Collaboration], "Experimental investigation of the two-photon widths of the chi/c0 and the chi/c2 mesons," Phys. Rev. Lett. **87**, 061801 (2001).

[53] T. Coan *et al.* [CLEO Collaboration],"Measurement of alpha-s from tau decays," Phys. Lett. B **356**, 580 (1995).

[54] Ted Vidnovic III and Paolo Rumerio, "E835′ Neutral DST Format and Production Streaming," E835 Internal Memo.

[55] Ted Vidnovic III, "NDST Efficiency in the $\pi^0\pi^0$ Analysis," E835 Internal Memo.